DEPOSITION OF SIZE-SELECTED NANOCLUSTERS

by

Lu Cao

A thesis submitted to The University of Birmingham for the degree of Doctor of Philosophy

Nanoscale Physics Research Laboratory

School of Physics and Astronomy

The University of Birmingham

September 2015

Abstract

The work presented in this thesis explores the production and the controlled deposition of size-selected nanoclusters. The size-dependent propagation of gold nanoclusters is investigated by depositing them through few-layer graphene (FLG) using a magnetron sputtering cluster source. Au_{55} nanoclusters penetrate through the FLG, however Au_{923} nanoclusters remain on the surface, as imaged by aberration corrected scanning transmission electron microscope (ac-STEM). The control of the atomic structure of gold nanoclusters (Au_{923}) by systematically varying the gas-phase condensation parameters in the magnetron sputtering cluster source (e.g. magnetron power and condensation length) is also reported. Results show we have the ability to eliminate all icosahedral isomers by tuning the formation conditions. The biggest advance reported in the work concerns the new technology of the Matrix Assembly Cluster Source (MACS), which has the potential to increase the production rate of nanoclusters by 7 orders of magnitude from 0.1-1nA (from a magnetron source) to 1-10mA. The principle of the MACS is demonstrated by the production of Ag and Au clusters. The development of the latest MACS instrument is also described. An equivalent cluster beam current of ~100nA has been achieved. Gold and silver clusters produced under controlled experimental conditions show a relatively narrow size distribution even without mass selection (at best ±25% in the number of atoms). The mean cluster size can be controlled via the experimental parameters, especially the metal concentration in the matrix. STEM is again the principal tool employed characterize the number and structure of cluster produced by the MACS.

Acknowledgements

I would like to thank many people for the help and support during my PhD life, especially the following individuals.

Prof. Richard Palmer, my supervisor, for the opportunity to work in the NPRL with such challenge but interesting project. Also thanks for providing me with inspiration, advice and motivation throughout last four years.

Dr. Feng Yin, co-supervisor, for the continuous support and suggestions on the all the works and other matters, without whom I cannot complete this thesis.
Dr. Simon Plant, co-supervisor, for the expertise and assistance on cluster source and excellent comments on the draft of the thesis.

William Terry, for the irreplaceable technical support on the MACS project. Dr. Zhiwei Wang, Miriam Dowle, and Dr. Kenton Arkill, for the patience and help on the electron microscope.

Dr. Ziyou Li, Dr. Quanming Guo, Dr. Wolfgang Theis, Dr. Richard Balog, Dr. Vitor Oiko, Dr. Karl Bauer, Nan Jian, Thibaut Mathieu, Jian Liu, Rongsheng Cai, Scott Holmes, for the help in many areas related to the project.

All past and present colleagues, in particular Kuo-Juei Hu, whose consistent friendship and support have been invaluable.

Author's Contribution

All of the work presented in this thesis was conducted by the author under the supervision of Prof. Richard Palmer and co-supervision of Dr. Feng Yin and Dr. Simon Plant. The contributions between the author and collaborators are described in full at the start of each chapter.

Author's Publications

Plant, S. R., Cao, L., Yin, F., Wang, Z. W., & Palmer, R. E. (2014). Size-dependent propagation of Au nanoclusters through few-layer graphene. Nanoscale, 6(3), 1258-1263.

Plant, S. R., Cao, L., & Palmer, R. E. (2014). Atomic structure control of size-selected gold nanoclusters during formation. Journal of the American Chemical Society, 136(21), 7559-7562.

Cao, L. et al., Matrix assembly cluster source (MACS) metal doping, In preparation.

Table of Contents

Chapter 1 Overview

Nanoclusters are attracting great attention because of their size and structural dependent properties as well as the interactions between nanoclusters and surfaces, which give nanoclusters vast potential in various applications such as catalysis [1-6], optical spectroscopy [7-9], nanoelectronics and biochips [10-12]. Deposition of nanoclusters on the surface offers a routine to control the properties even for novel materials such as graphene. The developments on the cluster beam and mass selection technologies provide the possibility to deposit nanoclusters on surfaces under high control [13-15].

1.1 Outstanding challenges

Although the selection of the size of nanoclusters produced in the cluster beam now permits the investigation of their size-dependent properties [16-22], however, there are still many outstanding challenges remaining in this field. One of the major challenges is even for a specific size, nanoclusters exhibit a range of geometric structures as reported on size-selected gold nanoclusters containing

magic number of atoms such as 20, 55, 309 and 923 [23-26]. The ability to control the isomer populations during formation of nanoclusters would enable their properties to be correlated with their atomic configurations. Indeed, one could argue that the combination of size-selection and atomic structural determination would represent an "ultimate limit" of control at the nanoscale. Another is the production rate of clusters by cluster beam deposition is limited by the cluster beam flux. For example, the typical cluster beam current generated in a magnetron sputtering gas condensation cluster source is limited to about 0.1-1nA, equivalent to only ~micrograms of clusters per hour [14]. This amount is sufficient for demonstration purpose of nanoclusters, for example as model catalysts. However, ~mg/day or even ~kg/day is the required economic quantities for applications such as test-tube tests and pharmaceutical/ fine chemicals application.

1.2 Overview of the thesis

In this thesis, we first explore the size dependent propagation of nanoclusters to demonstrate the potential in generation of nanostructured membranes. Secondly to overcome the "ultimate limit" challenge, condensation parameters in magnetron sputtering source are investigated in order to control the structures of nanoclusters. Finally, we report the progress on the proof-of-principle demonstration and development of the new technology, the matrix assembly cluster source, which has the potential to achieve abundant production of nanoclusters. This work acts as the bridge connecting fundamental demonstrations and practical applications of nanoclusters.

This thesis starts from the review of the related fields in Chapter 2 based on which are the works presented in this thesis. This chapter includes the introduction of the nanoclusters, production methods, characterization approaches, review of nanolcuster structures and the applications of the nanoclusters in variable areas. The introduction of nanoclsuters begins with the definition of the nanoclusters and briefly summarizes properties of nanoclusters, and their critical roles in variable applications. The review of nanocluster production methods focuses on the cluster beam deposition (CBD) techniques such as thermal source, laser ablation source and especially the magnetron source. Other production methods like wet-chemical way are also introduced. The characterization approaches reviewed in this chapter is focused on the scanning transmission electron microcopy (STEM), which is the primary characterization tool used for the works reported in this thesis. This part includes the history of the TEM/STEM and the image formation mechanisms in STEM. The review of nanocluster structure consists of the introduction of high symmetrical structures which are icosahedral, decahedral and fcc, and both theoretical calculations and experimental observations of cluster structures reported in last few years. The application of nanoclusters part briefly describes their utilizations especially in catalysis and biotechnologies.

The experimental apparatus used for the work in this thesis, such as the magnetron sputtering gas condensation cluster source equipped with lateral time-of-flight (ToF) mass filter and the aberration corrected scanning transmission electron microscope (ac-STEM), are described in Chapter 3. The schematics and basic components of both apparatuses are illustrated. The

operation of the magnetron source is introduced, with focus on how to optimize the cluster beam current and mass spectra measurement (sections 3.1.4 and 3.1.5). The STEM part focuses on the high angle annular dark field (HAADF) image and bright field (BF) image in section 3.2.2, both of which are used to characterize the clusters. The effects of electron beam are reported in section 3.2.3.

Chapter 4 to 6 are the result parts of the thesis. The works reported in Chapter 4 are the deposition and structural control of size-selected nanoclusters produced using the magnetron sputtering cluster source. The first part of the work reported in Chapter 4.1 is the size dependent propagation study of Au nanoclusters through few-layer graphene. Size-selected Au_{55} and Au_{923} nanoclusters, synthesized in the magnetron sputtering cluster source and size selected by the lateral time-of-flight mass filter, were deposited onto the few-layer graphene (FLG) surface [27]. The results show that clusters propagate through the FLG via a mechanism of defect generation, which is strongly dependent on cluster size. This approach provides an opportunity to control the introduction of dopant nanoclusters and generation of nanoscale defects in graphene or other thin membrane materials.

In the second part, in Chapter 4.2 we report the atomic structure control of size-selected Au_{923} nanoclusters by variation of the formation conditions such as magnetron power and condensation length [28]. Size-selected Au_{923} clusters prepared using a magnetron sputtering gas condensation cluster source exhibited three main high symmetry isomers: decahedral (Dh), icosahedral (Ih)

and face-centred cubic (fcc) structures such as the cuboctahedron.[26] The identification of the proportions of Ih, Dh and fcc isomers of Au_{923} nanoclusters within a given population, corresponding to a specific set of formation conditions was achieved by comparing HAADF STEM imaging at atomic resolution with multi-slice image simulations [24]. The results show we have the ability to tune the cluster formation conditions in order to eliminate all icosahedral isomers, which offers a route to the preparation of arrays or ensembles of supported nanoclusters consisting of a dominant or only single isomer, thus enabling the investigation of nanocluster properties as a function of not only the size but also the atomic configuration.

In Chapter 5 and 6 we report proof-of-principle demonstration and progress on the development of a new technology, the Matrix Assembly Cluster Source (MACS). The working principle of the MACS is introduced in Chapter 5. The first MACS apparatus was built and the proof-of-principle of the MACS was demonstrated. Also the effects of different parameters on cluster size and flux were preliminary studied in this chapter. In Chapter 6, we discuss the design and construction of a new MACS system, MACS 1, to scale up the cluster production rate as well as systematically investigated the effects of different parameters on cluster production such as metal concentration, matrix temperature, incident beam energy, so as to discover the cluster formation mechanisms. So far we have achieved an equivalent cluster beam current of ~100nA. Results show that gold and silver clusters produced under controlled experimental conditions show a relatively narrow size distribution even without mass selection ($m/\Delta m \sim 1$). The mean cluster size can be controlled via experimental parameters, especially the

metal concentration in the matrix. Effects of other parameters such as matrix temperature, incident beam energy on cluster size and flux are also investigated. The charge fractions of the clusters were also studied and mass spectra were obtained from the charged clusters using lateral time-of-flight mass selector, further confirming the cluster production and size control in the MACS.

Chapter 7 summarizes the results from all the work and describes the future plans both on fundamental demonstration of nanoclusters and instrument development of the MACS.

The works presented in this thesis are under supervision of Prof. Richard Palmer and co-supervision of Dr. Feng Yin and Dr. Simon Plant as well as a few of collaborators. The respective contributions by the author and collaborators are identified before each chapter.

List of references

[1] Herzing, Andrew A., et al. "Identification of active gold nanoclusters on iron oxide supports for CO oxidation." *Science* 321.5894 (2008): 1331-1335.

[2] Häkkinen, Hannu, et al. "Structural, electronic, and impurity-doping effects in nanoscale chemistry: supported gold nanoclusters." *Angewandte Chemie International Edition* 42.11 (2003): 1297-1300.

[3] Tsunoyama, Hironori, et al. "Size-specific catalytic activity of polymer-stabilized gold nanoclusters for aerobic alcohol oxidation in water." *Journal of the American Chemical Society* 127.26 (2005): 9374-9375.

[4] Palomba, S., L. Novotny, and R. E. Palmer. "Blue-shifted plasmon resonance of individual size-selected gold nanoparticles." *Optics Communications* 281.3 (2008): 480-483.

[5] Hu, Kuo-Juei, et al. "The effects of 1-pentyne hydrogenation on the atomic structures of size-selected Au N and Pd N (N= 923 and 2057) nanoclusters." *Physical Chemistry Chemical Physics* (2014).

[6] Habibpour, V., et al. "Novel powder-supported size-selected clusters for heterogeneous catalysis under realistic reaction conditions." *The Journal of Physical Chemistry C* 116.50 (2012): 26295-26299.

[7] Malola, Sami, et al. "Au40 (SR) 24 cluster as a chiral dimer of 8-electron superatoms: Structure and optical properties." *Journal of the American Chemical Society* 134.48 (2012): 19560-19563.

[8] Xie, Jianping, Yuangang Zheng, and Jackie Y. Ying. "Protein-directed synthesis of highly fluorescent gold nanoclusters." *Journal of the American Chemical Society* 131.3 (2009): 888-889.

[9] Haes, Amanda J., and Richard P. Van Duyne. "A nanoscale optical biosensor: sensitivity and selectivity of an approach based on the localized surface plasmon resonance spectroscopy of triangular silver nanoparticles." *Journal of the American Chemical Society* 124.35 (2002): 10596-10604.

[10] Wyrwa, Daniel, Norbert Beyer, and Günter Schmid. "One-dimensional arrangements of metal nanoclusters." *Nano Letters* 2.4 (2002): 419-421.

[11] Partridge, Jim G., et al. "Formation of electrically conducting mesoscale wires through self-assembly of atomic clusters." *Nanotechnology, IEEE Transactions on* 3.1 (2004): 61-66.

[12] Palmer, Richard E., and Carl Leung. "Immobilisation of proteins by atomic clusters on surfaces." *TRENDS in Biotechnology* 25.2 (2007): 48-55.

[13] Von Issendorff, B., and R. E. Palmer. "A new high transmission infinite range mass selector for cluster and nanoparticle beams." Review of Scientific Instruments 70.12 (1999): 4497-4501.

[14] Pratontep, S., et al. "Size-selected cluster beam source based on radio frequency magnetron plasma sputtering and gas condensation." Review of scientific instruments 76.4 (2005): 045103.

[15] Goldby, I. M., et al. "Gas condensation source for production and deposition of size-selected metal clusters." Review of scientific instruments 68.9 (1997): 3327-3334.

[16] Baletto, Francesca, and Riccardo Ferrando. "Structural properties of nanoclusters: Energetic, thermodynamic, and kinetic effects." *Reviews of modern physics* 77.1 (2005): 371.

[17] Barnard, A. S. "Modelling of nanoparticles: approaches to morphology and evolution." *Reports on Progress in Physics* 73.8 (2010): 086502.

[18] Barnard, Amanda S., et al. "Nanogold: a quantitative phase map." *ACS nano* 3.6 (2009): 1431-1436.

[19] Barnard, Amanda S. "Direct comparison of kinetic and thermodynamic influences on gold nanomorphology." *Accounts of chemical research* 45.10 (2012): 1688-1697.

[20] Sanchez, A., et al. "When gold is not noble: nanoscale gold catalysts." *The Journal of Physical Chemistry A* 103.48 (1999): 9573-9578.

[21] Maier, Stefan A., et al. "Plasmonics—a route to nanoscale optical devices." *Advanced Materials* 13.19 (2001): 1501-1505.

[22] Wu, Yue, et al. "Controlled growth and structures of molecular-scale silicon nanowires." *Nano Letters* 4.3 (2004): 433-436.

[23] Wang, Z. W., and R. E. Palmer. "Direct atomic imaging and dynamical fluctuations of the tetrahedral Au 20 cluster." *Nanoscale* 4.16 (2012): 4947-4949.

[24] Wang, Z. W., and R. E. Palmer. "Experimental evidence for fluctuating, chiral-type Au55 clusters by direct atomic imaging." *Nano letters* 12.11 (2012): 5510-5514.

[25] Li, Z. Y., et al. "Three-dimensional atomic-scale structure of size-selected gold nanoclusters." *Nature* 451.7174 (2008): 46-48.

[26] Wang, Z. W., and R. E. Palmer. "Determination of the ground-state atomic structures of size-selected Au nanoclusters by electron-beam-induced transformation." *Physical review letters* 108.24 (2012): 245502.

[27] Plant, Simon R., et al. "Size-dependent propagation of Au nanoclusters through few-layer graphene." *Nanoscale* 6.3 (2014): 1258-1263.

[28] Plant, Simon R., Lu Cao, and Richard E. Palmer. "Atomic structure control of size-selected gold nanoclusters during formation." *Journal of the American Chemical Society* 136.21 (2014): 7559-7562.

Chapter 2 Literature review

This chapter reviews literatures on the fields related to the works presented in the thesis, including the background of nanoclusters, production methods especially cluster beam technology, introductions of TEM/STEM, a review of theoretical and experimental work on nanocluster structures and applications of the nanoclusters in variable areas.

2.1 Overview of nanoclusters

A nanocluster is an aggregation of atoms from a few tens to millions with a diameter ranging from 0.2 to 20nm and has properties different from the bulk. The field of cluster science was first established in early 80's since the discovery of magic numbers [1-3]. It was found that clusters consisting of certain numbers of atoms exhibit particularly stable atomic and electronic configurations and are therefore observed in higher abundance compared with other size clusters. For example, 13, 20, 55, 309, 561, 923 are the magic numbers of gold clusters and clusters containing these numbers of atoms are much more stable and more easily produced in gas phase [4-9]. The population of magic numbers kept

increasing due to the discoveries of new stable structures both theoretically and experimentally [10-12]. With the development of cluster deposition and characterization methods such as scanning probing microscope (SPM), transmission electron microscope (TEM) etc., the experimental and theoretical work of cluster structures and related properties have emerged [13-16].

Clusters exhibit remarkable properties and have demonstrated their potential in technological applications across a wide range of fields as their properties are strongly dependent on their size [17-20]. Small clusters are widely used as catalysts to accelerate and select chemical reactions and their catalytic activity is found dependent on their size [21]. For example, Pt clusters deposited on MgO surface are used as catalyst for the oxidization of carbon monoxide, which was first demonstrated by U. Heiz et al. in 1999 [22]. The efficiency of CO_2 production (CO_2 per Pt atom) varies greatly with the size of the Pt clusters. Similar to the Pt clusters, small Au clusters can also be used as catalyst for oxidization of CO [23]. Moreover Au and Pt clusters can be used as catalyst for the oxidative dehydrogenation of hydrocarbons such as propane [24]. In nanofabrications, size-selected clusters are used as the mask for dry plasma etching to create nanoscale structures on semiconductors surface, such as nanopillars on a silicon surface demonstrated by Palmer and co-workers [25]. The silicon substrate is etched by an ECR plasma of SF_6, and the mean size of the pillar is determined by the chemical species of the deposited clusters. For example, Au, Ag and Cu clusters with the same diameter deposited on the substrate create pillars with different sizes. In the biological field, large size-selected clusters deposited on surfaces can function as the anchor sites for the immobilization, separation and

orientation of protein molecules due to the covalent bonds formed between proteins and clusters, offering the opportunity to make microarray biochips [26-27]. Additionally, clusters are widely used in optical devices for their function of amplifying the signal [28-30]. For example, in Raman spectrum, the Raman scattering cross sections are enhanced greatly if the analysed molecule is absorbed on Ag clusters because of which the electronic properties of the molecule are changed and the excitations in the molecule and metal enhance the resonance and local electromagnetic fields [31-32].

2.2 Review of cluster beam deposition methods

Cluster beam deposition is an ultra clean process has incomparable advantages in production of nanostructural materials and is of primary importance for the development of nanotechnology in industry [33-36]. The cluster beam depositon of nanoclusters has been demonstrated not only suitable for fundamental research but also has the potential in scaling up the production rate of nanoclusters with highly controlled properties [35][38-45].

The formation of nanoclusters in cluster beam deposition approach is in the gas phase and the critical parameter is the cross section of collisions between gas atoms, cluster atoms and clusters [46-48]. In a typical cluster source the clusters are formed by cooling down atomic vapor with injected cold condensation gas (e.g. helium), where the collisions promotes the atomic vapor to condense into clusters. The size distribution of clusters produced in gas phase is determined by several parameters such as the saturation of the atomic vapor and pressure

and flow rate of inert gas, as well as the condensation length [49-52]. The cluster generation chamber usually can be cooled using liquid nitrogen to reach a temperature below 100K to favor the condensation of large clusters [53]. The flux and the size of clusters increase with a denser atomic vapor in certain range. However, in some cases, the atomic vapor can be too dense to be cooled by the inert gas flow. The pressure of gas in the condensation chamber also affects the production and size distribution of clusters as high inert gas pressure boosts the condensation of large clusters. The significant increase in the detection of clusters at high condensation gas pressure is probably due to two reasons: (a) more clusters are swept out of condensation chamber by higher gas flow, and (b) the ionization efficiency of clusters is greatly increased at high pressure.

2.2.1 Mechanism of cluster formation in gas phase

The cluster formation process in the gas phase can be separated into two steps: nucleation and growth [54]. At the nucleation stage two body and three body collisions are eliminated, as the kinetic energy of atomic vapor is much higher than the bonding energy. The classical nucleation theory can be used to explain the nucleation model where the change of Gibbs free energy ΔG including contribution of both surface and volume is considered. The change of Gibbs free energy of system is

$$\Delta G = 4\pi r^2 \sigma + \frac{4\pi r^3}{3} \Delta G_v$$

where σ is the surface tension and ΔG_v is the Gibbs energy per volume [54]. To simplify the equation, the nucleus is treated as a perfect sphere with atomic volume of V_L and radius r. In the gas phase, the Gibbs energy per volume ΔG_v is

$$\Delta G_v = -k_B T ln(P_v/P_s)/V_L$$

where P_v and P_s are the pressure of vapor and saturation vapor at temperature T respectively and k_B is the Boltzman constant. The critical radius r_c is the radius of nucleus when system reaches the equilibrium state, $d\Delta G/dr=0$, and

$$r_c = \frac{2\sigma V_L}{k_B T ln(\frac{P_v}{P_s})}$$

The nucleus is stabilized by evaporating atoms when $r<r_c$ and by growing bigger to reduce the Gibbs free energy when $r>r_c$ [36]. At a certain temperature, the critical radius varies with the vapor pressures and it decreases with the increasing supersaturating pressure.

The growth model used to explain the growth of nanoclusters when $r>r_c$. It includes two mechanisms: surface growth by adsorption of atoms and coalescence [55]. Surface growth usually induces chemical reactions or phase change of the cluster surface as the cluster is already formed before atoms approaching. Coalescence is that clusters growing by collision between clusters via mechanism of Brownian motion [56]. At the early stage of cluster growth the surface growth is important and keeps contributing throughout the entire growth process. The whole growth process continues until the end of

condensation chamber and the surface growth mechanism is more dominant according to simulation by Hihara and Sumiyama [56-57].

2.2.2 Cluster source

Generally, cluster beam source can be categorized based on the cluster generation or beam formation mechanism such as thermal heating, laser ablation, magnetron sputtering [36]. Except for the clusters produced by ion sputtering, an ionization stage is mounted on the cluster source to produce charged particles for size selection or controlled deposition [58].

Thermal heating

The working principle of the thermal heating cluster beam source is that materials are heated in a high temperature crucible to generate an atomic vapor, which is similar to molecular beam epitaxy (MBE), but using a higher intensity thermal source [59-60]. The cluster formation process in the thermal heating source is realized by mixing the atomic vapor with high-pressure condensation gas.

A great example of thermal heating cluster source is the seeded supersonic nozzle source as shown in Figure 2.1, where materials are heated to high temperature to generate an atomic vapor then mixed with condensation gas at high pressure, usually several times higher than atmospheric pressure, which expands into a high vacuum via a conical shape nozzle to form a supersonic molecular beam [34,61]. The expansion is adiabatic which causes rapid cooling

of the mixture of atomic vapor and inert gas. Clusters are formed from the supersaturated atomic vapor and the growth process continues until far away from the nozzle when the pressure of atomic vapor is too low for interactions to take place between two clusters. Usually small clusters can be stabilized by the cooling provided by the supersonic expansion, but it might be not enough for large clusters such that evaporation of one or more atoms is inevitable for stabilization.

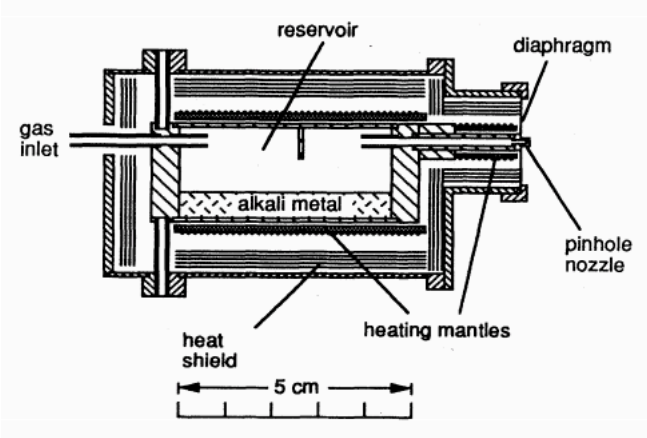

Figure 2.1 Seeded supersonic nozzle cluster beam source, reproduced from reference [34].

The seeded supersonic nozzle source is powerful enough to produce continuous and intense cluster beams of up to 10^{18} atoms/s for low melting point materials [62]. Because of the high consumption of material, most seeded supersonic nozzle sources have a relatively large size oven to avoid frequent refilling, which restricts the maximum temperature below 900K. The size of clusters produced in this source is determined by several parameters such as the oven temperature, inert gas pressure and the size of the nozzle. Usually the size of clusters

produced in the supersonic nozzle source ranges from two atoms to several hundred atoms. Clusters with several thousand atoms were also reported for this type of cluster source with very careful design and highly optimized experimental conditions. Likewise the type of the condensation gas also affects production and size of clusters. The growth of clusters lasts longer using a heavy inert gas because of its large cross section of collisions. In summary, despite of the high flux of clusters produced by the seeded supersonic nozzle source, this source is restricted to the production of small size clusters from low melting point materials (such as alkali metal). Also further ionization devices are needed for size selection since the clusters produced based on this mechanism are neutral.

Laser vaporization source

The laser ablation source (also known as the Smalley source) was first introduced by R. E. Smalley in early 1980's and has become one of the most popular methods to make clusters after 30 years' development [63]. The laser ablation source is designed to produce clusters from any type of metals, as well as non-metals such as carbon, silicon and some semiconductor conductors like GaAs [64]. In the laser ablation cluster source, high density atomic vapor of cluster material is created by focused laser probe in a short time and well-localized regime. Clusters are then produced by rapid quenching of the plasma [65-66]. In most of the laser ablation cluster sources, high power pulsed lasers are used and the density, size distribution and structures of clusters produced by the laser ablation source are affected by the ablated material, buffer gas as well as the time for cluster to resident before expansion.

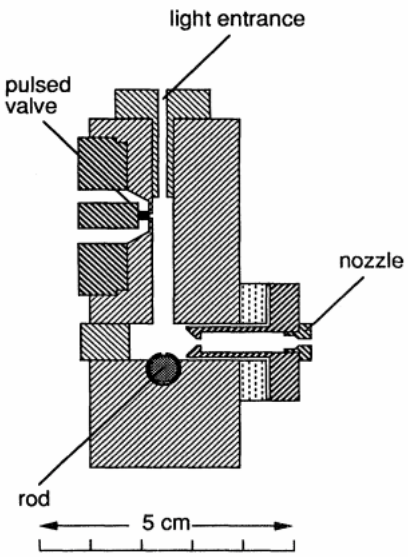

Figure 2.2 Laser ablation cluster source developed by P Milani, reproduced from reference [66].

The schematic diagram of the laser ablation source developed by P Milani is shown in Figure 2.2 [66]. As shown in the figure, the vaporization volume in the laser ablation source is smaller than thermal source and plasma source. The pulsed laser is incident from the top and focused on the target to vaporize a small amount of material, which is then mixed with pulsed injected inert gas to promote the formation of clusters by quenching. Then the mixture expands into vacuum to form cluster beam through a nozzle at the end of the chamber [67]. The geometry of the entrance of injected inert gas and target is important here as it might affect the formation and growth of clusters, because long channel nozzle promotes the formation of clusters. On the other hand, part of clusters might be lost by condensing on the walls of the channel. To overcome this problem, a cavity is introduced into most of the laser ablation sources to minimize the clusters' deposition on the wall with carefully designed dimensions. The shape of

the target used in the laser ablation source varies, such as disc or rod. The target is usually mounted on a rotation gear ensuring the uniform consumption of the surface [68].

The size distribution of clusters produced in the laser ablation cluster source can be controlled by the inert gas pressure and the condensation time of clusters remaining in the source. It has been demonstrated that large amount of monomers are formed at low gas pressure, while large clusters are more favored at high pressure [69]. Conversely to the continuous beam produced by the thermal evaporation, the laser vaporization source produces a pulsed beam but the overall production is as high as the evaporation source. The material consumption in the laser vaporization source is much lower because the use of a pulsed laser avoids heating the sample continuously. Clusters can be produced from a wider variety of bulk materials using laser vaporization, but the thermal sources (evaporation source and supersonic source) are only restricted to low melting point metals and few noble metals. With special design, some complicated clusters can also be produced by using laser vaporization sources, such as oxide, alloy and clusters surrounded with molecular ligands, produced in a cutaway source (a special type of the laser vaporization source) [64,70]. Although the clusters produced by the laser vaporization source are probably ionized during vaporization and collision processes, an ionization device is still needed for the detection of clusters.

Magnetron sputtering gas condensation cluster source

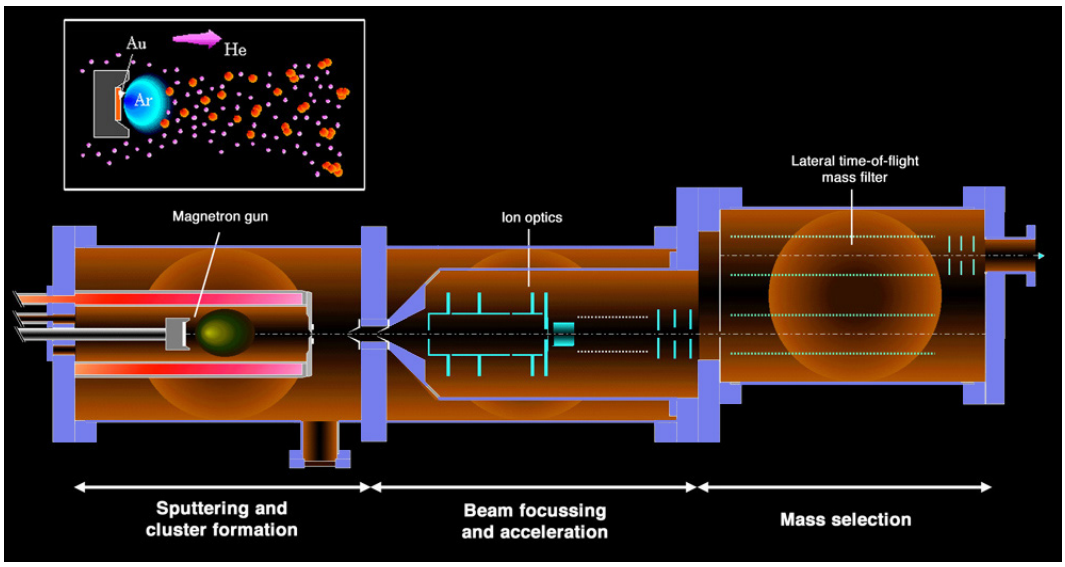

Figure 2.3 Magnetron sputtering gas condensation cluster source combined with lateral time-of-flight mass filter, reproduced from reference [74].

The magnetron sputtering gas condensation cluster source, also known as the Haberland source, combined with plasma sputtering techniques and gas condensation, is capable of producing continuous high density cluster beam of various materials including metals, semiconductors and insulators [71]. The clusters are produced by sputtering the bulk target with plasma to generate atomic vapor which is then condensed in the cold inert gas atmosphere [72]. A significant proportion of clusters produced by the magnetron sputtering are already ionized, around 30%, therefore no further ionization device is needed [73]. The size selection can be achieved by cooperation with ion optics and mass filter. Clusters with a wide size range from 2 to 70,000 atoms can be produced by this type of source. The schematic diagram of the conventional magnetron sputtering cluster source combined with mass selection system is shown in

Figure 2.3 [74]. Typically it consists of three high vacuum chambers for cluster generation, ion optics and mass selection respectively. Size selected clusters are deposited onto a substrate in the deposition chamber mounted after the time-of-flight mass selector.

The plasma sputtering takes place in an inner chamber, which can be cooled by liquid nitrogen, inside the generation chamber. The target is mounted in front of a magnetron gun, which is usually movable in a linear direction parallel to the chamber's axis allowing us to change the distance between the gun and the end of the inner chamber. The sputtering gas is directly injected to the front of the target from small orifices around the magnetron head. Both DC power and RF power can be applied to the magnetron gun [75]. DC sputtering is only suitable for conductive target because a large negative voltage is applied to the target igniting Ar gas into plasma. The Ar plasma is always more positive charged than negative because of its screening effect. The large negative voltage on the target provides a strong electrical field accelerating Ar plasma to bombard the target. For RF sputtering, both conducting and insulating targets can be used. The Ar gas is ignited to form plasma by the RF high voltage coupled to the target. The high RF voltage creates a cyclic attraction and repulsion of plasma on the target. This causes more negative charges to remain on the target because of the greater mobility of electrons building up a strong attraction to the positive plasma. Supersaturated vapors of atomic ions as well as some small clusters are produced in front of the target by the magnetron sputtering.

The condensation takes place in the rest of the inner chamber by introducing the He gas. Clusters with a wide size distribution mixed with the gases leave the inner chamber through an adjustable nozzle at the end. Given that 30% of clusters are already ionized to the plasma, no further ionization device is needed to generate an ion beam. The size range of clusters produced in the magnetron sputtering source is determined at the condensation stage, which is mainly affected by the gas pressure directly dominating the sputtering and condensation processes [49,76]. Two different gases are used in the sputtering gas condensation source: Ar and He. The Ar gas is used for the sputtering and generally a higher Ar pressure induces a higher sputtering rate. Thus large quantity of Ar gas is necessary to produce large clusters as they might require a higher concentration of sputtered atoms. The effects of the He gas in the magnetron sputtering source are more complicated. Similar to the inert gas in other cluster sources, the He gas is responsible for the growth of clusters, which provides cooling and collision for clusters condensation. Experimental results show clusters produced without He gas in a magnetron sputtering source are limited to a small size of 10 atoms or sometimes 20 atoms. The clusters growth process in the magnetron sputtering sources can be simply divided into two steps: sputtered atoms are cooled in He gas to form small cluster seeds; the seeds then grow into large clusters by collision with other sputtered atoms and small clusters [77]. Therefore, the He gas not only assists condensation of large clusters from seeds by collision, but also creates seeds which are small clusters [78]. The size distribution shifts towards smaller sizes when more seeds are produced at high He pressure. Sputtering power and aggregation distance also affects the size distribution. Inadequate sputtering power causes low production

rate of clusters and large clusters may not be formed. However, high sputtering powers can be unstable and might lead to a discontinuous cluster beam. Clusters are aggregated in the region between the magnetron gun and the nozzle. A minimum distance of 10cm is required for plasma ignition. A large aggregation distance in an optimum range enhances the production of large clusters.

The magnetron sputtering cluster source has several advantages over other cluster sources. The clusters produced by magnetron sputtering are already ionized at a notable proportion (~30%), such that the ion optics and mass filter can be fitted directly after generation chamber. Compared with the seeded supersonic nozzle source and evaporation source, clusters of a wide range of materials and sizes can be produced by the magnetron sputtering source. Unlike the pulsed beam used in the laser vaporization source, the cluster beam produced by the magnetron sputtering source is continuous and the maximum beam current of size selected cluster is up to several nano amps.

2.2.3 Other synthetic methods for cluster production

There are many other types of source apart from the thermal heating source, laser ablation source and sputtering source to produce nanoclusters from a physical vapour such as a pulsed microplasma cluster source and arc discharge source. Compared with the sputtering source, a pulsed microplasma cluster source is more suitable for stable operation as the atomic vapor is generated by a spatially confined plasma ablation of the target and clusters are formed by

aggregation in pulsed injected inert gas phase [79-81]. However the critical issue of the pulsed microplasma source is that the cluster beam flux is limited [46].

Another type of pulsed cluster source to produce highly ionized metal plasma is the arc discharge source where a discharge happens between two conductive electrodes to generate an atomic vapor. The arc discharge source has been considered as the replacement of laser ablation source in 1990 by Meiwes-Broer et al [82-83]. The principle of the vaporization by arc discharge is that large current emitted from the cathode due to thermionic and field emission induces the heating on the entire or small part of the cathode to vaporize materials. The discharging current can reach up to 10^5A for short time intervals. Clusters are formed by the vaporized materials or plasma which condense in the surrounding buffer gas introduced from a pulse valve [84-85].

Also clusters can be produced by chemical synthesis in which metal or semiconductor salts are used, and therefore it is versatile and usually inexpensive compared with the physical routines [86-88]. The early study of clusters produced via colloidal synthesis was reported by Faraday over 150 years ago [89]. Typically in chemical synthesis process nanoclusters are formed in the supersaturated salt solutions which is reduced subsequently. The size, shape and even crystalline of the nanoclusters can be controlled through the conditions of the solution such as PH or concentration of the ions. The nanoclusters synthesized in solution have great advantages if their applications are required to be carried out in solutions [91].

2.3 TEM and STEM

2.3.1 Overview of TEM and STEM

The first transmission electron microscope (TEM) was developed my Nobel Laureate (1986) Ernst Rusk and Max Knoll in 1932 where they successfully transferred the principle of optic microscope to electrons [92]. The resolution has been improved significantly with the electron microscope due to the wavelength of electron is subnanometer instead of hundreds of nanometer of visible light. Also the wavelength of electrons can be further shorten by accelerating the electrons as the wavelength λ is determined by momentum of the electrons p which follows the equation $\lambda=h/p$ proposed by de Broglie in 1925. According to the relativistic correction, the momentum of electrons is defined by $p=(2m_eV+eV^2/c^2)^{1/2}$, thus wavelength of electron accelerated by 200kV is 10-3nm [93]. The first scanning transmission electron microscope was developed my Manfred von Ardenne in 1938 where the sample is raster by a focused electron beam instead of the parallel electron beam in conventional TEM. The development of the STEM has enabled various techniques in the electron microscope such as annular dark field (ADF) imaging, Electron Energy Loss Spectroscopy (EELS) and Energy Dispersive X-ray (EDX) mapping [94].

The spatial resolution of the STEM is defined by the tip size of the electron probe on the sample, which is focused by objective lenses after electron gun and prior to the sample [95]. In early days the resolution of the STEM was limited by the positive spherical aberration when using round electron lenses pointed by

Scherzer [96]. To overcome this problem, the non-rotationally symmetric corrector was introduced into the STEM by Scherzer in 1947, where a negative aberration is generated deliberately to neutralize the positive aberration induced by round lenses [97]. With the help of manufacture of the aberration corrector, the resolution of STEM has been improved to a new era not only the spatial resolution but also the depth sectioning resolution. The spatial resolution of an state of the art STEM with aberration corrector has already been below 1 Angstrom and is pushing to nearly 0.5 Angstrom [98-99].

The great advantage of electrons is the wave-particle duality where the wave behavior enables the formation of images and diffraction patterns revealing the internal structures while the particle behavior facilities the interactions between electrons and specimen exposing the chemical properties. Generally the electron scattering can be divided into two groups, elastic scattering and inelastic scattering or coherent scattering and incoherent scattering. The difference between elastic and inelastic scattering the energy loss, which is important to reveal the chemical properties of specimen. The coherent and incoherent scattering is distinguished by whether the interference pattern can be formed by the scattering waves. Most elastic coherent scattering happens with relatively small scattering angles from 1 to 10 degree due to the Coulomb interaction between the electron cloud and incident electron beam [93]. The differential patterns, containing structure information of the material, are generated by the coherent electrons plane penetrating the specimen that forming the secondary spherical wavelets due to the low angle scattering by each atom. The high angle scattering with angle more than 90 degree is usually incoherent caused by the

Coulomb attraction from the nucleus. The interaction between nucleus and incident electron beam can be described by Rutherfold scattering that the differential cross section is given by the equation

$$\sigma_R(\theta) = \frac{e^4 Z^2}{16(4\pi\varepsilon_0 E_0)} \frac{\mathrm{d}\Omega}{sin^4 \frac{\theta}{2}}$$

where θ is the scattering angle, E_0 is the energy of the electron, Ω is the solid collection angle, Z is the atomic number of the specimen and ε_0 is the permittivity of free space. According to the equation, the differential cross section is increased with higher atomic number. Inelastic scattering is nearly always incoherent as energy varies but it contains valuable signals such as secondary electrons, X-rays, phonons, plasmons etc. Second electrons are the electrons knocked out from the specimen by the high energy electron beam, could be from conduction and valence band and inner shells. The X-rays generated in the electron microscope are two different types: Characteristic and Bremsstrahlung X-rays. Bremsstrahlung X-ray usually appears as the background due to the deceleration of the electrons by metal target. Characteristic X-ray normally presents two sharp peaks containing element and structure information is generated by the electrons transition between lower atomic energy levels in heavy elements. Phonons are generated due to the electron induced excitation. Plasmon is usually occurred in metals that waves are excited by high energy incident electrons in the loosely bound outer layer electrons [93].

2.3.2 Basic components in STEM

Electron gun

Nowadays most electron gun used in electron microscope is field emission gun (FEG) instead of the thermionic source as electrons generated in FEG are more monochromatic [93]. In the FEG electrons are generated by applying an intense electrical field. Usually the electron gun is made of W or LaB_6 etc, which have high melting point or low work function that electrons can easily escape from the conduction band. The electron gun is installed in an UHV chamber to avoid contamination and oxidation. A typical FEG contains two anodes in front of the gun which acts as the cathode. The first anode is biased to several thousand volts relative to the electron gun tip providing the extraction field to attract electrons out of the gun. The second anode is used to accelerate electrons also to make a crossover of the electron beam working as an ion optic lens which affects the electron beam size and position.

Magnetic lenses

In electron microscope magnetic lenses are used to focus electrons instead of electrostatic lenses as they are not frightened to high voltage breakdown [93]. The movement of electrons in magnetic field is driven by Lorentz force F, which follows the equation

$$F = -e(E + v \times B)$$

where E is the strength of electric field, B is the strength of magnetic field and v is the velocity of the electrons. The schematic diagram of a typical magnetic lens is shown in Figure where a coil of copper wires is surrounded inside of the pole piece made of soft iron. The magnetic field is created in the bore of the pole piece

by applying current through the coils. The strength of the magnetic field is not homogeneous that it's stronger close to the bore while it's weaker in the center and that's how the focusing works by deflecting electron towards center less than those away from the axis.

Resolution and Aberration correction

The theoretical resolution limit of the STEM can be calculated using the Rayleigh criterion where the smallest resolvable distance δ is a function of the wavelength of the incident radiation λ,

$$\delta \approx 0.61\lambda$$

In the STEM, the incident radiation is the de Broglie wavelength of high energy electron beam that

$$\lambda_{dB} = \frac{h}{\sqrt{2meV(1 + \frac{eV}{2mc^2})}}$$

Therefore, the de Broglie wavelength of electron beam at V=200kV using this equation is λ_{dB}=2.5x10^{-3}nm, which giving a smallest resolvable distance δ~1.5x10^{-3}nm.

In reality, however, the imaging resolution in the STEM never reaches close to the theoretical value and the main reason is the spherical aberrations. In the STEM the spherical aberration is induced by the circular lenses as the focal point of the electron beam varies with the distance from the center the lens. To overcome this problem, the non-rotationally symmetric corrector was first

introduced into the STEM by Scherzer in 1947, where a negative aberration is generated deliberately to neutralize the positive aberration induced by round lenses.

Two different types of aberration correction systems are available commercially, the multiple quadrupole and octupole lenses from Nion, which has the advantage to correct the axial chromatic aberration but its non-rotationally symmetric lenses are too complicated and hexapole and other transfer lenses from CEOS where a round lens doublet is placed in the middle of a pair of hexapole lenses. The principle of the aberration corrector is pre-diverge the electron beam to compensate the aberration induced by objective lenses [100-102].

ADF and BF Detectors

Detectors in the electron microscope can be semiconductor detector, CCD camera, scintillator-photomultiplier detector etc plus a viewing screen made of doped ZnS to direct see the electrons via green fluorescence [93]. ADF detector is the scintillator-photomultiplier detector coated with Al. Photons are generated in the scintillator, normally made of Ce-doped yttrium-aluminium garnet, when hit by incident electrons leading to the photoelectric effect at the entrance of the photomultiplier tube (PMT) where electrons are multiplied up to 10^8. The principle of BF detector is similar but using a round detector instead of the annular detector. The collection angle of both ADF and BF detector are determined and can be tuned by the electron optics after specimen such as camera length. HAADF detector is the ADF detector but collecting high angle scattered electrons.

2.3.3 Image formation in STEM

The image formation mechanism in STEM is different from that in TEM where the focused electron beam probe is rustling the specimen replaced of parallel beam [93]. The major difference in STEM from TEM is the incoherent electrons which enables the quantitative imaging in STEM with higher resolution than TEM. In the STEM the wavefunction of the electron beam probe is the sum of all partial plane waves given by

$$p(r) = \int A(u) \exp[-i2\pi u \cdot r]\, du$$

where A(u) is the complex aperture function following the equation

$$A_c(u) = H_c(u) \exp\,[i\chi(u)]$$

The $H_c(u)$ here is the circular top-hat function with unit height, $\chi(u)$ is the phase shift which depends on the aberration of the objective lens not only leading to the rotationally symmetric aberration but also non-symmetric aberrations. The specimen in STEM can be look as a self-illuminated object under electron beam with wide range of angles, which can be treated as a convolution intensity model mathematically rather than complicated amplitude, where the intensity following the equation

$$I_{incoherent}(r) = |p(r)|^2 \otimes |O(r)|^2$$

O(r) here is the object function of the specimen. The resolution of the STEM image is strongly dependent on the electron probe size and atomic resolution has been achieved with the help of aberration corrector. This technique has the

advantage that intensity of the atomic column has linear relationship with its thickness up to very large thickness which enables the date to be interpreted more directly. The scattered electrons collected by ADF detector follow the Rutherford scattering model where the intensity of the electrons is proportional to Z^2. However in reality, the power exponent is varied with camera length between 2 and 1.5 due to the screening effect at low angles [103-106].

2.4 Review of Cluster structures

2.4.1 Shell structures and magic numbers

The Mackay icosahedral is a great example explaining the shell structure [107], where 12 atoms are arranged to surround the central atom or all atoms are at the corners of an icosahedral, which contains two shells for the former and only one shell for the latter. In both cases, another layer of 42 atoms can be added on top of these 13 atoms core again to form a larger perfect icosahedral consisting of 55 atoms, which is known as one of the magic numbers of the Mackay icosahedral and experimentally agrees well with rare gas clusters [108-109]. Another example is the tetrahedron, where 4 atoms compose the core or the first shell. However unlike the icosahedron, adding one more complete layer to the tetrahedron actually results in four more shells instead of one.

As mentioned before, the discovery of magic number boosts the development of cluster science. Magic number is the total number of atoms consisted in a more favored structure and geometrically a complete shells set. The Shell index K is

used to define the number of shells in a specific geometry and the central atom is labeled with K=1 [110]. The equation of total number of atoms in most commonly observed geometries as a function of shell number is summarized below [111].

$$n = \frac{1}{6}K^3 + \frac{1}{2}K^2 + \frac{1}{3}K \ (tetrahedron)$$

$$n = \frac{10}{3}K^3 - 5K^2 + \frac{11}{3}K - 1 \ (\ Mackay\ icosahedron)$$

$$n = \frac{5}{6}K^3 + \frac{1}{6}K \ (decahedron)$$

$$n = \frac{10}{3}K^3 - 5K^2 + \frac{11}{3}K - 1 \ (truncated\ decahedron)$$

$$n = \frac{2}{3}K^3 + \frac{1}{3}K \ (octahedron)$$

$$n = \frac{10}{3}K^3 - 5K^2 + \frac{11}{3}K - 1 \ (cuboctahedron, triangular\ faces)$$

$$n = 16K^3 - 33K^2 + 24K - 6 \ (cuboctahedron, hexagonal\ faces)$$

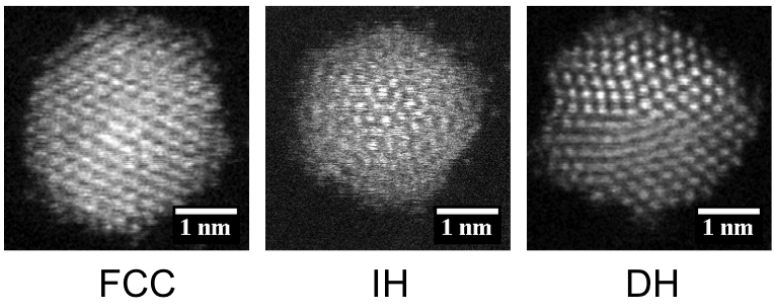

Figure 2.4 The HAADF images of Fcc, Ih and Dh structures observed in Au_{923} clusters.

In this section, we will mainly introduce three high symmetry structures, Fcc, Ih and Dh including limited variations such as Ino-Dh and Marks-Dh [112-115],

which are the dominant proportions observed in our structure control work on size selected Au_{923} nanoclusters as shown in Figure 2.4.

2.4.2 FCC

Fcc is the most closed parking (0.74) and most common structure observed in bulk crystals. Nanoclusters with fcc structures can be treated as a fraction of the bulk. Fcc exhibiting in nanoclusters or microscale particles via controlled growth contains various geometries such as cube, truncated cube, cuboctahedraon, truncated octahedron and octrahedraon. The Wulff construction, proposed by Marks [115], is believed to be the role followed by nanoclusters in equilibrium state fulfilling the equation [116],

$$\frac{\gamma(100)}{\gamma(111)} = \frac{d(100)}{d(111)}$$

where γ(100) and ϒ(111) are the surface energy of (100) and (111) facets and d(100) and d(111) are the corresponding distance between the facets and the center of cluster. Different geometries with fcc structures are able to transfer from one to another via mechanism of selective growth of cutting on specific facets and the shape of face of all fcc geometries are limited to square, triangle and hexagonal [116].

2.4.3 Icosahedron

Icosahedron clusters with 12 5-fold axes are never expected to grow to crystals as it doesn't match with the translational crystal symmetry. However, microscope studies by Ino et al. have shown the observed icosahedral gold nanoclsuters contain six 20 tetrahedra, which can be cut from fcc structure, sharing a common vertex in the center [112]. As tetrahedral is not the space filling structure, in the icosahedral nanoclusters the tetrahedral units usually have twin boundaries with the neighboring units (multi twinned particles) where the (111) facets of tetrahedra are exposed and crystallographical (111) facets are shared by two adjacent tetrahedral units, which makes to the inner three sides of each tetrahedral units are about 5% shorter than the side of tetrahedral units on the surface [117]. The icosahedral structure in nanoclusters was first reported by Mackay over 50 years ago when two icosahedral shell structures were introduced, Mackay icosahedral and double Mackay icosahedral and the latter has been corrected to anti-Mackay in early 2000's by Kuo et al. [118]. The Mackay and anti-Mackay are distinguished by the positions of the landed the adatoms. For Mackay icosahedron, adatoms are deposited on the site of FCC while for anti-Mackay adatoms are placed on HCP (hexagonal closed parked) [118]. Icosahedral is energetically favored at the early stage of cluster formation as reported based on calculations by theorist and the formation mechanism of icosahedral by rapiding cooling, freezing and melting has been argued for long time [119-122]. Baletto et al. have shown the theoretical study of growth of silver clusters where icosahedral can be formed at low temperature but then transform to decahedral due to thermal annealing [123]. In addition to the Mackay and anti-Mackay icosahedral, a large amount of variants have been found and reported in literature, such as Chui icosahedral where the icosahedral

decorated with crater on each corner and it is suggested to be more stable and thermodynamically realistic especially for large size clusters [124-126].

2.4.4 Decahedron

Apart from the icosahedral, another 5-fold symmetry structure often observed in nanoclusters is the decahedral. The regular decahedral consists of five tetrahedral units which are packed together and four equilateral triangle (111) facets of each tetrahedral are slightly distorted that two of these facets are shared with other units as twinning planes while the other two are turned into the surface of the decahedral [127]. The strain energy in decahedral is lower compared with that in icosahedral owing to the lower strain in tetrahedral units. Also the stain energy in decahedral can be minimized by varying the shape and size of the units. For example, the regular decahedral is not favorable in the experiments as it's non-spherical shape [128]. Although the atoms on the regular decahedral surface are closely-packed, the surface area of the decahedral is extremely large besides the internal strain. However, the decahedral can be truncated to become more spherical such as Ino-decahedral and Marks-decahedral that have been observed experimentally in nanoclusters. (100) facet are exposed on the truncated surface instead of closely-packed facets.

2.4.5 Review of theoretical work on nanocluster structures

The structure preference in nanoclusters is determined by the energetics especially for the structures with lower energy. From theoretical calculations

reported in literature by Baletto and Ferrando [129], the common investigation of the most favored structures in nanoclusters can be divided into two steps. Firstly a model is introduced to represent the interactions between the elementary constituents in the clusters where the Schrodinger equation is solved directly and the constructions of semi-empirical inter-atom potentials are involved. Secondly, a global optimization algorithm is applied to seek for the most favored isomers [116].

The most critical part here is the choice of the energetic model, which directly affects the accuracy of the calculation and there is not an ideal model that could deal with all the cases. For example, the ab initio quantum chemistry method provides exact solutions for most of the small clusters but it becomes unmanageable with increasing the nanocluster size . Methods based on density functional theory (DFT) are widely used in the structural calculations since 1990s and are believed to be accurate and less cumbersome after adequate test [116]. Although the exchange and correlation interactions in the DFT methods are refined approximately and greatly, there are still limitation for the DFT such as the lacking of intermolecular interactions in which case the position of atoms or molecules are not replaceable and the exclusion of thermodynamics, which means all the calculations are run at 0K. Semi-empirical methods, improved from the Hartree-Fock formalism that have been successfully used in organic chemistry before, are now also used to build the approximate energetic models in nanostructures [130]. For semiconductors and metals, there is the tight-binding model method with intermediate computational effort based on the wave functions [131]. The potentials between atom and atom or molecule and

molecule calculated based on the approximate quantum models can be then used in large clusters or large crystals by fitting with experimental properties of the materials via several methods such as EAM (embedded atom method), SMATB (second movement approximate to tight binding) or Sutton-Chen potentials [133]. The binding energy of a cluster can be described by the equation,

$$E_{binding} = aN + bN^{2/3} + cN^{1/3} + d$$

where *N* is the total number of the atoms containing in the cluster. The first term *aN* is attributed to the volume effect and the rest of the equation corresponds to the surface effect of facets $bN^{2/3}$, edges $cN^{1/3}$ and vertices *d*. *Δ(N)* is introduced to represent the stability of the clusters by figuring out the excess energy per surface atom with total *N* atoms in the perfect crystal,

$$\Delta(N) = \frac{E_{binding} - N\varepsilon_c}{N^{2/3}}$$

where ε_c here is the cohesive energy per atom in the crystal [116].

EAM is one of the popular theoretic method reported by many scientists such as Grocholar, Feiglto et al. to simulate the initial nucleation, coalescence and growth kinetics especially for gold nanoclusters synthesized in gas phase [134]. The simulations based on the EAM method have shown that the coalescence prefers to form decahedral and fcc structures for gold nanoclusters of less than 300 atoms at the early stage. Other parameters like aggregation rate and type of condensation gas do not affect the statistical structures much. The EAM simulations also show the probability to form icosahedral structure is highly

related to the size of the initial seed and temperature, and it decreases with increasing seed size whilst increased with raising temperature [135].

An interesting study of nanoclusters growth in liquid using both Molecular Dynamics and hybrid Monte Carlo method are reported by Desgranges and Delhommelle to simulate the nucleation of gold nanoclusters, where the growth of the nanocluster is attributed to the continuous cross-nucleations of two polymorphs [136]. They also found the nanoclusters are dominated by fcc structures at small size but when it's approaching the critical size, HCP structures start nucleating on the surface heterogeneously [137]. The famous microscopic mechanism study on growth of nanoclusters reported by Baletto et al., has indicated the icosahedral and decahedral are more favored in nanocrystalline structures of meta-stable silver nanoclusters at low and intermediate temperature between 350K and 500K. The icosahedral isomers are formed via the mechanism of shell by shell growth mode or the structural transformation from decahedral [123]. In Baletto's other work, silver nanoclusters with different size up to about 150 atoms are studied showing at extreme temperatures (both high and low) icosahedral is more preferred while decahedral is favored at the intermediate range [138]. It has also been presented that for gold nanoclusters where the immersion environment is found to have effects on the growing process [139].

When size of nanoclusters increases, the effect of the strain especially for multi-twinned nanoclusters becomes notable. Theoretical studies based on the surface energy, boundary energy and elastic strain energy including Ino's calculation

show that icosahedral gold nanoclusters are stable when size is smaller than 43.6nm whilst decahedral is 396.1nm [112]. Surface disorder also plays a critical role in the structures of nanoclusters as reported by Chui et al [126]. Simulations based on the energetics of nanoclusters by Baletto et al., predicted the structural transformations among icosahedral, decahedral and fcc in gold nanoclusters, that is icosahedral starts transforming into decahedral or fcc when the size of nanocluster is less than 100 atom and the transformation from decahedral to fcc starts at about 500 atoms [129]. Similar to gold, Ni icosahedral nanoclusters follow the same trend with increasing cluster size as investigated by Cleveland et al. The phase map of gold nanoclusters less than 30nm in diameter was calculated by Baletto et al. based on the first principle [127,140]. Also the roles of the substrate on nanoclusters structure cannot be neglected, for example transformation from decahedral to icosahedral is observed on clusters deposited on silica surface [20, 141].

Heating also plays a role in the structural transformation in nanoclusters because cluster surface softens upon heating, reconstruction happens during the heating and a liquid skin or quasi-molten state might be formed before the clusters are fully melted [142-145]. Pt and Pd nanoclusters have been studied as examples for heating effects based on EAM simulations by Schebarchov et al., which show the decahedral isomers of Pt_{887}, Pt_{1389} and Pd_{887} is turned into fcc before the melting point [146-147]. On the contrary, the freezing process is intended to form icosahedral as explored by Chushak on Au_{1157} with a cooling rate of $3x10^{11}$ K/s [148]. The structures based on crystallization process are also

investigated by various groups showing crystallization starting at the surface dominates the later crystallization process [149-151].

2.4.6 Review of experimental work on nanocluster structures

Most of the observations of structures of nanoclusters in experiments are achieved by electron microscope including transmission electron microscope (TEM) and scanning transmission electron microscope (STEM) both of which have ability to resolve the structures at atomic level. Some large clusters are studied in SEM as well. For gold nanoclusters, the first experimental observation of the structure can be tracked back to 1960s where gold clusters with diameter of about 30nm prepared by atomic vapor on gold single crystal were studied in TEM by Schwodebel et al. and the structure observed is decahedral [152]. In 1966 Ino et al. started to investigate gold clusters with different size in TEM. The clusters were prepared by atomic vapor deposition but with more control of the growth. Results showed that gold clusters with decahedral were observed at size of 40nm in diameter but icosahedral isomers were found as well with size between 10-40nm [153]. The structures of supported multi-twinned gold clusters on alkalihalide crystals were studied by Ino and Ogawa in 1967 suggesting that clusters of about 30nm prefer to be decahedral while 15nm clusters prefer icosahedral [154]. Big gold clusters up to 500nm deposited on mica substrate were also studied in early years by Sanders et al. showing decahedral structure [155]. Tsutomu et al. also studied the structure of gold clusters prepared by evaporation in TEM and the observation of decahedral for 15nm clusters and icosahedral for 13nm clusters was reported [156]. Between

1969 and 1972 the formation of multi-twinned gold clusters was investigated by Ino and Ogawa who found decahedral structure on clusters with 15nm and 20-40nm while icosahedral structure on 10 and 15-30nm clusters [157-158]. Wayman has studied structrure of gold clusters vaporized on graphite surface and found both decahedral and icosahedral structures on clusters about 40nm [159]. Relatively small gold clusters prepared by atomic vapor deposition were studied by Gillet et al. in 1977 showing decahedral structure on 15nm clusters and icosahedral structure on 8nm clusters [160]. Yacaman et al. reported the experimental study of gold clusters by vapor deposition in 1979 showing the decahedral structures of clusters between 12-40nm [161]. The first study of structures of clusters produced by cluster beam was reported in 1981 by Gillet et al. where Au, Pt and Pd clusters were produced in a flowing argon system and gold clusters presented decahedral and icosahedral for 6nm and 7nm clusters respectively [162]. In 1983 the Marks decahedral was first introduced by L. D. Marks observed on 10nm gold clusters [115]. Hofmeister et al. explored the inter structure of muli-twinned gold clusters on silver bromide film showing the gold clusters were decahedral [163]. Berriel-Valdos et al. found the equilibrium structure of 30nm gold clusters was icosahedral [164]. Ichihashi et al. studied the small gold nanoclusters around 2.5nm in TEM showing the decahedral structures [165]. Weiss et al. explored the structure of small gold nanoclusters between 2 and 6nm and also observed decahedral structures [166]. In Yacaman's work in early 1990s where small gold nanoclusters were produced by gas aggregation, decahedral structures were observed on 4nm gold clusters [167]. The structures of gold clusters prepared chemically were also studied where the size of the clusters was relatively larger. In 1973 Suito et al. observed decahedral

structure in 30nm colloidal gold clusters in TEM [168]. In 1990 Tholen et al. found gold clusters around 65nm synthesized chemically exhibiting decahedral structures [169]. Tanaka et al. explored gold nanoclsuters chemically synthesized in solution by electrodeposition with different electrode potentials showing that multi-twinned structures such as decahedral and icosahedral are more favored at low electrode potential and single crystalline or polycrystalline are preferred at high potential [170].

In recent researches published since 2000, Hofmeister et al. studied chemically synthesized gold nanoclusters containing two icosahedral in twin position in TEM combined with computer simulations [171]. In Oku and Hiraga's research published in 2000, Au nanoclusters prepared by chemical vapor and gas condensation with different size were studied in TEM, SEM and HREM and decahedral structures were observed on Au clusters of about 5nm [172]. The work done by Ugarte et al. in early 2000s has shown the statistical data of structures of gold nanoclusters prepared chemically where gold nanoclusters in range of 2-4nm were studied in HRTEM and XRD and fcc and decahedral structures were observed [173]. Also Koga and Sugawara have done statistical analysis on structures of gold nanoclusters with different size between 8 and 9 nm produced by cluster beam in HRTEM combined with multislice simulations where both decahedral and icosahedral isomers were identified [174]. Gold nanoclusters are used as catalyst and the structures of gold catalyst before and after reaction were studied by Hofmeister and Claus et al. using HRTEM where both decahedral and icosahedral were found on 5nm gold nanoclusters [175]. Buriak studied large gold nanoclusters of about 100nm synthesized chemically

in SEM which shows the large icosahedral structure [176]. Even larger gold clusters from 200nm to 5micrometers were studied by Xie et al. where most of them exhibit decahedral structures [177]. Chemically prepared small gold nanoclusters with narrow size distribution, around 2nm, were studied by Perez et al. showing that fcc and decahedral were dominant in Au clusters [178]. Using chemical method, Han et al. tried controlled synthesis process to produce pure or large proportion of gold clusters between 10 and 90nm with icosahedral structures [179]. In addition to Han's work, Song et al. have achieved the size control on not only just icosahedral but also decahedral and truncated tetrahedral gold clusters around 100nm prepared via chemical methods [180]. Moreover, Zhang et al. reported the ability to transform the structure of gold clusters from icosahedral to a truncated form [181]. Li et al. studied the size selected Au_{923} produced in magnetron sputtering gas condensation cluster beam source in STEM where the decahedral structure is observed and its 3D structure is revolved using quantitative HAADF image [4]. The effects of coalescence behavior on gold nanoclusters of around 3nm was studied by Geng et al. which promotes that formation of decahedral [182]. The coalescence of large cluster of about 10nm was studied by Tilley where real time TEM and kinetic monte carlo calculation were used to confirm decahedral is more favored in coalescence behavior [183]. Lee et al. reported the ability to control the structure of large gold clusters between 15-30nm in solution using 1,2-hexadecanediol to reduce the $AuCl_4^-$, which determined the crystallinity of the cluster [184]. Yacaman et al. studied the stability of decahedral in large clusters synthesized via rapid cooling mechanism [185].

More recently, the metastable structures of nanoclusters and their instabilities have been investigated, which dates back to late 1980s whe Iijima and Ichihashi already reported the structure fluctuation observed experimentally in small gold nanoclusters of around 2nm deposited on SiO_2 surface where their structures were found to flip back and forth randomly between multi-twinned structures and single crystal under the 120kV electron beam in TEM with electron beam dosage of $1.3x10^7 e/nm^2$. The structure transformation of size selected nanoclusters have also been explored by Palmer's group where the size selected nanoclusters were produced in the magnetron sputtering gas condensation cluster beam source with unique lateral time-of-flight mass selector and structures of nanoclusters were studied in the aberration corrected scanning transmission electron microscope [10]. The triangle structure of size selected Au_{20} and Chiral-type of size selected Au_{55} as well as their structural fluctuation were directly observed in the STEM [9,12]. The structure transformations of size selected Au_{923} from icosahedral to decahedral or fcc under 200keV electron beam were also confirmed in the experiments suggesting icosahedral is the least stable structure while decahedral or fcc is more likely to be the equilibrium state [10]. The structural transformation of larger size gold nanoclusters between 5 and 12nm was studied by Young et al. with fine controlled temperature and the phenomena that clusters transform into decahedral from different initial structures during the in-site heating in TEM was observed in real time [186]. Similar to the heating treatment, Yacaman et al. carried out rapid cooling on gold nanoclusters of 5-10.4 nm showing that decahedral transformed into icosahedral during the cooling process using variable temperature high resolution TEM (HRTEM) [185]. Nanoclusters annealed in gas phase or melt-freeze process have

been studied by Koga et al. in 2004 where the transformation from icosahedral to decahedral was observed on clusters with 3 to 14nm during the annealing whilst the transformation from decahedral to fcc was found during the melt-freeze treatment [187]. Although all nanoclusters are believed to be metastable, some structures are more metastable than the others. Early this year Wells and Palmer et al. demonstrated the metastability of size selected Au_{561}, Au_{742} and Au_{923} by monitoring the structure transformation under electron beam in real time using aberration corrected STEM [188]. The mechanism of structural transformation from icosahedral to decahedral of gold nanoclusters was discussed by Koga et al. suggesting it's caused by a cooperative slip dislocation of (111) planes inside the icosahedral structure. The icosahedral contains five fold axis surrounded by 10 distorted fcc tetrahedral in the middle, 5 in the top region and other 5 in the bottom region with the boundaries of (111) planes. The neighboring tetrahedral will merge into one new pyramid segment when those boundaries start to slip over the plane underlined and new (110) plane is exposed, which is believed to have lower energy barrier after this non-diffusive cooperative process [187].

2.5 Review of application of nanoclusters

The applications nanoclusters including metal, oxides, nitrides, carbon and semiconductors produced in gas phase using cluster beam deposition technique cover various area such as electronics, optics, magnetics, sensors [36], and specially on the catalysis and biotechnology fields, which are motivations to develop our new technology, the matrix assembly cluster source.

2.5.1 Catalysis

Applications of nanoclusters as catalysis have great potential due to their strong size dependent properties. For example, cluster beam deposition has been used to deposit size-selected nanoclusters on an inert surface to catalyze the chemical reaction as reported by Heiz et al [68]. In this work, the cluster beam was formed using laser ablation cluster source and mass selection was achieved using quadrupole mass filter. Clusters were then deposited on thin oxide film supported on metal single crystal. The cluster source in Heiz's group is also combined with various equipments such as FTIR, temperature desorption and electron spectroscopy to study the catalytic properties en-suit. The catalytic property of Ni clusters deposited on MgO thin film for CO oxidation is explored. Abbet has also investigated the catalytic properties of nanoclusters using similar system where size selected Pd, Au Ni and Si clusters are tested with the CO adsorption [190]. Catalytic properties as well as chemical properties of bimetallic nanoclusters such as Pd-Pt deposited on TiO_2 surface have been studied by Aizawa using the laser ablation cluster beam source and en-suit reaction system [191-202]. The photocatalytic properties of nanoclusters or thin film produced by cluster beam source equipped with UV light source irradiation has been intensively studied by Anpo et al, such as NO decomposition into N_2 and O_2 promoted by Ti/Si binary oxide thin film, oxidation of acetaldehyde by Pt nanoclusters deposited on TiO_2 thin film [193-195].

Palmer and co-workers have investigated the catalytic properties of bare size-selected metal nanoclusters by collaboration with Johnson Matthey [196-197].

Size selected nanoclusters are produced in the magnetron sputtering gas condensation cluster soruce and mass selection is achieved by the lateral time-of-flight mass selector. Size selected Au nanocluster containing 561, 923 and 2057 atoms have been tested to study the size dependent catalytic properties for CO oxidation. Pd_{923}, Pd_{2057} and Au_{923} and Au_{2057} have been tested for the 1-pentyne hydrogenation reaction. Moreover, the fates of the size selected clusters before and after chemical reactions have been studied statistically in the ac-STEM and the results show part of small clusters such as 561 and 923 are disintegrated during the reactions while large clusters are more stable which only slightly diffused and aggregated after chemical tests.

2.5.2 Biotechnological applications

An example of nanoclusters application in biological area is the bio-chips demonstrated by Palmer and co-workers where nanocluster deposited on the surface are used as anchor site to immobilize molecules [26,198-199]. The Au nanoclusters are produced in the magnetron sputtering cluster source and size of the clusters is selected by the lateral time-of-flight mass filter. Clusters are pinned into graphite surface with controlled high energy deposition method and the bonding between molecules and clusters are confirmed by the AFM imaging. This method would bring the single molecule optical studies into reality by using controlled well separated cluster deposition so that only one protein molecule is exposed in the microscope, which exhibits ultimate potential in increasing the sensitivity of biochips. The thin films assembled by nanoclusters produced in cluster beam source are also biocompatible as reported by Carbone et al that the

TiO_2 film assembled by TiO_x nanoclusters produced in supersonic beam is found to be supportive and adhesive for the normal growth of cancer cells [200]. The mechanism behind is the surface morphology of the nanoclusters assembled film exhibits nanoscale granularity enabling the surface functionalization with the molecules. The nanostructured titania film are proposed to be the most adequate substrate for cell arrays or medical microfabricated devices.

2.5.3 Other applications in electronics, optics and magnetics

Nanostructured materials especially semiconductors, are interest due to their electronic and optical properties. With the controlled deposition based on the cluster beam techniques, the properties of semiconductor nanoclusters such as the visible photoluminescence exhibited on nanocrystalline materials containing Ge or Si can be investigated as a function of cluster size or the size distribution or even the structures. Photoluminescence of silicon nanoclusters has been studied by Ehbrecht and co-workers combining a gas flow reactor and cluster beam deposition technique [201]. The silicon clusters are produced in the gas flow reactor using a CO laser to decompose the hydrogen from the SiH_4 and cluster beam is formed by supersonic expansion into the high vacuum. The photoluminescence, which is size dependent, is observed on the silicon clusters under ultraviolet radiation due to the quantum confinement effect. Voigt and co-workers have explored the electronic properties of silicon nanostructured film deposited of size selected silicon clusters with a coverage of about ~80% [202]. Results show the conductivity of the thin film is increased superliner as the function of film thickness, with exponent of 1.5. Ostraat and co-workers have

developed transistor based on silicon nanoclusters produced in gas phase showing compatible properties with industrial manufactured silicon [45]. The optic properties of metal clusters including both noble metal and alloys exhibiting size dependence has also been reported by Kreibig and co-workers using laser ablation source [203].

The magnetic properties of nanoclusters including Fe, Co as well as core shell clusters and binary clusters produced in gas phase have been summarized well by Binns and Sumiyama [204]. The effects of supporting substrates on their magnetic properties have been also investigated. Anther hot area of the application of nanoclusters is sensors [205-208]. Nanocluster based sensors have been studied by Kennedy and co-workers since ten years ago. In Kennedy's work, tin oxide nanoclusters (between 10 and 35nm) were produced by thermal evaporation in gas phase combined with in flight annealing afterwards. The integrated process demonstrated by Kennedy and co-workers has been widely used nowadays in manufacturing of nanocluster based sensors.

List of references

[1] Knight, W-D_, et al. "Electronic shell structure and abundances of sodium clusters." *Physical review letters* 52.24 (1984): 2141.

[2] Echt, O., K. Sattler, and E. Recknagel. "Magic numbers for sphere packings: experimental verification in free xenon clusters." *Physical Review Letters* 47.16 (1981): 1121.

[3] Martin, T. Patrick. "Shells of atoms." *Physics Reports* 273.4 (1996): 199-241.

[4] Li, Z. Y., et al. "Three-dimensional atomic-scale structure of size-selected gold nanoclusters." *Nature* 451.7174 (2008): 46-48.

[5] Pyykkö, Pekka. "Structural properties: Magic nanoclusters of gold." *Nature nanotechnology* 2.5 (2007): 273-274.

[6] Li, Jun, et al. "Au20: A tetrahedral cluster." *Science* 299.5608 (2003): 864-867.

[7] Kryachko, E. S., and Françoise Remacle. "The magic gold cluster Au20." *International Journal of Quantum Chemistry* 107.14 (2007): 2922-2934.

[8] Gruene, Philipp, et al. "Structures of neutral Au7, Au19, and Au20 clusters in the gas phase." *Science* 321.5889 (2008): 674-676.

[9] Wang, Z. W., and R. E. Palmer. "Direct atomic imaging and dynamical fluctuations of the tetrahedral Au 20 cluster." *Nanoscale* 4.16 (2012): 4947-4949.

[10] Wang, Z. W., and R. E. Palmer. "Determination of the ground-state atomic structures of size-selected Au nanoclusters by electron-beam-induced transformation." *Physical review letters* 108.24 (2012): 245502.

[11] Marks, L. D. "Experimental studies of small particle structures." *Reports on Progress in Physics* 57.6 (1994): 603.

[12] Jian, Nan, et al. "Hybrid atomic structure of the Schmid cluster Au 55 (PPh 3) 12 Cl 6 resolved by aberration-corrected STEM." *Nanoscale* 7.3 (2015): 885-888.

[13] Valden, M., X. Lai, and Dz W. Goodman. "Onset of catalytic activity of gold clusters on titania with the appearance of nonmetallic properties." *Science* 281.5383 (1998): 1647-1650.

[14] Reetz, Manfred T., et al. "Visualization of surfactants on nanostructured palladium clusters by a combination of STM and high-resolution TEM." *Science* 267.5196 (1995): 367.

[15] Morales, Alfredo M., and Charles M. Lieber. "A laser ablation method for the synthesis of crystalline semiconductor nanowires." *Science* 279.5348 (1998): 208-211.

[16] Billas, Isabelle ML, A. Chatelain, and Walt A. de Heer. "Magnetism from the atom to the bulk in iron, cobalt, and nickel clusters." *Science* 265.5179 (1994): 1682-1684.

[17] Rossi, Giulia, et al. "Magic polyicosahedral core-shell clusters." *Physical review letters* 93.10 (2004): 105503.

[18] Lauritsen, Jeppe V., et al. "Size-dependent structure of MoS2 nanocrystals." *Nature nanotechnology* 2.1 (2007): 53-58.

[19] Häkkinen, Hannu, et al. "Structural, electronic, and impurity-doping effects in nanoscale chemistry: supported gold nanoclusters." *Angewandte Chemie International Edition* 42.11 (2003): 1297-1300.

[20] Daniel, Marie-Christine, and Didier Astruc. "Gold nanoparticles: assembly, supramolecular chemistry, quantum-size-related properties, and applications toward biology, catalysis, and nanotechnology." *Chemical reviews* 104.1 (2004): 293-346.

[21] Xu, Z., et al. "Size-dependent catalytic activity of supported metal clusters." (1994): 346-348.

[22] Heiz, U., et al. "Catalytic oxidation of carbon monoxide on monodispersed platinum clusters: each atom counts." *Journal of the American Chemical Society* 121.13 (1999): 3214-3217.

[23] Lee, Sungsik, et al. "CO oxidation on Au n/TiO2 catalysts produced by size-selected cluster deposition." *Journal of the American Chemical Society* 126.18 (2004): 5682-5683.

[24] Vajda, Stefan, et al. "Subnanometre platinum clusters as highly active and selective catalysts for the oxidative dehydrogenation of propane." *Nature materials* 8.3 (2009): 213-216.

[25] Tada, Tetsuya, et al. "Formation of 10 nm Si structures using size-selected metal clusters." *Journal of Physics D: Applied Physics* 31.7 (1998): L21.

[26] Palmer, Richard E., and Carl Leung. "Immobilisation of proteins by atomic clusters on surfaces." *TRENDS in Biotechnology* 25.2 (2007): 48-55.

[27] Leung, Carl, et al. "Immobilization of Protein Molecules by Size-Selected Metal Clusters on Surfaces." *Advanced Materials* 16.3 (2004): 223-226.

[28] Wenseleers, Wim, et al. "Five orders-of-magnitude enhancement of two-photon absorption for dyes on silver nanoparticle fractal clusters." *The Journal of Physical Chemistry B* 106.27 (2002): 6853-6863.

[29] Stenzel, O., et al. "Enhancement of the photovoltaic conversion efficiency of copper phthalocyanine thin film devices by incorporation of metal clusters." *Solar energy materials and solar cells* 37.3 (1995): 337-348.

[30] Rand, Barry P., Peter Peumans, and Stephen R. Forrest. "Long-range absorption enhancement in organic tandem thin-film solar cells containing silver nanoclusters." *Journal of Applied Physics* 96.12 (2004): 7519-7526.

[31] Zhao, Linlin, Lasse Jensen, and George C. Schatz. "Pyridine-Ag20 cluster: a model system for studying surface-enhanced Raman scattering." *Journal of the American chemical society* 128.9 (2006): 2911-2919.

[32] Nie, Shuming, and Steven R. Emory. "Probing single molecules and single nanoparticles by surface-enhanced Raman scattering." *science* 275.5303 (1997): 1102-1106.

[33] Dietz, Thomas G., et al. "Laser production of supersonic metal cluster beams." *The Journal of Chemical Physics* 74.11 (1981): 6511-6512.

[34] De Heer, Walt A. "The physics of simple metal clusters: experimental aspects and simple models." *Reviews of Modern Physics* 65.3 (1993): 611.

[35] Stark, Wendelin J., and Sotiris E. Pratsinis. "Aerosol flame reactors for manufacture of nanoparticles." *Powder Technology* 126.2 (2002): 103-108.

[36] Wegner, K., et al. "Cluster beam deposition: a tool for nanoscale science and technology." *Journal of Physics D: Applied Physics* 39.22 (2006): R439.

[37] Lockwood, David J. "Nanostructure Science and Technology."

[38] Wegner, Karsten, and Sotiris E. Pratsinis. "Scale-up of nanoparticle synthesis in diffusion flame reactors." *Chemical Engineering Science* 58.20 (2003): 4581-4589.

[39] Kammler, Hendrik K., Lutz Mädler, and Sotiris E. Pratsinis. "Flame synthesis of nanoparticles." *Chemical engineering & technology* 24.6 (2001): 583-596.

[40] Singh, Yogendra, et al. "Approaches to increasing yield in evaporation/condensation nanoparticle generation." *Journal of Aerosol Science* 33.9 (2002): 1309-1325.

[41] Wegner, Karsten, and Sotiris E. Pratsinis. "Nozzle-quenching process for controlled flame synthesis of titania nanoparticles." *AIChE Journal* 49.7 (2003): 1667-1675.

[42] Nakaso, Koichi, et al. "Evaluation of the change in the morphology of gold nanoparticles during sintering." *Journal of Aerosol Science* 33.7 (2002): 1061-1074.

[43] Nanda, K. K., et al. "Band-gap tuning of PbS nanoparticles by in-flight sintering of size classified aerosols." *Journal of applied physics* 91.4 (2002): 2315-2321.

[44] Karlsson, Martin NA, et al. "Size-and composition-controlled Au–Ga aerosol nanoparticles." *Aerosol science and technology* 38.9 (2004): 948-954.

[45] Ostraat, Michele L., et al. "Ultraclean two-stage aerosol reactor for production of oxide-passivated silicon nanoparticles for novel memory devices." *Journal of The Electrochemical Society* 148.5 (2001): G265-G270.

[46] Milani, Paolo, and Salvatore Iannotta. *Cluster beam synthesis of nanostructured materials*. Springer Science & Business Media, 2012.

[47] Milani, P., et al. "Cluster beam synthesis of nanostructured thin films." *Journal of Vacuum Science & Technology A* 19.4 (2001): 2025-2033.

[48] Mazza, T., et al. "Libraries of cluster-assembled titania films for chemical sensing." *Applied Physics Letters* 87.10 (2005): 103108.

[49] Granqvist, C. G., and R. A. Buhrman. "Ultrafine metal particles." *Journal of Applied Physics* 47.5 (1976): 2200-2219.

[50] Haberland, Hellmut, et al. "Thin films from energetic cluster impact: a feasibility study." *Journal of Vacuum Science & Technology A* 10.5 (1992): 3266-3271.

[51] Hihara, Takehiko, and Kenji Sumiyama. "Formation and size control of a Ni cluster by plasma gas condensation." *Journal of applied physics* 84.9 (1998): 5270-5276.

[52] Yamamuro, S., Kenji Sumiyama, and K. Suzuki. "Monodispersed Cr cluster formation by plasma-gas-condensation." *Journal of applied physics* 85.1 (1999): 483-489.

[53] Sumiyama, Kenji, et al. "Structure and magnetic properties of Co/CoO and Co/Si core–shell cluster assemblies prepared via gas-phase." *Science and Technology of Advanced Materials* 6.1 (2005): 18-26.

[54] Goldby, Ian Michael. *Dynamics of molecules and clusters at surfaces*. Diss. University of Cambridge, 1996.

[55] Uyeda, Ryozi. "Studies of ultrafine particles in Japan: crystallography. Methods of preparation and technological applications." *Progress in Materials Science* 35.1 (1991): 1-96.

[56] Hihara, Takehiko, and Kenji Sumiyama. "Formation and size control of a Ni cluster by plasma gas condensation." *Journal of applied physics* 84.9 (1998): 5270-5276.

[57] Lehtinen, Kari EJ, and Michael R. Zachariah. "Self-preserving theory for the volume distribution of particles undergoing Brownian coagulation." *Journal of Colloid and Interface Science* 242.2 (2001): 314-318.

[58] Gatz, P., and O. F. Hagena. "Cluster beams for metallization of microstructured surfaces." *Applied surface science* 91.1 (1995): 169-174.

[59] Ross, K. J., and B. Sonntag. "High temperature metal atom beam sources." *Review of scientific instruments* 66.9 (1995): 4409-4433.

[60] Ross, K. J., and B. Sonntag. "High temperature metal atom beam sources." *Review of scientific instruments* 66.9 (1995): 4409-4433.

[61] Bewig, L., et al. "Seeded supersonic alkali cluster beam source with refilling system." *Review of scientific instruments* 63.8 (1992): 3936-3938.

[62] Binns, C. "Nanoclusters deposited on surfaces." *Surface science reports* 44.1 (2001): 1-49.

[63] Dietz, Thomas G., et al. "Laser production of supersonic metal cluster beams." *The Journal of Chemical Physics* 74.11 (1981): 6511-6512.

[64] Duncan, Michael A. "Invited Review Article: Laser vaporization cluster sourcesa)." *Review of Scientific Instruments* 83.4 (2012): 041101.

[65] Maruyama, Shigeo, Lila R. Anderson, and Richard E. Smalley. "Direct injection supersonic cluster beam source for FT-ICR studies of clusters." *Review of scientific instruments* 61.12 (1990): 3686-3693.

[66] Milani, Paolo. "Improved pulsed laser vaporization source for production of intense beams of neutral and ionized clusters." *Review of scientific instruments* 61.7 (1990): 1835-1838.

[67] Geusic, M. E., et al. "Surface reactions of metal clusters I: The fast flow cluster reactor." *Review of Scientific Instruments* 56.11 (1985): 2123-2130.

[68] Heiz, U., et al. "Chemical reactivity of size-selected supported clusters: An experimental setup." *Review of scientific instruments* 68.5 (1997): 1986-1994.

[69] Woenckhaus, J., and J. A. Becker. "A fast pressure monitor for pulsed laser vaporization cluster sources." *Review of scientific instruments* 65.6 (1994): 2019-2022.

[70] Bansmann, Joachim, et al. "Magnetic and structural properties of isolated and assembled clusters." *Surface Science Reports* 56.6 (2005): 189-275.

[71] Haberland, H., M. Karrais, and M. Mall. "A new type of cluster and cluster ion source." *Zeitschrift für Physik D Atoms, Molecules and Clusters* 20.1 (1991): 413-415.

[72] Raizer, Yuri P., and John E. Allen. *Gas discharge physics*. Vol. 2. Berlin: Springer, 1997.

[73] Haberland, Hellmut, et al. "Thin films from energetic cluster impact: a feasibility study." *Journal of Vacuum Science & Technology A* 10.5 (1992): 3266-3271.

[74] Pratontep, S., et al. "Size-selected cluster beam source based on radio frequency magnetron plasma sputtering and gas condensation." *Review of scientific instruments* 76.4 (2005): 045103.

[75] Smith, Roger. *Atomic and ion collisions in solids and at surfaces: theory, simulation and applications*. Cambridge University Press, 2005.

[76] Olynick, D. L., J. M. Gibson, and R. S. Averback. "Impurity-suppressed sintering in copper nanophase materials." *Philosophical Magazine A* 77.5 (1998): 1205-1221.

[77] Soler, J. M., et al. "Microcluster growth: transition from successive monomer addition to coagulation." *Physical Review Letters* 49.25 (1982): 1857.

[78] Hihara, Takehiko, and Kenji Sumiyama. "Formation and size control of a Ni cluster by plasma gas condensation." *Journal of applied physics* 84.9 (1998): 5270-5276.

[79] Barborini, E., P. Piseri, and P. Milani. "A pulsed microplasma source of high intensity supersonic carbon cluster beams." *Journal of Physics D: Applied Physics* 32.21 (1999): L105.

[80] Tafreshi, H. Vahedi, et al. "The role of gas dynamics in operation conditions of a pulsed microplasma cluster source for nanostructured thin films deposition." *Journal of nanoscience and nanotechnology* 6.4 (2006): 1140-1149.

[81] Bongiorno, G., et al. "Nanocrystalline metal/carbon composites produced by supersonic cluster beam deposition." *Journal of nanoscience and nanotechnology* 5.7 (2005): 1072-1080.

[82] Ganteför, Gerd, et al. "Pure metal and metal-doped rare-gas clusters grown in a pulsed ARC cluster ion source." *Chemical Physics Letters* 165.4 (1990): 293-296.

[83] Ganteför, Gerd, et al. "Pure metal and metal-doped rare-gas clusters grown in a pulsed ARC cluster ion source." *Chemical Physics Letters* 165.4 (1990): 293-296.

[84] Siekmann, H. R., et al. "VUV-photoelectron spectroscopy on lead clusters deposited from the pulsed arc cluster ion source (PACIS)." *Zeitschrift für Physik B Condensed Matter* 90.2 (1993): 201-206.

[85] Cha, Chia-Yen, Gerd Ganteför, and Wolfgang Eberhardt. "New experimental setup for photoelectron spectroscopy on cluster anions." *Review of scientific instruments* 63.12 (1992): 5661-5666.

[86] Mohanty, U. S. "Electrodeposition: a versatile and inexpensive tool for the synthesis of nanoparticles, nanorods, nanowires, and nanoclusters of metals." *Journal of applied electrochemistry* 41.3 (2011): 257-270.

[87] Niu, Wenxin, and Guobao Xu. "Crystallographic control of noble metal nanocrystals." *Nano Today* 6.3 (2011): 265-285.

[88] Moriarty, Philip. "Nanostructured materials." *Reports on Progress in Physics* 64.3 (2001): 297.

[89] Faraday, Michael. "The Bakerian lecture: experimental relations of gold (and other metals) to light." *Philosophical Transactions of the Royal Society of London* 147 (1857): 145-181.

[90] Xia, Younan, et al. "Shape-Controlled Synthesis of Metal Nanocrystals: Simple Chemistry Meets Complex Physics?." *Angewandte Chemie International Edition* 48.1 (2009): 60-103.

[91] Fennell, John, et al. "A selective blocking method to control the overgrowth of Pt on Au nanorods." *Journal of the American Chemical Society* 135.17 (2013): 6554-6561.

[92] URL http://www.nobelprize.org/nobel_prizes/physics/laureates

[93] Williams, David B., and C. Barry Carter. The transmission electron microscope. Springer Us, 1996.

[94] Nellist, P. D., and S. J. Pennycook. "Incoherent imaging using dynamically scattered coherent electrons." Ultramicroscope 78.1 (1999): 111-124.

[95] Scherzer, O_. "über einige Fehler von Elektronenlinsen." Zeitschrift für Physik 101.9-10 (1936): 593-603.

[96] Scherzer, O. "Spharische und chromatische korrektur von elektronen-linsen." Optik 2 (1947): 114-132.

[97] Lupini, Andrew R., et al. "Characterizing the two-and three-dimensional resolution of an improved aberration-corrected STEM." Microscope and Microanalysis 15.05 (2009): 441-453.

[98] Haider, Maximilian, et al. "Electron microscope image enhanced." Nature 392 (1998): 768-769.

[99] Borisevich, Albina Y., Andrew R. Lupini, and Stephen J. Pennycook. "Depth sectioning with the aberration-corrected scanning transmission electron microscope." Proceedings of the National Academy of Sciences of the United States of America 103.9 (2006): 3044-3048.

[100] Haider, M., S. Uhlemann, and J. Zach. "Upper limits for the residual aberrations of a high-resolution aberration-corrected STEM." Ultramicroscope 81.3 (2000): 163-175.

[101] Rose, H. H. "Optics of high-performance electron microscopes." Science and Technology of Advanced Materials 9.1 (2008): 014107.

[102] Haider, Max, et al. "A spherical-aberration-corrected 200kV transmission electron microscope." Ultramicroscope 75.1 (1998): 53-60.

[103] Klenov, Dmitri O., and Susanne Stemmer. "Contributions to the contrast in experimental high-angle annular dark-field images." Ultramicroscope 106.10 (2006): 889-901.

[104] Wang, Z. W., et al. "Quantitative Z-contrast imaging in the scanning transmission electron microscope with size-selected clusters." Physical Review B 84.7 (2011): 073408.

[105] Nellist, P. D., and S. J. Pennycook. "The Principles and Interpretations of Annular Dark-Field Z-Contrast Imaging." Advances in Imaging and Electron Physics 113 (2000): 148-204.

[106] Jesson, D. E., and S. J. Pennycook. "Incoherent imaging of crystals using thermally scattered electrons." Proceedings of the Royal Society of London A:

Mathematical, Physical and Engineering Sciences. Vol. 449. No. 1936. The Royal Society, 1995.

[107] Mackay, A. L. "A dense non-crystallographic packing of equal spheres." *Acta Crystallographica* 15.9 (1962): 916-918.

[108] Echt, O., K. Sattler, and E. Recknagel. "Magic numbers for sphere packings: experimental verification in free xenon clusters." *Physical Review Letters* 47.16 (1981): 1121.

[109] Honeycutt, J. Dana, and Hans C. Andersen. "Molecular dynamics study of melting and freezing of small Lennard-Jones clusters." *Journal of Physical Chemistry* 91.19 (1987): 4950-4963.

[110] Martin, T. P., et al. "Shell structure of clusters." *The Journal of Physical Chemistry* 95.17 (1991): 6421-6429.

[111] Martin, T. Patrick. "Shells of atoms." *Physics Reports* 273.4 (1996): 199-241.

[112] Ino, Shozo. "Stability of multiply-twinned particles." *Journal of the Physical Society of Japan* 27.4 (1969): 941-953.

[113] Raoult, B., et al. "Comparison between icosahedral, decahedral and crystalline Lennard-Jones models containing 500 to 6000 atoms." *Philosophical Magazine B* 60.6 (1989): 881-906.

[114] Marks, L. D. "Surface structure and energetics of multiply twinned particles." *Philosophical Magazine A* 49.1 (1984): 81-93.

[115] Marks, L. D. "Modified Wulff constructions for twinned particles." *Journal of Crystal Growth* 61.3 (1983): 556-566.

[116] Baletto, Francesca, and Riccardo Ferrando. "Structural properties of nanoclusters: Energetic, thermodynamic, and kinetic effects." *Reviews of modern physics* 77.1 (2005): 371.

[117] Mackay, A. L. "A dense non-crystallographic packing of equal spheres." *Acta Crystallographica* 15.9 (1962): 916-918.

[118] Kuo, K. H. "Mackay, anti-Mackay, double-Mackay, pseudo-Mackay, and related icosahedral shell clusters." *Structural Chemistry* 13.3-4 (2002): 221-230.

[119] Mottet, C., et al. "Modeling free and supported metallic nanoclusters: structure and dynamics." *Phase Transitions* 77.1-2 (2004): 101-113.

[120] Nam, H-S., et al. "Formation of an icosahedral structure during the freezing of gold nanoclusters: surface-induced mechanism." *Physical review letters* 89.27 (2002): 275502.

[121] Chushak, Yaroslav G., and Lawrence S. Bartell. "Melting and freezing of gold nanoclusters." *The Journal of Physical Chemistry B* 105.47 (2001): 11605-11614.

[122] Cleveland, Charles L., W. D. Luedtke, and Uzi Landman. "Melting of gold clusters: Icosahedral precursors." *Physical review letters* 81.10 (1998): 2036.

[123] Baletto, F., C. Mottet, and R. Ferrando. "Microscopic mechanisms of the growth of metastable silver icosahedra." *Physical Review B* 63.15 (2001): 155408.

[124] Barnard, A. S., et al. "Ideality versus reality: Emergence of the Chui icosahedron." *The Journal of Physical Chemistry C* 112.38 (2008): 14848-14852.

[125] Chui, Yu Hang, et al. "Topological characterization of crystallization of gold nanoclusters." *The Journal of chemical physics* 125.11 (2006): 114703.

[126] Chui, Yu Hang, et al. "Molecular dynamics investigation of the structural and thermodynamic properties of gold nanoclusters of different morphologies." *Physical Review B* 75.3 (2007): 033404.

[127] Cleveland, Charles L., and Uzi Landman. "The energetics and structure of nickel clusters: size dependence." *The Journal of chemical physics* 94.11 (1991): 7376-7396.

[128] Ascencio, J. A., et al. "Structure determination of small particles by HREM imaging: theory and experiment." *Surface Science* 396.1 (1998): 349-368.

[129] Baletto, F., et al. "Crossover among structural motifs in transition and noble-metal clusters." *The Journal of chemical physics* 116.9 (2002): 3856-3863.

[130] Germer Jr, Henry A. "Solvent interaction within the Hartree-Fock SCF molecular orbital formalism." *Theoretica chimica acta* 34.2 (1974): 145-155.

[131] Ho, Kai-Ming, et al. "Structures of medium-sized silicon clusters." *Nature* 392.6676 (1998): 582-585.

[132] Barreteau, C., et al. "spd tight-binding model of magnetism in transition metals: Application to Rh and Pd clusters and slabs." *Physical Review B* 61.11 (2000): 7781.

[133] Ferrando, Riccardo, Julius Jellinek, and Roy L. Johnston. "Nanoalloys: from theory to applications of alloy clusters and nanoparticles." *Chemical reviews* 108.3 (2008): 845-910.

[134] Grochola, Gregory, Salvy P. Russo, and Ian K. Snook. "On morphologies of gold nanoparticles grown from molecular dynamics simulation." *The Journal of chemical physics* 126.16 (2007): 164707.

[135] Feigl, Christopher, et al. "A theoretical study of size and temperature dependent morphology transformations in gold nanoparticles." *Chemical Physics Letters* 474.1 (2009): 115-118.

[136] Desgranges, Caroline, and Jerome Delhommelle. "Molecular simulation of the nucleation and growth of gold nanoparticles." *The Journal of Physical Chemistry C* 113.9 (2009): 3607-3611.

[137] Barnard, Amanda S. "Direct comparison of kinetic and thermodynamic influences on gold nanomorphology." *Accounts of chemical research* 45.10 (2012): 1688-1697.

[138] Baletto, F., C. Mottet, and R. Ferrando. "Reentrant morphology transition in the growth of free silver nanoclusters." *Physical review letters* 84.24 (2000): 5544.

[139] Grochola, G., et al. "Exploring the effects of different immersion environments on the growth of gold nanostructures." *Molecular Simulation* 32.15 (2006): 1255-1260.

[140] Barnard, Amanda S., et al. "Nanogold: a quantitative phase map." *ACS nano* 3.6 (2009): 1431-1436.

[141] Kuo, Chin-Lung, and Paulette Clancy. "Melting and freezing characteristics and structural properties of supported and unsupported gold nanoclusters." *The Journal of Physical Chemistry B* 109.28 (2005): 13743-13754.

[142] Wang, Yanting, S. Teitel, and Christoph Dellago. "Melting of icosahedral gold nanoclusters from molecular dynamics simulations." *The Journal of chemical physics* 122.21 (2005): 214722.

[143] Chen, Fuyi, Z. Y. Li, and Roy L. Johnston. "Surface reconstruction precursor to melting in Au309 clusters." *AIP Advances* 1.3 (2011): 032105.

[144] Doye, J. P. K., and D. J. Wales. "Thermally-induced surface reconstructions of Mackay icosahedra." *Zeitschrift für Physik D Atoms, Molecules and Clusters* 40.1 (1997): 466-468.

[145] Ercolessi, Furio, Wanda Andreoni, and Erio Tosatti. "Melting of small gold particles: Mechanism and size effects." *Physical Review Letters* 66.7 (1991): 911.

[146] Schebarchov, D., and S. C. Hendy. "Thermal instability of decahedral structures in platinum nanoparticles." *The European Physical Journal D* 43.1-3 (2007): 11-14.

[147] Schebarchov, D., S. C. Hendy, and W. Polak. "Molecular dynamics study of the melting of a supported 887-atom Pd decahedron." *Journal of Physics: Condensed Matter* 21.14 (2009): 144204.

[148] Chushak, Y., and Lawrence S. Bartell. "Molecular dynamics simulations of the freezing of gold nanoparticles." *The European Physical Journal D-Atomic, Molecular, Optical and Plasma Physics* 16.1 (2001): 43-46.

[149] Opletal, G., et al. "Elucidation of surface driven crystallization of icosahedral clusters." *Chemical Physics Letters* 482.4 (2009): 281-286.

[150] Delogu, F. "A numerical study of the freezing behavior of an unsupported nanometer-sized Au droplet." *Nanotechnology* 18.48 (2007): 485710.

[151] Chui, Yu Hang, Ian K. Snook, and Salvy P. Russo. "Visualization and analysis of structural ordering during crystallization of a gold nanoparticle." *Physical Review B* 76.19 (2007): 195427.

[152] Schwoebel, R. L. "Condensation of gold on gold single crystals." *Surface Science* 2 (1964): 356-366.

[153] Ino, Shozo. "Epitaxial growth of metals on rocksalt faces cleaved in vacuum. II. Orientation and structure of gold particles formed in ultrahigh vacuum." *Journal of the Physical Society of Japan* 21.2 (1966): 346-362.

[154] Ino, Shozo, and Shiro Ogawa. "Multiply twinned particles at earlier stages of gold film formation on alkalihalide crystals." *Journal of the Physical Society of Japan* 22.6 (1967): 1365-1374.

[155] Allpress, J. G., and J. V. Sanders. "The structure and orientation of crystals in deposits of metals on mica." *Surface Science* 7.1 (1967): 1-25.

[156] Komoda, Tsutomu. "Study on the structure of evaporated gold particles by means of a high resolution electron microscope." *Japanese Journal of Applied Physics* 7.1 (1968): 27.

[157] Ogawa, Shiro, and Shozo Ino. "Formation of Multiply-Twinned Particles in the Nucleation Stage of Film Growth." *Journal of Vacuum Science & Technology* 6.4 (1969): 527-534.

[158] Ogawa, Shiro, and Shozo Ino. "Formation of multiply-twinned particles on alkali halide crystals by vacuum evaporation and their structures." *Journal of Crystal Growth* 13 (1972): 48-56.

[159] Wayman, C. M., and T. P. Darby. "Nucleation and growth of gold films on graphite: II. The effect of substrate temperature." *Journal of Crystal Growth* 28.1 (1975): 53-67.

[160] Gillet, M. "Structure of small metallic particles." *Surface Science* 67.1 (1977): 139-157.

[161] Heinemann, K., et al. "The structure of small, vapor-deposited particles: I. Experimental study of single crystals and particles with pentagonal profiles." *Journal of Crystal Growth* 47.2 (1979): 177-186.

[162] Renou, A., and M. Gillet. "Growth of Au, Pt and Pd particles in a flowing argon system: Observations of decahedral and icosahedral structures." *Surface Science* 106.1 (1981): 27-34.

[163] Hofmeister, H. "Habit and internal structure of multiply twinned gold particles on silver bromide films." *Thin Solid Films* 116.1 (1984): 151-162.

[164] Pérez-Ramírez, J. G., et al. "On the equilibrium shape of multiple-twinned particles." *Superlattices and Microstructures* 1.6 (1985): 485-487.

[165] Iijima, Sumio, and Toshinari Ichihashi. "Structural instability of ultrafine particles of metals." *Physical review letters* 56.6 (1986): 616.

[166] Gao, Pei-Yu, et al. "The structure of small penta-twinned gold particles." *Zeitschrift für Physik D Atoms, Molecules and Clusters* 12.1-4 (1989): 119-121.

[167] Jose-Yacaman, M., et al. "Decagonal and hexagonal structures in small gold particles." *Surface Science* 237.1 (1990): 248-256.

[168] Uyeda, Natsu, Misao Nishino, and Eiji Suito. "Nucleus interaction and fine structures of colloidal gold particles." *Journal of Colloid and Interface Science* 43.2 (1973): 264-276.

[169] Thölén, A. R. "Electron microscope investigation of small particles." *Phase Transitions: A Multinational Journal* 24.1 (1990): 375-406.

[170] Lu, Da-ling, et al. "The shape and structure of gold particles grown at different electrode potentials." *Surface science* 325.1 (1995): L397-L405.

[171] Nepijko, Sergej A., et al. "Multiply twinned particles beyond the icosahedron." *Journal of Crystal Growth* 213.1 (2000): 129-134.

[172] Oku, Takeo, and Kenji Hiraga. "Atomic structures and stability of hexagonal BN, diamond and Au multiply-twinned nanoparticles with five-fold symmetry." *Diamond and related materials* 10.3 (2001): 1398-1403.

[173] Zanchet, D., B. D. Hall, and D. Ugarte. "Structure population in thiol-passivated gold nanoparticles." *The Journal of Physical Chemistry B* 104.47 (2000): 11013-11018.

[174] Koga, K., and K-I. Sugawara. "Population statistics of gold nanoparticle morphologies: direct determination by HREM observations." *Surface science* 529.1 (2003): 23-35.

[175] Mohr, Christian, Herbert Hofmeister, and Peter Claus. "The influence of real structure of gold catalysts in the partial hydrogenation of acrolein." *Journal of Catalysis* 213.1 (2003): 86-94.

[176] Hormozi Nezhad, Mohammad R., et al. "Synthesis and patterning of gold nanostructures on InP and GaAs via galvanic displacement." *Small* 1.11 (2005): 1076-1081.

[177] Jiang, Peng, et al. "Poly (vinyl pyrrolidone)-capped five-fold twinned gold particles with sizes from nanometres to micrometres." *Nanotechnology* 17.14 (2006): 3533.

[178] Esparza, R., et al. "Structural analysis and shape-dependent catalytic activity of Au, Pt and Au/Pt nanoparticles." *Matéria (Rio de Janeiro)* 13.4 (2008): 579-586.

[179] Kwon, Kihyun, et al. "Controlled synthesis of icosahedral gold nanoparticles and their surface-enhanced Raman scattering property." *The Journal of Physical Chemistry C* 111.3 (2007): 1161-1165.

[180] Seo, Daeha, et al. "Shape adjustment between multiply twinned and single-crystalline polyhedral gold nanocrystals: decahedra, icosahedra, and truncated tetrahedra." *The Journal of Physical Chemistry C* 112.7 (2008): 2469-2475.

[181] Xu, Jun, et al. "Hydrothermal syntheses of gold nanocrystals: from icosahedral to its truncated form." *Advanced Functional Materials* 18.2 (2008): 277-284.

[182] Wang, Y. Q., W. S. Liang, and C. Y. Geng. "Coalescence behavior of gold nanoparticles." *Nanoscale research letters* 4.7 (2009): 684-688.

[183] Lim, Teck H., et al. "Real-time TEM and kinetic Monte Carlo studies of the coalescence of decahedral gold nanoparticles." *ACS nano* 3.11 (2009): 3809-3813.

[184] Zhang, Qingbo, et al. "Tuning the crystallinity of Au nanoparticles." *Small* 6.4 (2010): 523-527.

[185] Casillas, Gilberto, J. Jesús Velázquez-Salazar, and Miguel Jose-Yacaman. "A New Mechanism of Stabilization of Large Decahedral Nanoparticles." *The Journal of Physical Chemistry C* 116.15 (2012): 8844-8848.

[186] Young, N. P., et al. "Transformations of gold nanoparticles investigated using variable temperature high-resolution transmission electron microscope." *Ultramicroscope* 110.5 (2010): 506-516.

[187] Koga, Kenji, Tamio Ikeshoji, and Ko-ichi Sugawara. "Size-and temperature-dependent structural transitions in gold nanoparticles." *Physical review letters* 92.11 (2004): 115507.

[188] Wells, Dawn M., et al. "Metastability of the atomic structures of size-selected gold nanoparticles." *Nanoscale* 7.15 (2015): 6498-6503.

[189] Nalwa, Hari Singh. *Encyclopedia of nanoscience and nanotechnology*. CRC Press, 2004.

[190] Abbet, Stéphane, et al. "Synthesis of monodispersed model catalysts using softlanding cluster deposition." *Pure and Applied Chemistry* 74.9 (2002): 1527-1535.

[191] Aires, FJ Cadete Santos, et al. "Scanning tunneling microscope study of model catalysts obtained by cluster beam deposition of palladium onto highly oriented pyrolitic graphite." *Journal of Vacuum Science & Technology B* 12.3 (1994): 1776-1779.

[192] Rousset, J. L., et al. "Characterization and reactivity of Pd–Pt bimetallic supported catalysts obtained by laser vaporization of bulk alloy." *Applied surface science* 164.1 (2000): 163-168.

[193] Takeuchi, Masato, et al. "Preparation of titanium-silicon binary oxide thin film photocatalysts by an ionized cluster beam deposition method. Their photocatalytic activity and photoinduced super-hydrophilicity." *The Journal of Physical Chemistry B* 107.51 (2003): 14278-14282.

[194] Takeuchi, Masato, et al. "Effect of Pt loading on the photocatalytic reactivity of titanium oxide thin films prepared by ion engineering techniques." *Research on chemical intermediates* 29.6 (2003): 619-629.

[195] Zhou, Jinkai, et al. "Photocatalytic decomposition of formic acid under visible light irradiation over V-ion-implanted TiO2 thin film photocatalysts prepared on quartz substrate by ionized cluster beam (ICB) deposition method." *Catalysis letters* 106.1-2 (2006): 67-70.

[196] Hu, Kuo-Juei, et al. "The effects of 1-pentyne hydrogenation on the atomic structures of size-selected Au N and Pd N (N= 923 and 2057) nanoclusters." *Physical Chemistry Chemical Physics* (2014).

[197] Malola, Sami, et al. "Au40 (SR) 24 cluster as a chiral dimer of 8-electron superatoms: Structure and optical properties." *Journal of the American Chemical Society* 134.48 (2012): 19560-19563.

[198] Collins, J. A., et al. "Clusters for biology: immobilization of proteins by size-selected metal clusters." *Applied surface science* 226.1 (2004): 197-208.

[199] Palmer, R. E., S. Pratontep, and H-G. Boyen. "Nanostructured surfaces from size-selected clusters." *Nature Materials* 2.7 (2003): 443-448.

[200] Carbone, Roberta, et al. "Biocompatibility of cluster-assembled nanostructured TiO 2 with primary and cancer cells." *Biomaterials* 27.17 (2006): 3221-3229.

[201] Ehbrecht, M., et al. "Photoluminescence and resonant Raman spectra of silicon films produced by size-selected cluster beam deposition." *Physical Review B* 56.11 (1997): 6958.

[202] Voigt, F., et al. "Porous thin films grown from size-selected silicon nanocrystals." *Materials Science and Engineering: C* 25.5 (2005): 584-589.

[203] Kreibig, Uwe, and Michael Vollmer. "Optical properties of metal clusters." (1995).

[204] Binns, C., et al. "The behaviour of nanostructured magnetic materials produced by depositing gas-phase nanoparticles." *Journal of Physics D: Applied Physics* 38.22 (2005): R357.

[205] Qiu, Jiao-Ming, et al. "Nanocluster deposition for high density magnetic recording tape media." *Journal of applied physics* 97.10 (2005): 10P704.

[206] Kennedy, M. K., et al. "Tailored nanoparticle films from monosized tin oxide nanocrystals: particle synthesis, film formation, and size-dependent gas-sensing properties." *Journal of Applied Physics* 93.1 (2003): 551-560.

[207] Mädler, L., et al. "Direct formation of highly porous gas-sensing films by in situ thermophoretic deposition of flame-made Pt/SnO 2 nanoparticles." *Sensors and Actuators B: Chemical* 114.1 (2006): 283-295.

[208] Kennedy, M. K., et al. "Effect of in-flight annealing and deposition method on gas-sensitive SnO x films made from size-selected nanoparticles." *Sensors and Actuators B: Chemical* 108.1 (2005): 62-69.

Chapter 3 Experimental apparatus

In this chapter, we introduce the two pre-existing apparatuses used in the works presented in the thesis: the magnetron sputtering cluster source with time-of-flight mass filter built by Birmingham Instruments (BI) and the aberration corrected scanning transmission electron microscope (JEOL 2100F). The magnetron sputtering cluster source with time-of-flight mass filter is one of the few techniques available to carry out controlled deposition of size-selected nanoclusters and is used for the cluster production work presented in Chapter 4. The aberration corrected scanning transmission electron microscope is a powerful tool with the potential to obtain abundant range of characterization data of nanoclusters, such as size and structure, and has been used to analyze the clusters produced both in the magnetron source and the matrix assembly cluster source (MACS). The schematics, basic principles and operation procedures of these two pieces ofapparatus are illustrated in this chapter. The imaging, effects of the electron beam and atom counting using the STEM are also discussed. The new technology we developed, the MACS, is described later in Chapters 5 and 6.

3.1 Magnetron sputtering gas condensation cluster beam source and lateral time-of-flight mass filter

3.1.1 Magnetron cluster source

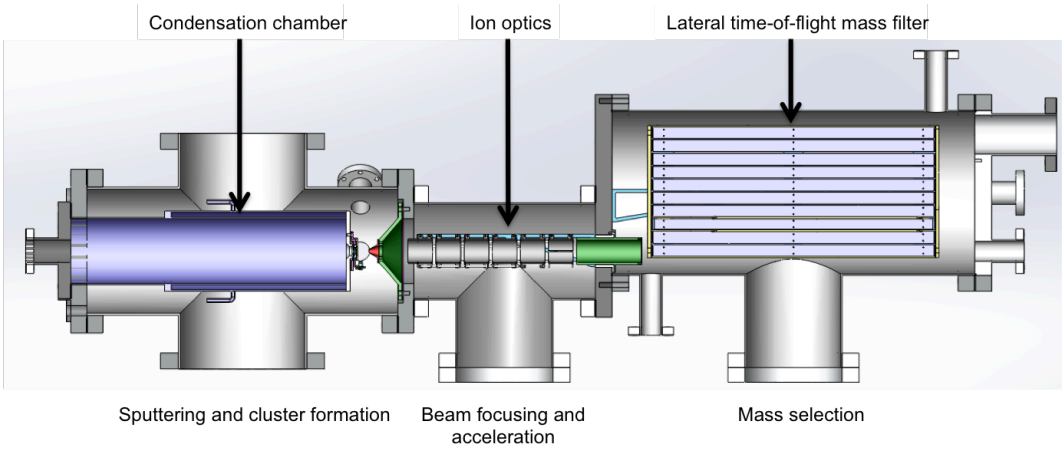

Figure 3.1 Schematic diagram of the magnetron sputtering gas condensation cluster source. It consists of three chambers: cluster generation chamber, ion optic chamber and mass filter chamber. (drawn by Jinlong Yin from Birmingham Instruments)

The schematic diagram of the magnetron sputtering gas condensation cluster beam source equipped with lateral time-of-flight mass filter (built by Birmingham Instrument) based in Nanoscale Physics Research Laboratory, University of Birmingham is shown in Figure3.1 [1]. The cluster beam source consists of three main chambers: cluster generation chamber, ion optic chamber and mass filter chamber.

The clusters are formed in the condensation chamber inside the generation chamber, which can be cooled by liquid nitrogen. In this chamber an atomic vapor is generated by magnetron sputtering of the bulk target [2]. The 2" magnetron gun is mounted on a linear drive, so that the position of the magnetron head can be varied from 150mm to 250mm inside the chamber. The sputtering gas used is Ar, injected from small orifices with diameters of around 0.1mm surrounding the magnetron head. The Ar plasma can be ignited by either a DC or RF power supply to create the atomic vapor including atomic ions and small clusters by sputtering the target. Ar ions are accelerated to a high energy by a large electric field formed between the plasma and the target due to the screening effect of the plasma. The sputtering power for both DC and RF power supplies can be varied from around 10W (minimum power to ignite Ar plasma) to 200W (limited by the power supply). For DC sputtering mode, a high negative potential is applied to the target which should be conductive. In the case of RF sputtering mode, a high voltage RF signal is coupled to the electrically isolated target to develop negative electrical field due to the great mobility of electrons. In this case, the target is not required to be conductive materials and it can be semiconductor and even insulators. The advantage of using magnetron sputtering to produce atomic vapor over other technique such as thermal evaporation is that a significant proportion (around 30%) of the sputtered material is already ionized [3]. No further ionization device is required to enable high energy deposition or mass selection. Behind the magnetron head there is an unbalanced array of strong magnets to further enhance the plasma density and ionization rate. The condensation of large clusters from the atomic vapor is promoted by collisions with induced helium gas from the back of the chamber.

The roles of the helium gas are not only for collision but also as the seeds for the formation of clusters at nucleation stage [4-9]. Both Ar and He flow rates are controlled by the mass flow controllers each with a maximum flow rate of 200 sccm. An adjustable nozzle (iris), 1mm to 10mm in diameter, is mounted at the end of the condensation chamber enabling control of the pressure in condensation chamber independently to the gas flow rate.

Clusters extracted from the condensation chamber are focused into a cluster beam in the ion optic chamber by applying an electrical field after supersonic expansion from the skimmer (5mm in diameter). All the ion optic lenses are negatively biased as well as nozzle and skimmer (biased with low negative voltage) as the mass filter of the cluster source has been designed to only select positively charged particles. We only select clusters propagating parallel to the axis of the cluster beam source, as the mass resolution is sensitive to the beam focus at the end of the mass filter. The ion optics system consists of 7 cylindrical lenses including a XY deflector and electrical field is created along the ion optic axis to focus cluster ions. Five lenses, lens1, lens2, lens3 and XY lenses, are connected to independent power supplies while the other two are biased to the beam potential which is 500V here. The power supplies for the ion optic lenses are the high voltage modules from Applied Kilovoltage up to -2.5kV. The beam potential is powered by a power supply from Glassman FL series up to -1kV. The optimum voltage settings on each lens vary with the size of selected clusters and the rough range is obtained by the simulation of the cluster beam trajectory in SIMION 8.1 [10]. The shape of the focused cluster beam passing through the ion

optics can be monitored by a Faraday cup at the white beam exit (the bottom exit of the mass filter).

3.1.2 Working principle of the lateral time-of-flight (ToF) mass filter

The focused cluster ion beam is then mass selected by the lateral time-of-flight (ToF) mass filter installed in the third chamber [11]. In the lateral ToF mass filter, a portion of the cluster ion beam is accelerated perpendicular to its original flight direction with a pulsed electric field in the bottom region and then stopped at the top region of the mass filter by another opposite pulsed electric field after letting it fly in the middle for a certain time. The cluster beam is therefore effectively spread out vertically after entering the mass filter and the magnitude of the displacement of the cluster ion beam under the same electric pulse is dependent on the charge mass ratio of the clusters and nearly all cluster ions are single charged. The mass selection is achieved with an aperture placed at the end of top region only allowing a small portion of the displaced ion beam flying through.

The schematic diagram of the lateral ToF mass filter is shown in Figure 3.2 [11]. The bottom region of the mass filter is called the acceleration region where the cluster ion beam is kicked upward by a pulsed electrical field. The middle region is called the flight region where is field free between two pulses. The top region is the deceleration region where the perpendicular movement is stopped by another opposite kick. The cluster beam enters the mass filter from the left side. A Faraday cup is mounted at the end of the bottom region, which should be the

focal point, to monitor the shape of the cluster beam. The length of the pulse is crucial to make sure no cluster is leaving the acceleration region before the pulse ends thus all cluster ions gain exactly the same momentum. The flight region is field free between two pulses. In the deceleration region, an identical high voltage pulse is applied on the top plate after all cluster ions with selected mass entering this region so that cluster ions will lose their perpendicular velocity and keep flying horizontally through the exit aperture at the end.

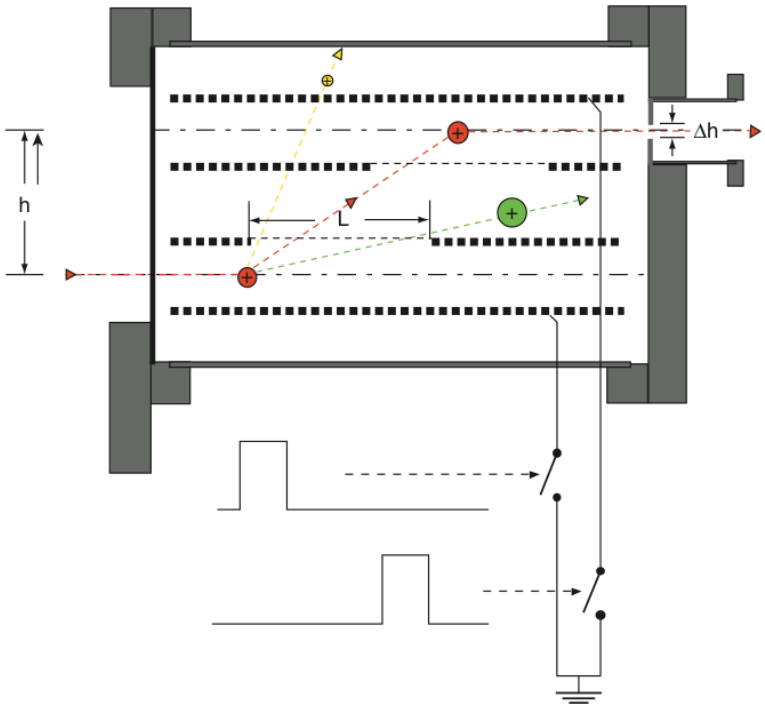

Figure 3.2 Schematic diagram of the lateral time-of-flight mass filter, reproduced from reference [11]. The cluster beam enters the mass filter from the left side. The cluster ion beam is kicked upward by a pulsed electrical field applied in the bottom region and stopped by stopped another opposite kick after flying into the top region. The mass selection is achieved with an aperture placed at the end of top region only allowing a small portion of the displaced ion beam flying through.

The two pulses applied in the acceleration and deceleration regions are identical but with a delay time τ_d. The pulse time and the waiting time between consecutive acceleration pulses are defined as τ_p and τ_w. a is the vertical distance covered by ions in acceleration region and deceleration region. b is the vertical distance of free flight region. d_1 and d_2 are the plates separations in pulse regions and flight region. l and s are the sideway lengths of cluster ion beam than can and cannot be used. x is the total displacement of the ion beam. L is the total length of the mass filter.

The first pulse starts when the acceleration region is fulfilled with cluster ions and stops when displacement a is covered by clusters with selected mass. Thus τ_p is

$$\tau_p = \frac{2a}{\sqrt{2eU_p/m}} = \frac{2a}{v_p}$$

where U_p and v_p are the energy and velocity of ions gained from the acceleration pulse. The second pulse starts when ions reach the deceleration region after flying through the flight region. Thus the delay time between two pulses is

$$\tau_d = \frac{b}{\sqrt{2eU_p/m}} = \frac{b}{v_p}$$

The waiting time between two consecutive allowing the ions to fill the acceleration region again is determined by the original velocity of ions, that is

$$\tau_w = \frac{s+l}{\sqrt{2eU_0/m}} = \frac{s+l}{v_0}$$

where U_0 and v_0 are the initial energy of cluster ions. The frequency of both acceleration and deceleration pulse is F

$$F = \frac{1}{\tau_p + \tau_w}$$

And the transmission ratio can be calculated

$$T = \frac{l}{(\tau_p + \tau_w)v_0} = \frac{l}{s + l + 2a(v_0/v_p)}$$

The mass resolution of the lateral ToF mass filter can be figured out from the displacement of ions as a function of mass. Assuming m_0 is the selected mass with a total displacement of x. The displacement x_m of cluster with mass m is

$$x_m = \frac{m_0}{m} x$$

The width of the selected mass range is given by the exit aperture size that

$$\Delta m = \frac{dm}{dx_m} \Delta x = -\frac{m_0}{x} \Delta x$$

Therefore the mass resolution is given by

$$R = \frac{m}{\Delta m} = \frac{x}{\Delta x}$$

To obtain better mass resolution, the cluster ion beam is required to be focused well at the end of the mass filter only so that the small difference on displacements of clusters with small mass difference can be distinguished. Also the shortest possible delay time is used to obtain high transmission efficiency. To avoid large mass cluster ions being accelerated by several pulses, a second pulse, which is the same as the deceleration pulse is also applied to two of the middle plates in flight region to create a swipe to remove any remaining large slow moving clusters.

3.1.3 Experimental apparatus of the lateral ToF mass filter

There are two lateral ToF mass filter setups in our lab, one installed in the magnetron sputtering gas condensation cluster source, the other one is attached to the MACS 1 system. The dimensions of these two setups are different. For the one connected with magnetron cluster source, the vertical displacement of the cluster beam is 184mm and the total length of the mass filter is 560 mm. Also exit apertures of different diameters (between 5 mm, 3 mm, 2 mm, 1 mm and 0.5 mm) can be used to enable control of the mass resolution. The mass filter in the MACS system is a smaller version with a shorter displacement of 120 mm and the total length is only 370 mm. The exit aperture is also fixed at 5 mm in diameter.

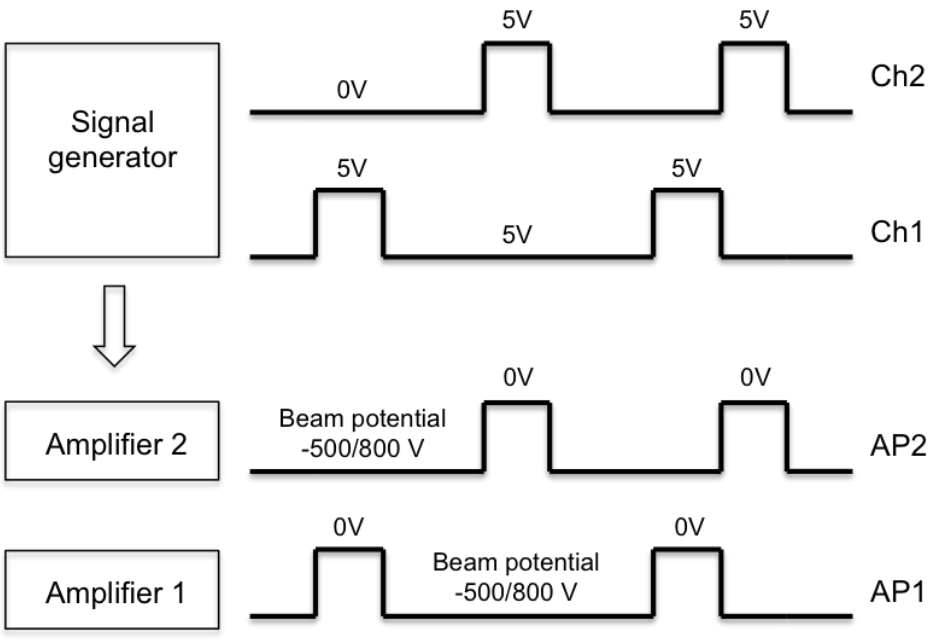

Figure 3.3 The pulse signals in the ToF mass filter. The high frequency pulse signal is generated by a signal generator where two channels of pulse signal (5 V) with a delay time are generated and delivered to two amplifiers to output the

high voltage pulsed signal (500/800 V) for acceleration and deceleration regions. The pulse width is set as 20% of the total pulse period and the delay time is 50% of the total period between two pulses.

The electronics of these two ToF mass filters are exactly the same. The high frequency pulse signal is generated by a signal generator from BNC (575-2h) where two channels of pulse signal (5 V) with a delay time are generated and delivered to two amplifiers from DEI (PVX4150) to output the high voltage pulsed signal for acceleration and deceleration regions as illustrated in Figure 3.3. The magnitude of the pulse is controlled by the beam potential voltage, which is applied by the high voltage powersupply from Glassman (FL series). The beam potential in the magnetron cluster beam source is set at -500 V, while -800 V in the MACS system. Both channels of pulse signals generated from the BNC single generator are square waves with magnitude of 5 V.

For these two mass filter systems the pulse signals are nearly identical except the frequency for the selected size varies slightly due to different total displacement. The pulse width is set as 20% of the total pulse period and the delay time is 50% of the total period between two pulses. The pulse signals are then amplified by two pulse generators before being delivered to the mass filter. For each pulse generator, it has two input channels and one output channel. The two input channels are connected to beam potential (Low) and ground (High) respectively. The output channel is connected to the assigned plates of the mass filter and output voltage is the difference between the Low and High input voltages dependent on the gate voltage (5V or 0V) which is a square wave signal.

All the plates of the ToF mass filter are biased at the beam potential when pulse is off. When pulse is on, the plates in the acceleration or deceleration regions are switched from beam potential to 0 V to give positive cluster ions a kick. For the mass filter in the MACS system, which has a vertical displacement of 120mm, the optimal pulse frequency of selected Ar clusters (mass=40 amu) is 203kHz, based on which frequency of any selected mass can be calculated.

3.1.4 Operation of the magnetron sputtering cluster source and sample deposition

The operation of the magnetron sputtering cluster source can be divided into following steps: preparation work, plasma ignition, optimization of the cluster beam (including tuning condensation conditions and ion optics, and mass spectra) and sample deposition.

Preparation work

The preparation work before producing clusters includes changing the target, cooling, mounting samples onto the sample holder and pumping down the chambers. Usually the base pressure of the cluster source is lower than 10^{-6} mbar in the generation chamber and 10^{-7}~10^{-8} mbar in ion optic chamber, mass filter chamber and deposition chamber. Liquid nitrogen cooling of the condensation chamber is also a necessity to prompt condensation when making large size clusters. The cooling process usually takes 1 hour from room temperature to ~77K.

Plasma ignition

To ignite the plasma, Ar gas flow is tuned to around 20sccm before switching on the magnetron. The power of the magnetron is usually set between 10 and 15W. After the plasma being ignited, Ar gas flow can be tuned down to around 5sccm to maintain a sputtering yield.

Optimization of the cluster beam

Optimization of the cluster beam is to achieve maximum cluster beam current, which involves tuning the condensation parameters, which are magnetron power, condensation length, Ar and He flow, condensation pressure, and optimizing the ion optics. The magnetron power can be accessed from the magnetron power supply and it can be varied from 10W to 200W. 200W is the limitation of the power supply while 10W is the minimum power to generate stable plasma. The condensation length can be varied by moving the position of the magnetron, which is mounted on a linear motion. Ar and He gas flow are controlled independently by the flow meter with a maximum flow rate of 200sccm. The pressure of the condensation chamber is controlled by adjusting the opening of the nozzle, which allows the condensation pressure independent from the gas flow rate. Ion optics is optimized by tuning the voltages on each lens. There are 7 ion optic lenses but only 3 of them are tunable plus the XY deflector. Others are all biased with beam potential. The cluster beam current is read from the sample holder placed after the mass filter, which is connected to the picoammeter (Kethley 6485). Between the sample holder and the mass filter there are three ion optic lenses (two are beam potential biased and only one is tunable) to maintain the focus of the cluster beam. The sample holder is

mounted in a linear motion and have several slots vertically arranged. The blank slot on the sample holder is used to monitor the cluster beam current during the optimization. The optimization process for large size clusters has to build up step by step. For example, to produce Au_{923} cluster, we have to tune for Au_1 or Au_3 first as small magic number clusters are more easily to produce and usually have higher current. Then we can tune for Au_{13}, Au_{55}, …, gradually build up to Au_{923}. The typical voltage settings of ion optics for producing Au_{923} cluster are listed in table 3.1, please note ion optic lenses biased with beam potential are not listed in the table.

Lens	Power supply No.	Voltage (V)
Skimmer	HV12	60
Lens1	HV1	1800
Lens2	HV14	500
Lens3	HV2	1200
Lens5, X+	HV3	500
Lens5, X-	HV4	500
Lens6, Y+	HV5	1100
Lens6, Y-	HV6	1100
Lens7	HV13	500

Table 3.1 The typical voltage settings of ion optics for producing Au_{923} cluster.

After achieving the optimal and stable cluster beam current, usually is above 10pA as noise level is ~5pA, of selected size, deposition is carried out by moving the sample into right position. The substrates we used in experiments are carbon film and sample holder is biased by the high voltage power supply (from Glassman FL series) and is connected to ground through the picoammeter

(Kethley 6485). Therefore, any charges delivered by cluster ions on substrate are transferred to ground efficiently that the deposition is not affected by the charging effect, and current is recorded by the picoammeter. The deposition energy is controlled by the bias voltage applied on the sample holder and coverage of the cluster is determined by the deposition time and beam current.

3.1.5 Mass spectra

The mass spectra is achieved by reading the cluster beam current while continuously sweeping the pulse frequency of the mass filter, for example from 108 amu to 108000 amu. The current is measured by Kethley 6485 picoammeter on sample holder. Two examples of mass spectrum of small Cu clusters less than 20 atoms and Ag clusters less than 100 atoms are shown in Figure 3.4 and 3.5.

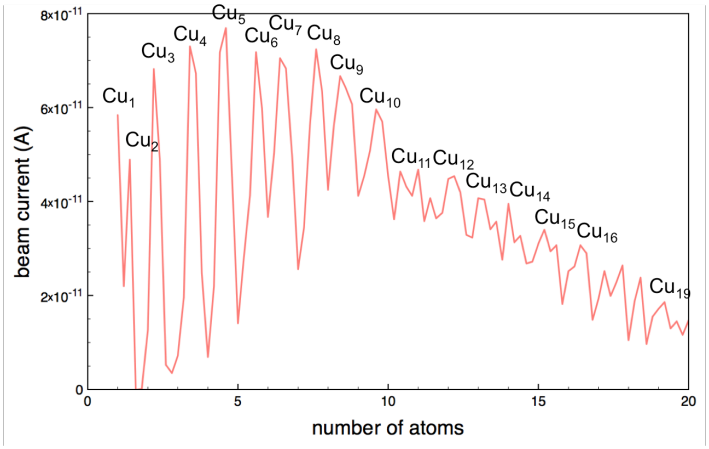

Figure 3.4 Mass spectra of Cu clusters produced in the magnetron sputtering gas condensation cluster source.

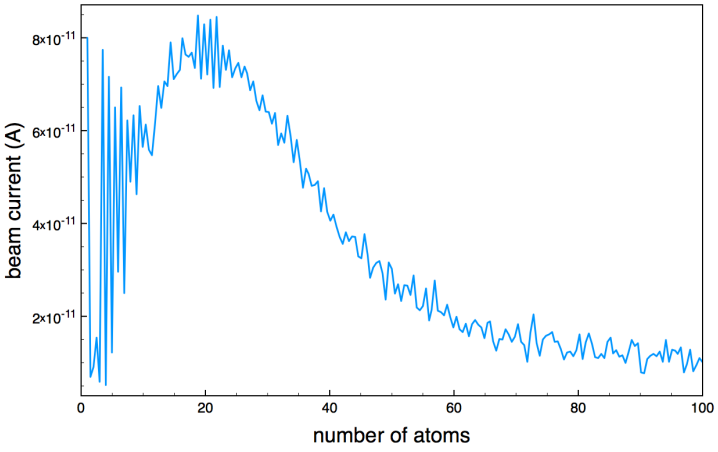

Figure 3.5 Mass spectra of Ag clusters produced in the magnetron sputtering gas condensation cluster source.

3.2 Aberration corrected scanning transmission electron microscope

3.2.1 Overview of JEOL 2100F

The electron microscope based in Nanoscale Physics Research Laboratory, University of Birmingham is a JEOL 2100F scanning transmission electron microscope (STEM) with CEOS aberration corrector up to the fifth order. The photograph and schematic diagram of internal structure of JEOL 2100F is shown in Figure 3.6.

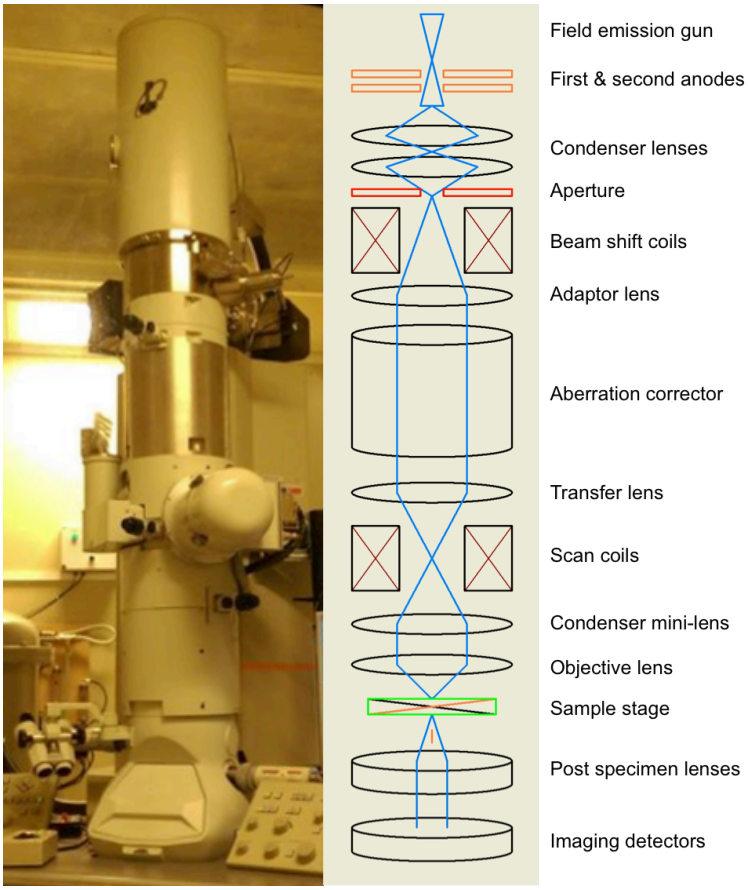

Figure 3.6 Photograph and schematic diagram of internal structure of JEOL 2100F scanning transmission electron microscope (STEM) with CEOS aberration corrector in NPRL, University of Birmingham.

Electron gun

In the JEOL 2100F, electrons are generated from a Schottky field emission electron gun (FEG) and are then extracted and accelerated to high energy by two electrodes in front of the gun. The tip of the FEG is made of tungsten with (100) surface coated with a layer of ZrO to reduce the work function barrier. The size of the tip is in nanometer scale so that the electric field between the tip and the first electrode is strong enough to extract electrons out of the tip. An acceleration voltage of 200kV is applied to the second electrode accelerating electrons to about 70% of the light speed. The electron gun is installed in a high vacuum chamber of pressure down to 10^{-9} Pa. The electron gun is slightly heated to avoid

contamination and to promote the emission efficiency. The focused electron beam probe is formed by electrons passing through 3 stages of electron optics system and the aberration of the electron beam is corrected by the aberration corrector prior to the specimen.

Electron optics

The working principle of the electron optics system is to generate electromagnetic fields by the lens coils in the condenser lens system to collimate and focus the electrons. Additionally, further coils are used to align the electron beam with the sample by tilting and shifting the beam. A set of apertures is mounted after the condenser lens system to remove the widely scattered electrons, and the most common aperture we used is 40μm in diameter.

Aberration corrector

The aberration correction system is installed after the condenser lens and aperture, where the aberration induced by the condenser lens is compensated. In our JEOL 2100F STEM, the aberration corrector used is CEOS double hexapole spherical aberration corrector consisting of two sets of 6 pole pieces and two sets of transfer lenses in the middle. An approximately circular field is generated by the two sets of hexapole elements with the dedicated rotational offset alignment to form a negative spherical aberration equivalent to the positive aberration induced by condenser lenses. The electron beam passing through the aberration corrector is then focused into a probe by the objective lens prior to

reaching the plane of the specimen. The scanning of the electron beam probe across the specimen surface is enabled by the scan coils. With the help of aberration correct the resolution of the STEM is pushed to 0.1045nm at the time of installation.

3.2.2 Imaging

Two different types of images are obtained from the STEM in the works presented in this thesis, high angle annular dark field (HAADF) image and bright field (BF) image. The schematic diagram illustrating the formation of HAADF image and BF image are shown in Figure 3.7. The HAADF image is contributed by high angle scattered electrons and collected using dark field detector from JEOL, which is similar to a donut. While the BF image is formed by electrons with narrow forward angles and collected by the detector from Gatan, which is a circular plate. Both detectors are installed beneath the specimen.

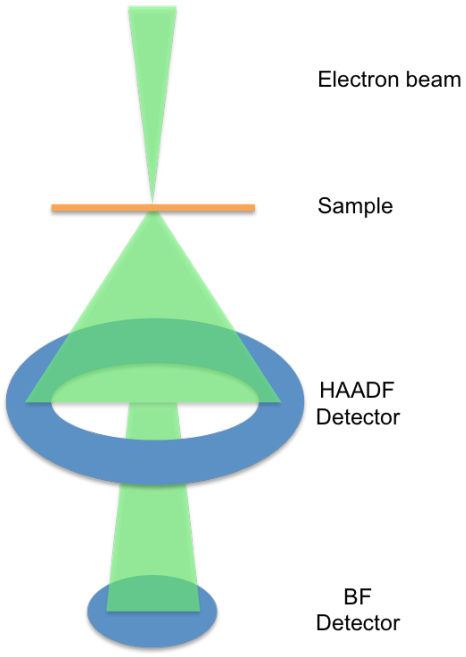

Figure 3.7 Schematic diagram illustrating the positions of HAADF detector and BF detector.

The advantages of HAADF image are that it exhibits sound atomic resolution and contains the quantitative information. HAADF images are formed by high angle scattered electrons which lose the coherence if the collection angle is large enough that the inner collection angle is more than three times of the beam convergence semi-angle (about 50 mrad). In that case, the electrons to form the HAADF image are not affected by the complicated phase change, instead they are determined by the elemental atomic number and the thickness and can be described by Rutherford scattering equation. The intensity of HAADF STEM image formed by high angle scattered incoherent electrons which follow the Rutherfold scattering equation is proportional to Z^2, Z is the atomic number. However, in reality the power exponent is affected by the screening of nuclear charge that the equation has to be modified to $I \sim tZ^{\alpha}$, α is usually varied with camera length in the STEM, which determines collection angle and convergence angle. In our STEM, the power exponent α is calibrated with help of size selected nanoclusters Au_{923} and Pd_{923} by ZW. Wang in 2011 for the condition of the inner and outer collection angle of 62 and 164mrad and convergence angle of 19mrad [12]. In the calibration, average intensities of size selected Au_{923} and Pd_{923} are measured respectively over large populations. The power exponent α is then obtained based on the equation

$$\frac{I_{Au}}{I_{Pd}} = (\frac{Z_{Au}}{Z_{Pd}})^{\alpha}$$

that $\alpha = 1.46 \pm 0.18$ [12].

The electrons reaching the BF detector are assumed to retain the coherence as they are only be scattered within very small angles. Thus the phase change due to interactions between electrons and sample and fine lattice structural details can be revealed using the BF images.

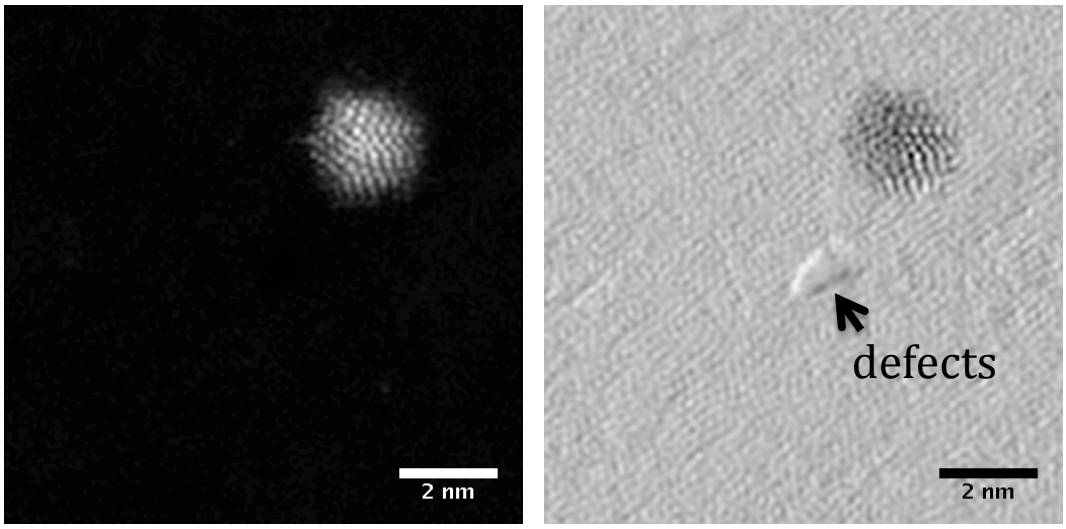

Figure 3.8 HAADF image and BF image of size-selected Au_{309} cluster deposited on FLG surface. The atomic structure of the Au cluster is clearly revealed in both the HAADF image and the BF image. However, the lattice structure of the FLG is only visible in the BF image as well as the defects on the FLG surface.

Examples of HAADF image and BF image of size-selected Au_{309} cluster deposited on few-layer graphene (FLG) surface are shown in Figure 3.8. The atomic structure of the Au cluster is clearly revealed in both the HAADF image and the BF image. However, the lattice structure of the FLG is only visible in the BF image as well as the defects on the FLG surface. Hydrocarbons on the FLG surface are also detectable using BF image as reported in chapter 4.1.

On the other hand, HAADF image has its irreplaceable advantage, which is quantitative information. For example, the intensity of the size-selected Au_{309} cluster can be used as the mass balance to measure the thickness of the graphene film, which is used in Chapter 4.1 to determine the number of layers of the FLG. Also in chapter 5 and chapter 6, the number of atoms of clusters produced in the matrix assembly cluster source is measured by the HAADF intensity of single atoms and size-selected Au_{923} clusters.

3.2.3 Effect of electron beam

The effect of high-energy electron beam on nanocluster structures has already been investigated by Wang and Palmer in 2012, where they found the structure of Au_{923} cluster is transferring under the electron beam from icosahedral to decahedral or fcc. The mechanism of the structural transformation under high-energy electron is that nanoclusters absorb energy from the electron beam to drive them through the energy threshold to reach more equilibrated state. The same phenomenon is also observed in our work when successively taking images on the same Au_{923} cluster. The time between each photo shoot is 5s and the structure of the Au_{923} is changed from icosahedral to fcc after 160s. The first shoot HAADF image and images taken at 30s, 80s and 160s are shown in Figure 3.9.

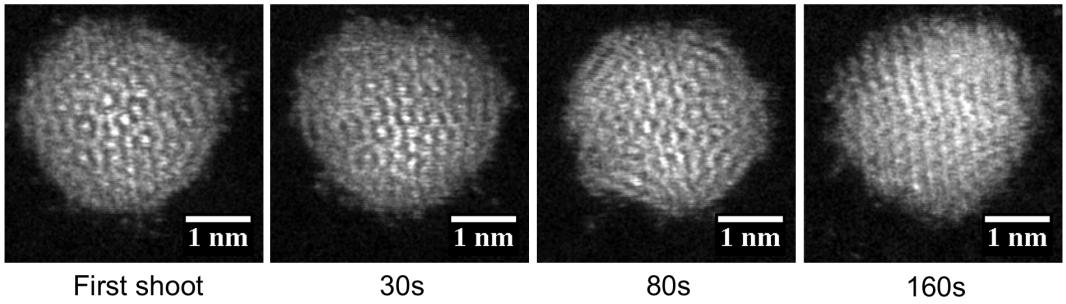

Figure 3.9 HAADF images of the same Au_{923} taken at first shoot, 30s, 80s and 160s. The structure of the Au_{923} is changed from icosahedral at the beginning to fcc after 160s.

Another primary effect of electron beam on clusters is "beam shower". Beam shower is used to expose the sample to a defocused electron beam for a certain time to fix contaminations such as hydrocarbon on the surface. It has been widely used when imaging samples using STEM mode, as surface hydrocarbons are more easily accumulated around the focused electron beam. In order to immobilize hydrocarbons, the duration of the beam shower time is usually between 15mins and 30mins. With such a long time, not only cluster structure but also the cluster size may be affected. Moreover, small clusters (less than 100 atoms) are likely to be destroyed during the beam shower. Figure 3.10 is HAADF images of two Au clusters under beam shower for 50mins. Images are taken at every 10mins. As seen from the images, structures of both clusters keep changing and atoms break away from the clusters due to the exposure under the electron beam.

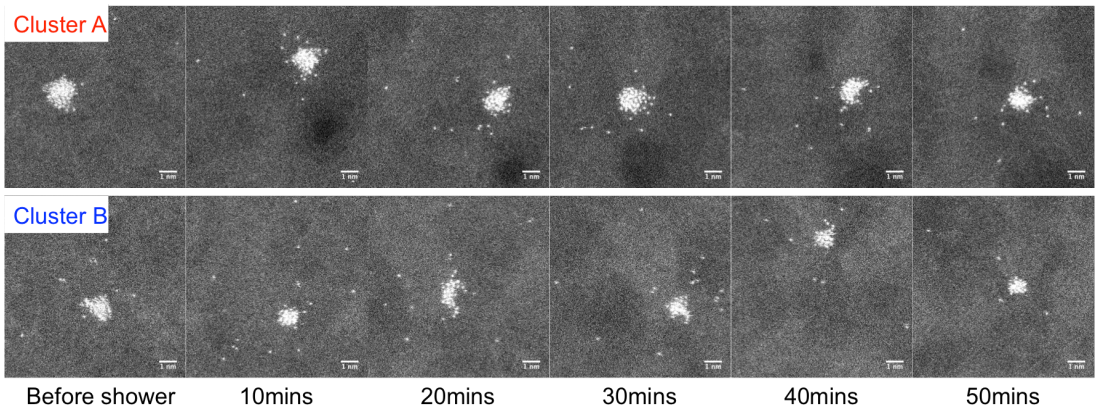

Figure 3.10 HAADF images of two Au clusters under beam shower for 50mins. Images are taken at every 10mins. The structures of both clusters keep changing and atoms break away from the clusters due to the exposure under the electron beam.

As discussed above, the electron beam may have an effect on both cluster structure and cluster size, which will cause errors when determining the cluster structure or measuring cluster size using electron microscope especially STEM mode. To minimize these errors, as in chapter 4, all images used for structural assignment are taken at the first shot and without beam shower. The HAADF images of clusters prepared in the MACS, in chapter 5 and chapter 6, also avoid beam shower to obtain accurate size measurements. There are several approaches available to eliminate the contaminations without beam shower, such as leaving the sample in the microscope for a few hours to remove contamination in vacuum and with liquid nitrogen cooling. Also one could use a plasma source to process the sample, although this was not available at the time of the experiments.

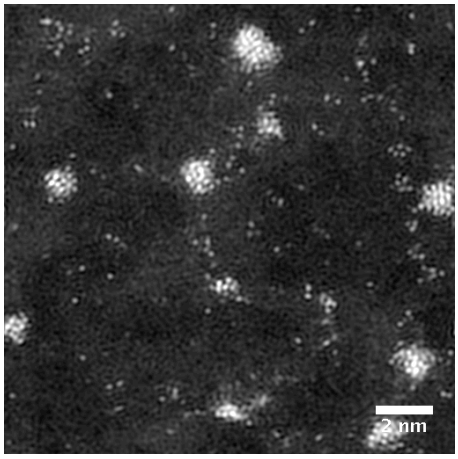

Figure 3.11 HAADF image of Ag clusters after 20mins beam shower and large number of single atoms are visible.

On the other hand, beam shower has its own utility in the size measurement of cluster size. In chapter 5 and chapter 6, the size of cluster produced in the MACS is measured by comparing the HAADF intensity using mass balance (single atoms). The beam shower is an efficient approach to break enough single atoms away from the clusters. An example of HAADF image of Ag clusters after 20mins beam shower is shown in Figure 3.11, where large number of separated single atoms is visible.

3.3 Atom counting of clusters produced in MACS

Clusters produced in the MACS are deposited on the amorphous carbon film coated TEM grid. These samples are then analyzed in the aberration-corrected scanning transmission electron microcsopy (ac-STEM). Both high angle annular dark field (HAADF) images and bright field images are obtained from samples. The HAADF images are used to get quantitative data such as cluster density and

cluster size distribution, while bright field images provide cluster structures in better contrast. The cluster flux is calculated based on the cluster density measured from HAADF STEM images then divided by deposition time instead of directly measuring the current. Two reasons are: not all the clusters produced are positively charged, as there are also negatively charged and most portion is neutral as found in the charge fraction experiment later. The current measured on the cold finger is a mixture of cluster beam current, Ar ion beam current through the matrix and secondary electron generates during the collisions when the Ar ion beam hits the matrix. The size of clusters is measured from the integrated HAADF intensity by comparing with the HAADF intensity of mass balance, which is single atom here. Single atoms can only be seen at high magnification in STEM that atoms are coming off due to the fragmentation of clusters under high energy electron beam [13-14]. In order to avoid clusters damaged by the electron beam, the HAADF images of clusters is taken at low magnification (2Mx). Moreover, different pixel sizes are usually used in high and low magnification images. Generally, HAADF intensity of a cluster or single atom at different magnifications and different resolutions can be described by the following equation, where the HAADF intensity is proportional to pixels that the cluster takes times the time electron beam scanning over one pixel.

$$\boldsymbol{I \propto K \times Area\ (total\ pixels\ covered\ by\ cluster)} \\ \boldsymbol{\times Time(electron\ beam\ scanning\ over\ one\ pixel)}$$

Here *K* is related to the settings in the microscope. In this work, all the settings (energy of electron beam, camera length, spot area, contrast and brightness) are not changed that K can be regard as a constant. The time for the electron beam to

scan over one pixel can be set in the microscope as well. For standard settings, pixel times at 1024×1024 and 512×512 are 19μs and 38μs respectively. Therefore, the general equation of weighing clusters by intensity of single atoms at different magnification is given by

$$N = \frac{I_{cluster}}{I_{single\ atom}} \times \frac{MAG^2_{single\ atom}}{MAG^2_{cluster}} \times \frac{Pixels_{single\ atom} \times Time_{per\ pixel\ single\ atom}}{Pixels_{cluster} \times Time_{per\ pixel\ cluster}}$$

This equation is verified by weighting the size of size-selected Pd120 clusters using HAADF intensity of single atoms. The size selected Pd clusters are produced in magnetron sputtering cluster source through ToF mass filter.

All the STEM images are processed using ImageJ [15]. The HAADF intensity of clusters is measured via the two-circles method to subtract the contribution of the background, as shown in Figure 3.12(a). Firstly, a large circle is drawn around a cluster and the total intensity *I1* inside the circle and the area *A1* are automatically obtained. Then a small circle (larger than the cluster) is drawn around the cluster inside the large one. The intensity *I2* and area *A2* of the ring between the two circles are obtained. The integrated HAADF intensity I2 is contributed by the background only. With this, the intensity of the background inside the large circle can be calculated as

$$I_3 = \frac{I_2}{A_2} \times A_1$$

Therefore the intensity of the cluster excluding background is

$$I = I_1 - I_3 = \frac{I_1 \times A_2 - I_2 \times A_1}{A_2}$$

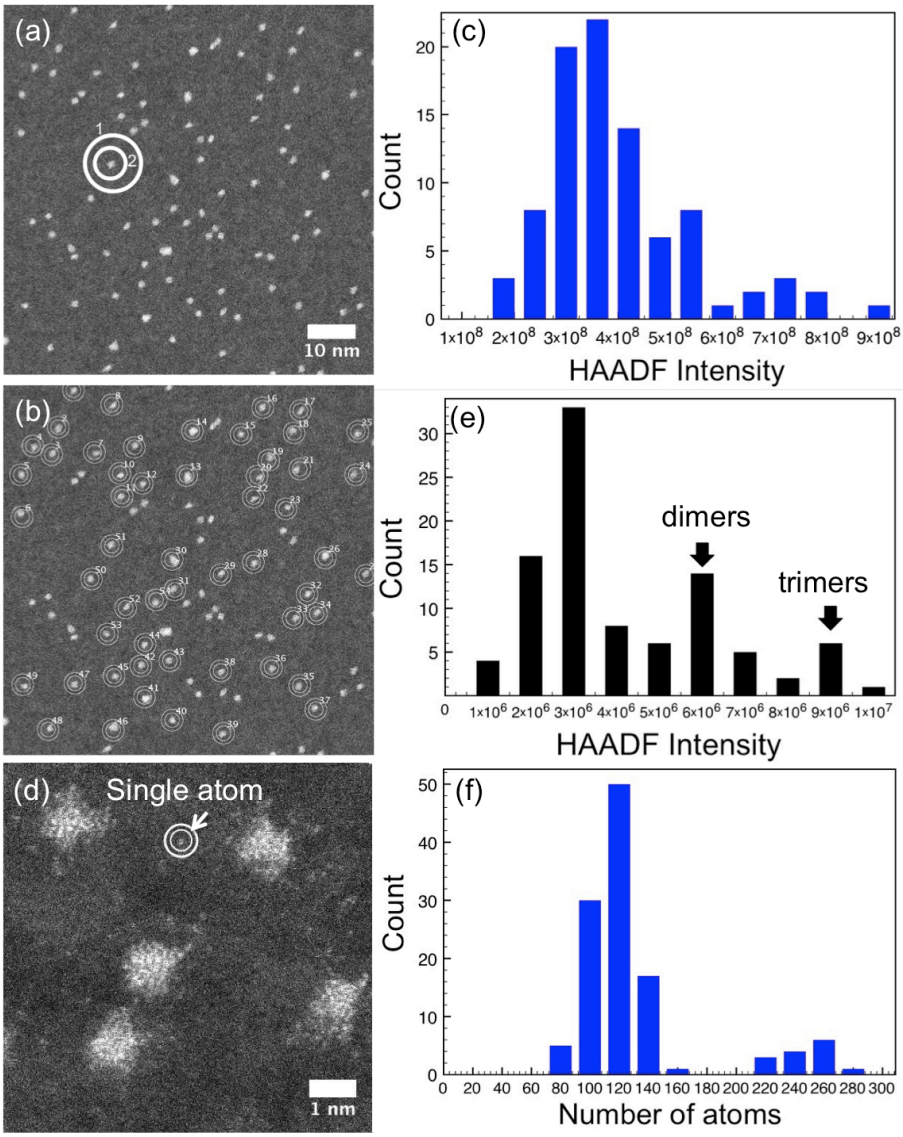

Figure 3.12 (a) HAADF STEM image (2Mx, 1024x1024) of size-selected Pd_{120} clusters produced using the magnetron sputtering cluster source equipped with lateral ToF mass fitler. The integrated HAADF intensity of cluster is measured using the two-circle method for background subtraction. (b) Automatic measurement of integrated HAADF intensity using script written by Dr. K. Arkill. (c) The measured integrated HAADF intensity distribution of Pd_{120} clusters. (d) High magnification HAADF STEM image (12Mx, 512x512) of Pd_{120} clusters for measurement of intensity of single atoms. (e) The measured integrated HAADF intensity distribution of Pd atoms. The primary peak is single Pd atom and

second and third peaks belong to dimers and trimers respectively. (f) The calculated size distribution of the size-selected Pd_{120} clusters.

A script is written by Dr. K. Arkill to measure the HAADF intensity of clusters automatically, as shown in Figure 3.12(b). The corresponding integrated HAADF intensity distribution of the clusters is shown in Figure 3.12(c). Diameters of the two circles are both adjustable for different clusters and are kept uniform during the measurement to reduce the error. The HAADF intensity of single Pd atoms is measured from high magnification HAADF images (usually more than 6Mx depending on the atomic number) using the same methods, as shown in Figure 3.12(d). The obtained intensity distribution of single atoms is shown in Figure 3.12(e). Three peaks are found in the intensity distribution. The first peak is the intensity of single Pd atoms, while the second and third peak are supposed to be the dimers and trimers. Therefore, the number of atoms in clusters is

$$N = \frac{I_0}{I_{A0}} \times \frac{12^2 \times 512 \times 512}{2^2 \times 1024 \times 1024} \times \frac{38}{19}$$

Here I_{A0} is the peak intensity of the intensity distribution of single atoms and I_0 is the intensity of the size-selected Pd clusters. The calculated size distribution of the size-selected Pd_{120} cluster is shown in Figure 3.12(f). The second peak shown in the histogram of size distribution around 240 is due to the double charge or the aggregation of clusters. To lower the statistical error, over 100 images were taken for each sample from five different mesh areas to get the size distribution as well as cluster flux.

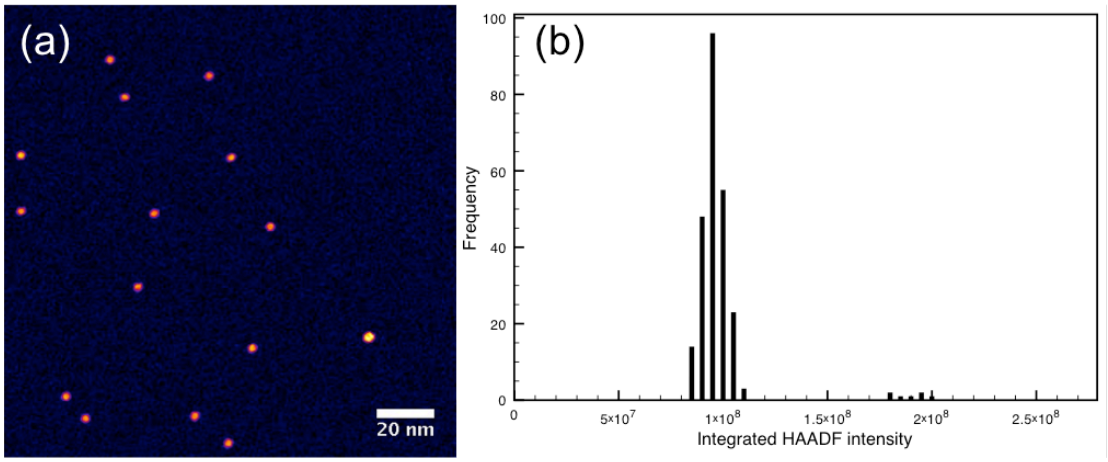

Figure 3.13 (a) HAADF STEM image of size-selected Au_{923} produced using magnetron sputtering cluster source with a mass resolution of ±5%. (b) The integrated HAADF intensity distribution of the Au_{923} clusters. The primary peak value of the HAADF intensity distribution is chosen as the mass balance. The secondary peak is the dimers, which is due to the doubly charged clusters or aggregation.

For the Au clusters produced using the MACS apparatus, size-select Au_{923} clusters prepared in the magnetron sputtering cluster source with a mass resolution of ±5% were used as the mass balance for atoms counting. To minimize the systematical error, HAADF STEM images of clusters both produced in the MACS and size-selected Au_{923} are taken with exactly same electron microscope conditions such as beam current (127μA), exposure time (38μs) and pixel size (512x512). A HAADF STEM image of size-selected Au_{923} is shown in Figure 3.13(a). The integrated HAADF intensity distribution of the clusters is shown in Figure 3.13(b). The primary peak value of the HAADF intensity distribution is chosen as the mass balance. The secondary peak is the dimers, which is due to the doubly charged clusters or aggregation.

List of references

[1] Pratontep, S., et al. "Size-selected cluster beam source based on radio frequency magnetron plasma sputtering and gas condensation." *Review of scientific instruments* 76.4 (2005): 045103.

[2] Smith, Roger. *Atomic and ion collisions in solids and at surfaces: theory, simulation and applications*. Cambridge University Press, 2005.

[3] Haberland, Hellmut, et al. "Thin films from energetic cluster impact: a feasibility study." *Journal of Vacuum Science & Technology A* 10.5 (1992): 3266-3271.

[4] Hall, S. G., et al. "Compact sputter source for deposition of small size-selected clusters." *Review of scientific instruments* 68.9 (1997): 3335-3339.

[5] Wucher, A., and M. Wahl. "The formation of clusters during ion induced sputtering of metals." *Nuclear Instruments and Methods in Physics Research Section B: Beam Interactions with Materials and Atoms* 115.1 (1996): 581-589.

[6] Granqvist, C. G., and R. A. Buhrman. "Ultrafine metal particles." *Journal of Applied Physics* 47.5 (1976): 2200-2219.

[7] Olynick, D. L., J. M. Gibson, and R. S. Averback. "Impurity-suppressed sintering in copper nanophase materials." *Philosophical Magazine A* 77.5 (1998): 1205-1221.

[8] Soler, J. M., et al. "Microcluster growth: transition from successive monomer addition to coagulation." *Physical Review Letters* 49.25 (1982): 1857.

[9] Hihara, Takehiko, and Kenji Sumiyama. "Formation and size control of a Ni cluster by plasma gas condensation." *Journal of applied physics* 84.9 (1998): 5270-5276.

[10] Manura, David J., and David A. Dahl. "Simion Version 8.0/8.1 User Manual." (2011).

[11] Von Issendorff, B., and R. E. Palmer. "A new high transmission infinite range mass selector for cluster and nanoparticle beams." *Review of Scientific Instruments* 70.12 (1999): 4497-4501.

[12] Wang, Z. W., et al. "Quantitative Z-contrast imaging in the scanning transmission electron microscope with size-selected clusters." *Physical Review B* 84.7 (2011): 073408.

[13] Li, Z. Y., et al. "Three-dimensional atomic-scale structure of size-selected gold nanoclusters." *Nature* 451.7174 (2008): 46-48.

[14] Young, N. P., et al. "Weighing supported nanoparticles: size-selected clusters as mass standards in nanometrology." *Physical review letters* 101.24 (2008): 246103.

[15] Abràmoff, Michael D., Paulo J. Magalhães, and Sunanda J. Ram. "Image processing with ImageJ." *Biophotonics international* 11.7 (2004): 36-42.

Chapter 4 Deposition of size-selected gold nanoclusters

Two parts of works are included in this chapter with combined techniques of cluster production using magnetron cluster source and characterization using ac-STEM. In the first part, the size dependent propagation of clusters through few-layer graphene (FLG) is explored. This work enables the control of properties of graphene-based materials and other membranes, which have potential in application of selective permeation filter. The second part investigates the control of nanocluster structures (Au_{923}) during the formation stage in the gas phase. The breakthrough of this work offers a routine to study the properties of clusters not only as a function of size but also isomer configurations. It also provides possibility of production of isomerically pure clusters for applications such as catalysis. Although the works presented in this chapter reveal the vast potential of nanoclusters, the bridge connecting the fundamental demonstration and the applications is, we believe, abundant production. This is our motivation to develop the matrix assembly cluster source, which will be discussed in Chapter 5 and Chapter 6.

The works presented in this chapter are the results of collaboration between the author and co-supervisor, Dr. Simon Plant. The ideas of these two experiments were both from Dr. Simon Plant. The sample preparation was done by Dr. Simon Plant. Sample characterization using ac-STEM was done by the author. Data analysis and discussion were contributed by both the author and Dr. Simon Plant. The two parts of works were published on Nanoscale [1] and JACS [2] respectively.

4.1 Size-dependent propagation

4.1.1 Overview

Through the development of cluster ion beam technology and the mass selection technique, highly controlled deposition of clusters is achieved not only for size but as well as for surface coverage and deposition energy [3-4]. This has enabled the interactions between nanoclusters and the substrates surface to be carefully analysed, which in turn promotes the development of novel materials with applications on a variety of areas [5-6].

Deposition of nanoclusters onto graphene offers a way to alter and tailor their properties, which also enables one to explore the interaction between nanoclusters and the graphene's surface as previously reported of size selected Pd nanoclusters deposited on supported graphene [7-8]. The interaction between metals and graphene is a cutting-edge topic because of the increasing interests on metal-graphene composite materials and the promising properties

of metal on graphene based electronics [9-10]. Gold as model metal cluster deposited on graphene via solution or coating has been studied intensively in last few years using electron microscope especially on its behavior or dynamics on the graphene film [11-15]. Researches have demonstrated the enhanced chemical sensitivity of graphene decorated with metal nanoclusters, which has potential applications such as sensing [16-18].

In this work, Au nanoclusters with two different sizes are deposited onto few layer graphene (FLG) surface under specific deposition energy to demonstrate the size dependent propagation through few layer graphene, via the mechanism of defect generation. Although the graphene membrane is atomically thin and it is impermeable, its properties can be tuned and could be used as a selectively permeable membrane after the defect generation by size selected nanoclusters [19-21]. In previous work, defect generation by size selected nanoclusters have been reported to decorate nanoporous membrane which is similar to atomic ion bombardment of graphene [22-23]. Also the deposition of size selected Ag nanoclusters from 3 to 5000 atoms on graphite has been investigated intensively [24-36]. Here, size selected Au55 nanoclusters was used to bombard graphite surface first to create defects in order to determine the implantation depth of nanoclusters under specific deposition energy using scanning tunneling microscope (STM). This technique is then transferred to suspended FLG film and use aberration corrected scanning transmission electron microscope (ac-STEM) to track the fates of deposited Au_{55} and Au_{923} clusters.

4.1.2 Sample preparation and implantation depth of nanoclusters into graphite

The size selected Au nanoclusters are prepared in the magnetron sputtering gas condensation cluster source as introduced previously. The size of clusters is selected by the lateral time-of-flight mass selector prior to the deposition onto the substrate. The mass resolution used for both Au_{55} and Au_{923} are $M/\Delta M=20$, which is determined by the exit aperture size of the mass filter [37-39]. The deposition energy of clusters is controlled by the bias voltage applied on the substrate. The coverage of nanoclusters on the substrate is monitored by the beam current and the integrated deposition time. Size selected Au55 nanoclusters are first produced to study the implantation depth of nanoclusters into the highly ordered pyrolytic graphite (HOPG, grade ZYB). The surface of the HOPG is freshly cleaved and the deposition energy of the Au55 nanoclusters is 5keV determined by the bias voltage on the substrate. After deposition the HOPG is transferred to the tube furnace immediately after removal from vacuum chamber, where the HOPG is etched oxidatively at 650°C for 3mins in ambient atmosphere to widen the nanoscale implantation channels laterally created by the nanoclusters, which are reactive to oxygen, enable to be measured by the STM tip. While the depth of the channels remain the same as the bottom is defect free. The etch pits are then analyzed in bench top STM (Veeco Digital Instruments Nanoscope IIIa) in ambient atmosphere to obtain the implantation depth. A mechanically cut Pt/Ir wire is used as STM tip and typical tunneling parameters we used are 0.5V bias voltage on the tip and tunneling current of 0.5nA.

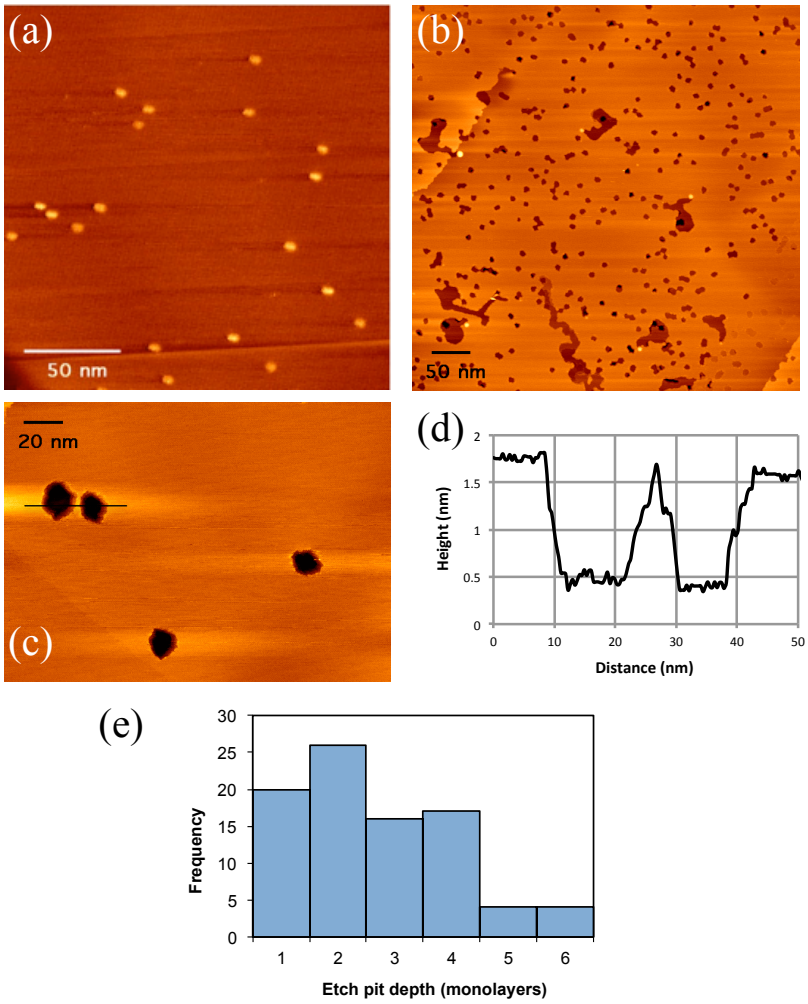

Figure 4.1 (a) STM image of HOPG surface deposited with size selected Au_{55} at energy of 5keV without etching. The bright spots are the defects owing to the bombardment with Au_{55} clusters. (b) STM image of HOPG surface deposited with size selected Au_{55} at energy of 5keV after oxidative etching at 650°C for 3mins. (c) The zoom in STM image of HOPG surface deposited with size selected Au_{55} at energy of 5keV after oxidative etching and the line across two etch pits shows the typical depth analysis method. (d) The corresponding line profile plot of the depths. (e) The frequency distribution of the measured depths of etch pits. Reproduced from reference [1].

The STM images of HOPG surface with implantation of Au_{55} at 5keV are shown in Figure 4.1. Figure 4.1(a) is the STM image of HOPG surface implanted by size selected Au_{55} nanoclusters at 5keV but without oxidative etching. The bright spots are the defects on the graphite lattice created by clusters land on the surface. However, as diameter of Au_{55} is less than 1nm, the defects owing to Au_{55} nanocluster implantation is too narrow to be measured by the STM tip in ambient atmosphere. Therefore the oxidative etching is a necessity to widen the nanoscale channels laterally to enable the STM measurement. The STM image of HOPG after Au_{55} implantation and after oxidative etching is shown in Figure 4.1(b). The depth of resultant each etch pit is measured by a line profile plot, as shown in Figure 4.1(c) and 4.1(d), to obtain the depth distribution as shown in Figure 4.1(e).

The histogram of depth distribution shown in Figure 4.1(e) does not represent the actual implantation depth of nanoclusters into graphite [38]. Although the defects created by clusters implantation expand laterally during oxidative etching, the lattice damage is also partially healed when annealing the HOPG at high temperature [32]. The final depth of the resultant etch pits is the dynamic competition between the oxidative etching and the thermal annealing that reducing the depth of many etch pits, which have been investigated previously by Ag cluster implanted into graphite with MD simulations. The results indicate the maximum depth of resultant etch pits gives the nanocluster implantation depth which is 6 layers for Au_{55} with implantation energy of 5keV, which means the Au_{55} nanoclusters deposited at 5keV is able to penetrate 6 monolayers graphene film. This number consists well with the previously measured pinning

energy threshold, the required energy to make a point defect on a single monolayer graphite lattice, which is 0.75keV for Au_{55} [41-42]. Extrapolated from the pinning energy, the implantation depth is equivalent to 6.7 layers where the error is within 1 monolayer from experimental results.

4.1.3 Controlled deposition of size selected Au_{55} and Au_{923} on FLG

The few layer graphene (FLG) film used in this work is grown by CVD with an average thickness of the FLG is 4 monolayers suspended on Cu TEM grid (from Graphene Laboratories Inc.). Size selected Au_{55} nanoclusters are produced in magnetron sputtering cluster source and deposited on the FLG with deposition energy of 5keV. The FLG deposited with Au_{55} nanoclusters is studied in the aberration-corrected scanning transmission electron microscope (STEM). Both bright field (BF) and high angle annular dark field (HAADF) images are taken to examine the FLG as well as the deposited clusters. The STEM image reveals the thickness of the FLG film varies across the surface. Also hydrocarbons coating is observed on the FLG surface from STEM images that might affect the interaction between Au cluster and the FLG surface. Depositing nanoclusters onto hydrocarbon-based surface have been studied previously both for grahene produced by micromechanical exfoliation (pristine graphene) and CVD growth [11-12]. As indicated in those studies e.g. evaporating Au atoms onto graphene, Au atoms cannot bond to clean graphene monolayer that they are observed as single atoms or only aggregate around surface hydrocarbons, although Au bond to clean few layer graphene surface has been reported [11-12].

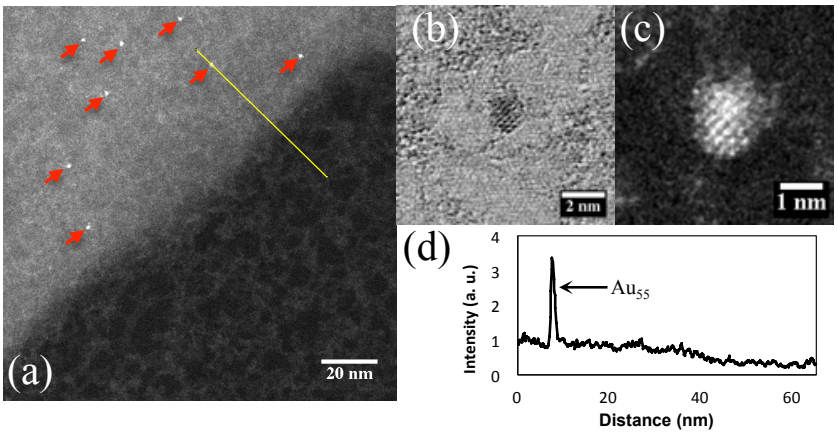

Figure 4.2 (a) HAADF STEM image of FLG taken at step edge bombarded of Au_{55} clusters with deposition energy of 5keV. The thin region of the FLG is about 2 monolayers. (b) BF STEM image of a Au_{55} clusters left on thick FLG surface showing the lattice adjacent between FLG and the cluster. (c) HAADF STEM image of the same Au_{55} cluster showing the atomic structure. (d) Integrated HAADF intensity profile plot from the line drawn in (a). Reproduced from reference [1].

In our work Au_{55} nanoclusters deposited on the FLG surface has energy of 5keV, which is nearly 7 times far above the pinning threshold for Au_{55} (0.75keV). Therefore, all Au_{55} nanoclusters are supposed to have sufficient kinetic energy to propagate through the FLG surface and any Au_{55} nanoclusters left on the surface are either pinning into the thick FLG area or bounded with hydrocarbons and they are immobile. Figure 4.2(a) are the HAADF STEM image of FLG film with high energy deposited Au_{55} nanoclusters taken at a step edge, the bright region on the top left is corresponding to the thicker FLG film while the dark region on the bottom right is the thinner FLG film. As shown in the Figure 4.2(a), Au_{55} nanoclusters can be found in the thicker region only where clusters are pinned into FLG or trapped by surface hydrocarbons. However it is completely cluster

free in the thinner region indicating all clusters propagate straight through the thin layer FLG film. The size selected Au_{55} nanoclusters left on the thicker FLG film can be used as the mass balance to estimate the thickness of the FLG film by the integrated HAADF intensity using following equation [43-44].

$$R = \frac{I_{Au}}{I_C} = \frac{N_{Au}}{N_C}(\frac{Z_{Au}}{Z_C})^{\alpha}$$

where the R is the ratio of intensities of Au clusters (I_{Au}) comparing with carbon (I_C) in selected area. N_{Au} is the number of atoms in the cluster which is 55 here. N_C is the number of carbon atoms in the selected area. Z_{Au} and Z_C are the atomic number of Au and C. α=1.46±0.18 which is determined by the collection angle of the HAADF detector and has been calibrated before [45]. Therefore, the thickness of the thinner FLG region is equivalent to 2 monolayers while the thicker region is about 8-9 layers, after subtracting the general background. A bright field (BF) STEM image of an individual Au_{55} cluster landed on the thicker FLG region is shown in Figure 4.2(b). As the deposition energy is much higher than the pinning energy of Au_{55}, the cluster is trapped on the surface by either pinned into the thick FLG film (about 8~9 monolayers measured by size selected Au_{55}) or immobilized by surface hydrocarbons. The initial kinetic energy of the cluster is dissipated by the deformations owing to the cluster landing on the surface, including both plastic and elastic, of the cluster, FLG film and surface hydrocarbons. Also lattice of the FLG film and surface hydrocarbons are visible on this BF-STEM image. Figure 4.2(c) is the HAADF STEM image of the size selected Au_{55} cluster, same one in the BF-STEM image, exhibiting fcc-type region identified by comparing the lattice structure with the simulated structural

isomers [46]. The observed high symmetry structure of the cluster indicating there is no fragmentation when the cluster landed on the surface suggesting the landing process of the cluster is buffered by the surface hydrocarbons which work as a breaking cushion [47]. However, the FLG lattice is not visible in the HAADF STEM image as the contrast of the HAADF image is a function of atomic number. Figure 4.2(d) is the intensity plot of the line profile drawn in Figure 4.2(a) perpendicular to the step edge of the thick and thin FLG film regions and across a Au_{55} cluster which is corresponding to the sharp spark in the plot.

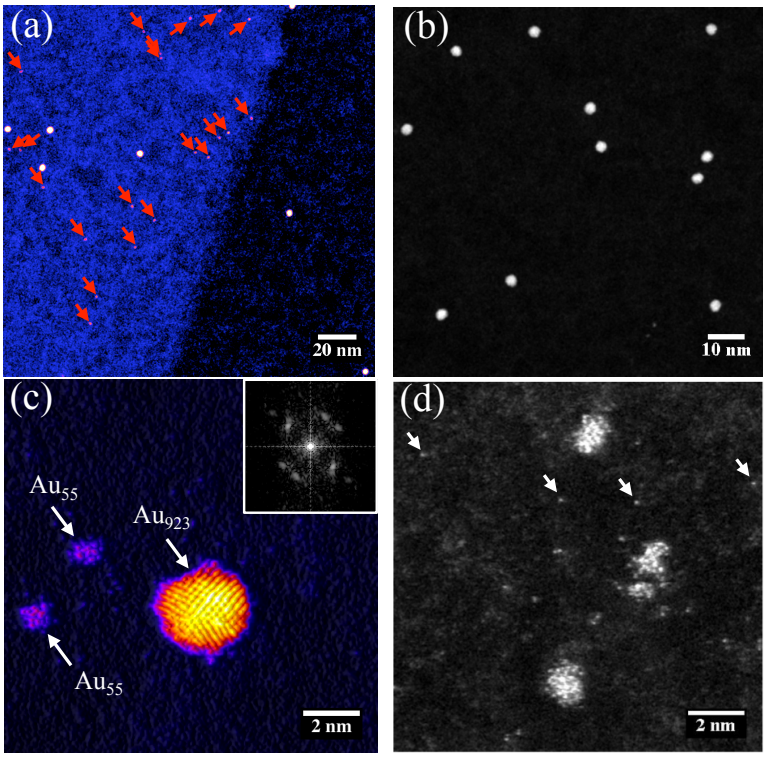

Figure 4.3 (a) HAADF STEM image of FLG taken at step edge bombarded of both size selected Au_{55} and Au_{923} clusters with deposition energy of 5keV. The thinner region of the FLG is about 3-4 monolayers and only Au_{923} clusters reside there. Au_{55} clusters are marked with red arrow in the thicker region. (b) HAADF STEM image of thinner FLG region (about 4 monolayers) showing Au_{923} clusters are

monodispersed. (c) Atomic resolution HAADF STEM image of both Au_{923} and Au_{55} clusters in thicker FLG region with a FFT (fast Fourier transform) of the Au_{923} cluster. (d) HAADF STEM image of fragmentation of Au_{55} clusters in thicker FLG region, single atoms are marked with white arrow. Reproduced from reference [1].

To further investigate the interaction of clusters deposited on graphene surface, two different size clusters Au_{55} and Au_{923} are deposited on the same batch of FLG surface. Both Au nanoclusters are produced in the magnetron sputtering cluster source and the sizes are selected by the lateral time-of-flight mass selector with a mass resolution of $M/\Delta M=20$. Deposition energy for both size clusters is 5keV. For Au_{55}, same as before, the deposition energy 5keV is well above the typical pinning energy threshold of Au cluster into graphite. While for Au_{923}, the deposition energy 5keV is equivalent to 5.4eV per atom, which is far below the pinning threshold 13.6eV per atom. Therefore, the Au_{923} clusters deposited on the FLG surface are all expected to remain on the surface while the Au_{55} clusters have sufficient energy to propagate straight through FLG less than 6 monolayers. The FLG deposited with both Au_{55} and Au_{923} clusters are studied in the aberration corrected STEM. Figure 4.3(a) shows a HAADF STEM image taken at a step edge between the thicker and thinner FLG film regions. Same as before, Au_{55} clusters are only observed on the thicker FLG film region that they have penetrated through the thinner FLG film. However, Au_{923} clusters are found both on the thicker and thinner FLG films as their deposition energy is not enough to break even monolayer graphene. The thickness of the FLG film is measured from the integrated HAADF intensity comparing with the mass balance which is the

size selected clusters. The result suggests the FLG film without Au_{55} clusters is only about 3~4 monolayers thick consistent with that Au_{55} clusters are able to penetrate 6 monolayers FLG film at energy of 5keV. Figure 4.3(b) shows the HAADF STEM image of a thinner FLG film region (~4 monolayers) devoid of Au_{55} clusters where the deposited Au_{923} clusters are monodispersed, which indicates the clusters are immobilized by either binding to surface hydrocarbons or trapped by intrinsic defects around to their landing site on the FLG film, at least at room temperature. Therefore, we can conclude that the propagation of Au clusters through graphene is strongly dependent on the cluster size. Secondly clusters soft-landed on the FLG film are not free mobilized as they are trapped locally by binding to surface hydrocarbons or intrinsic defects on the FLG film. Figure 4.3(c) is the surface plot of HAADF STEM image of both Au_{55} and Au_{923} nanoclusters on the relatively thick FLG region showing two Au_{55} clusters are nearby one Au_{923} cluster at the magnification high enough to resolve the atomic structure of Au_{923}, which is decahedral here assigned by comparing with simulated structural isomers. Also individual Au atoms are found around clusters, which we believe are liberated from the clusters. This is confirmed in Figure 4.3(d) where various stages of fragmentation is appeared on all three Au_{55} clusters and liberated individual atoms are marked in the image. The fragmentation of clusters might be caused due to combination of high energy deposition and the high energy electron beam radiation. Even at low beam dose, the cluster structure fluctuates as a function of exposure time, which was reported recently on Au_{55} where the structure is changing under the electron beam and appearing amorphous sometimes, which makes it hard to identify the structure of clusters [46]. However, no metal-mediated etching of graphene is

observed for Au clusters as well as fragments here in the electron microscope although the electron beam can affect cluster fragmentation and structural transition, which is agreed with previous studies that observed on other metals than Au [48].

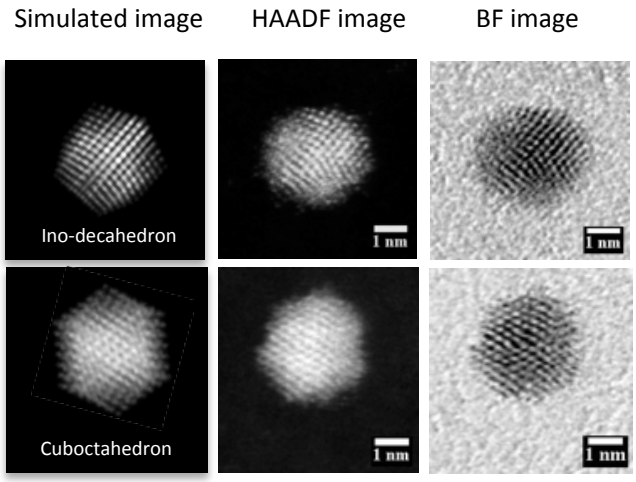

Figure 4.4 HAADF STEM images, BF STEM images and corresponding multislice simulated images of size selected Au_{923} clusters on FLG exhibiting decahedral and cubotahedral structure [46]. Reproduced from reference [1].

Unlike Au_{55} clusters, Au_{923} are relatively stable on the FLG surface with nearly no fragmentations at 5kev deposition energy and under the electron beam that most of them still remain their quasi-spherical shapes, which allows the structure assignments of atomic resolution images. Figure 4.4 are two examples of atomic resolution HAADF STEM image and BF STEM image of Au_{923} clusters compared with the multislice simulated structural isomers. The two structures here are decahedral and cubotahedral (fcc) isomers and the experiment images are comparable with the multislice image simulations of the previous identified structures of Au_{923}. In previous work, size selected Au_{923} are soft-landed on the

amorphous carbon film and the deposition energy is only 0.5eV per atom [49]. In our current work, the deposition energy of Au_{923} is 5.4eV per atom but it doesn't affect or fragment the clusters. The comparison between atomic resolution HAADF STEM image and multislice simulated image has been widely used on the structure identification of many other clusters such as Au_{20} and Au_{55}.

The remaining challenge of this work is the defects on the thinner FLG film region (less then 6 monolayers) induced by Au_{55} penetration are not visualized in our aberration corrected STEM. But we believe it might be achieved in the future by using the low energy aberration corrected HAADF STEM, such as 60keV, to avoid electron beam damage on the FLG film [50].

4.1.4 Conclusion

In summary, in this work the size dependent propagation of highly controlled nanoclusters through FLG have been demonstrated, using the cluster ion beam deposition technique combined with the magnetron sputtering and lateral time-of-flight mass selection. At the same deposition energy, Au_{55} nanoclusters are found to penetrate through the thin FLG film via mechanism of defect generation, while Au_{923} nanoclusters are left on the surface and monodisperse. This work opens the way to use nanolcusters to induce controlled defects on graphene film as well as controlled nanoclusters, which is greatly advantageous for the development of graphene based functional materials.

4.2 Atomic structure control

4.2.1 Overview

Nanoclusters, especially for Au nanoclusters, are reported to attract considerable attentions and be used extensively in many areas such as catalyst, nanoelectronics as well as plasmonics due to their strongly size and structure dependent properties [49-59]. The cluster ion beam deposition technology combined with mass selector, e.g. the lateral time-of-flight mass selector and Quadrapole, enables the controlled production of nanoclusters with specific size, composition, surface coverage and deposition energy and permits the investigation of the size dependent properties of nanoclusters [2-4]. However, even for a specific size nanoclusters exhibit various atomic configurations as previously studied on small gold nanoclusters Au_{20}, Au_{55} and large gold nanoclusters such as Au_{309} and Au_{923} [44-46,49]. The structural control of the nanoclusters down to the atomic level still remains a challenge.

Since the atomic configurations of nanoclusters play important roles on their active sites which is critical for applications such as catalyst, it would be great advantageous to control their isomer populations at the formation stage, which enables the control of the properties of nanoclusters. Here, we are reporting the routine which is able to control the atomic structures of size selected Au nanoclusters during the formation by tuning the parameters in magnetron sputtering gas condensation cluster beam source. This method has been used in the magnetron sputtering cluster source before to transfer the core-shell

composition of Au-Cu bimetallic nanoclusters [60]. In our experiments, size selected Au_{923} nanoclusters are produced in the magnetron sputtering cluster source and during the generation of Au_{923}, parameters such as magnetron power and condensation length have been varied [39]. The prepared Au_{923} nanoclusters are deposited on amorphous carbon TEM grid and are imaged in the aberration corrected STEM to obtain the statistical proportions of isomers with certain populations by comparing HAADF image with multislice simulation of previous identified structures of Au_{923}. We have demonstrated that the decahedral Au_{923} is the dominant proportion over the parameter space and the icosahedral Au_{923} proportion varies monotonically with both magnetron power and condensation length. At specific conditions the icosahedral isomers are eliminated. The results provide the opportunity for the investigation of the properties of nanoclusters not only size dependent but as a function of structures.

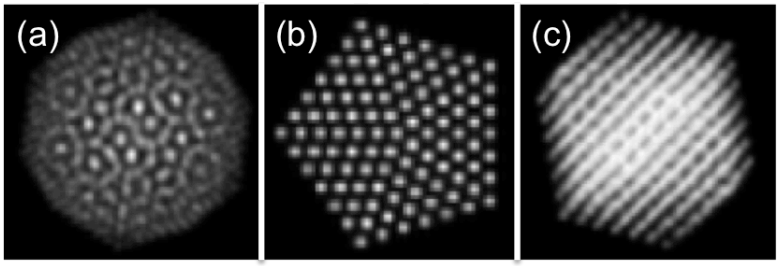

Figure 4.5 Simulated HAADF STEM images biased on the multislice mechanism of Au_{923} clusters exhibiting icosahedral, decahedral and cuboctahedral structures. Simulation results is done by Dr. Z.W. Wang.

4.2.2 Sample preparation

The size-selected Au_{923} nanoclusters are produced in the magnetron sputtering gas condensation cluster beam source, where the nanoclusters are formed by

supersaturated atomic vapor condensed in rare gas atmosphere and the size of the nanoclusters is selected by the inline lateral time-of-flight mass filter using a mass resolution of M/ΔM=20, which is determined by the exit aperture size of the mass filter. Therefore, the size selected Au_{923} nanoclusters actually contain 923±23 atoms [39]. To explore effects of preparation conditions on cluster atomic structure, parameters such as magnetron power, condensation length, Ar and He gas flow and gas pressure in the condensation chamber are varied during the generation of the nanoclusters. All nanoclusters prepared in the magnetron source are soft-landed on the amorphous carbon film TEM grid to retain their free space structures, insofar as possible. The deposition energy used is 1.5keV equivalent to 1.6eV per atom controlled by the bias voltage applied on the sample holder, which is well below the typical pinning energy threshold of Au cluster onto graphite (~14eV per atom) [41]. Clusters are then characterized in the aberration-corrected STEM, JEOL 2100F, equipped with the 200keV electron beam and HAADF detector (62 mrad collection angle). The structure of clusters are assigned by comparing the HAADF images with the multislice simulated HAADF-STEM images from previously identified atomic structures of Au_{923} as shown in Figure 4.5 (The simulation is done by Dr. Z.W. Wang). The statistical proportions of structural isomers at each experimental condition are obtained by the structural analysis of more than 1200 clusters.

The previous identified high symmetry structures of Au_{923} nanocluster are the icosahedral (Ih), decahedral (Dh) and cuboctahedral (fcc) [49]. The structural models of these three high symmetry isomers are shown in Figure 4.6(a-c). The corresponding HAADF STEM images of Au_{923} nanoclusters represent the Ih, Dh

and Fcc structures are shown in Figure 4.6(d-g) and both Ih and Dh structures exhibit the 5-fold symmetry axes just like that in the theoretical models. As reported previously, the Marks truncated decahedron might be found partially among the Dh-Au_{923} nanoclusters, which is shown in Figure 4.6(g), although 923 is not a magic number of the Marks dechahedron. Based on the theoretical models, the HAADF STEM images of these three structural isomers with different orientations are simulated in the QSTEM via the multislice mechanism, as shown in Figure 4.5. The structures of Au_{923} nanoclusters produced experimentally are assigned by the comparison of the lattice patterns with the simulated HAADF STEM images. The Ih-Au_{923} nanoclusters with the unique geometric patterns in HAADF STEM images, such as rings and dots in certain orientation, are easily to be identified. Dh-Au_{923} nanoclusters are recognized owing to their 5-fold symmetry. The Fcc-Au_{923} nanoclusters are face centered cubic usually exhibits straight lines or cross lines across the clusters. But in all cases, there are a number of nanoclusters have amorphous appearance or their structures cannot be assigned to any high symmetry isomers. Regarding to these unidentified nanoclusters, we do not arbitrarily exclude them, instead we designate them into amorphous or unassigned (A/U) besides the high symmetry categories: Ih, Dh and Fcc.

4.2.3 Variation of magnetron power

The magnetron power is varied in the range from 10 to 120W controlled by the power supply connecting to the magnetron head. 120W is nearly the maximum output of the power supply and the 10W is the minimum power for cluster

generation (plasma is hard to be ignited if power is less than 10W). The role of the magnetron power is to control the sputtering yield of the target, which is gold here, to produce supersaturated atomic vapor for cluster formation. The proportions of isomers of nanoclusters observed with certain population are plotted in Figure 4.6(h) as a function of the increasing magnetron power. The initial (lowest magnetron power) and final (highest magnetron power) states of proportions of all four categories are highlighted in Figure 4.6(I). The deposition energy used for the Au_{923} nanoclusters is 1.5keV equivalent to 1.6eV per atom, which is far below the typical pinning energy threshold of Au into graphite (about 14eV per atom). In previously reported studies on structures of Au_{923} nanocluters, the deposition energy used is 0.5eV/atom depositing on amorphous carbon film and 5.4eV/atom depositing on FLG film respectively. As shown in Figure 4.6(h-I), the Dh-Au_{923} isomer is founded to be the most abundant proportion over all different magnetron powers. The proportions of Fcc-Au_{923} and the A/U are not varied significantly across the parameter space. These results are agreed well with the predictions reported by Li et al. stating in spite of the fact that Ih isomer is more favored than Dh or Fcc in small clusters, which contain less than 100 atoms, the Ino-Dh is the most stable structure for large clusters up to 1000 atoms [61]. Experiments by Koga et al. have also shown Au nanoparticles with diameter of 3nm (similar to the size of Au_{923}) are initially icosahedral majored when produced in the gas phase by rapid condensation of atomic vapor but vast majority of them are converted to Dh by thermal annealing [62]. Therefore, in our case for Au_{923} nanoclusters the Dh isomer is more likely to be the most equilibrium structure. In our present results, the proportion of Dh-Au_{923} is observed decreasing monotonically (gradient -0.09, R^2>0.99) with the

increasing magnetron power while the proportion of Ih-Au_{923} raises up (gradient 0.12, R^2=0.99), which reflects the Dh-Au_{923} is competing with the Ih-Au_{923}.

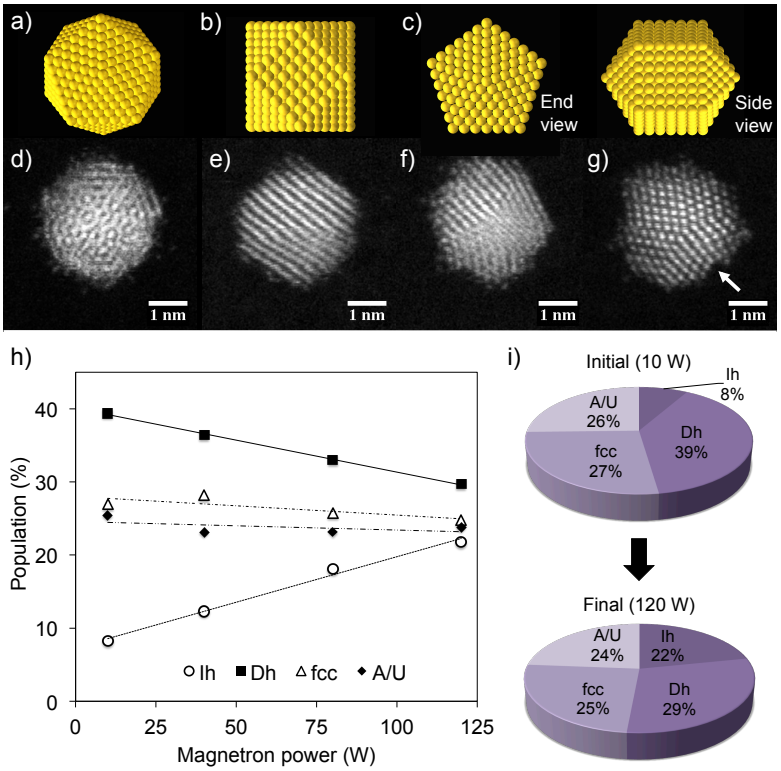

Figure 4.6 (a) Geometry models of icosahedral structure of Au_{923}. (b) Geometry models of cuboctahedral (fcc) structure of Au_{923}. (c) Geometry models of Ino-decahedral structure of Au_{923}. (d) HAADF STEM image of Au_{923} exhibiting icosahedral isomer. (e) HAADF STEM image of Au_{923} showing cuboctahedral isomer. (f) HAADF STEM image of Au_{923} exhibiting decahedral structure. (g) Decahedral Au_{923} clusters exhibiting Marks decahedron. (h) Proportions of Ih, Dh, fcc and A/U isomers within certain population of Au_{923} clusters prepared with different magnetron power. (i) The proportions of the four compositions at the lowest and highest magnetron power. Reproduced from reference [2].

The internal competition between Dh and Ih isomers leads us to consider the nanocluster formation mechanism microscopically down to the atomic level. The results show the Ih isomers are more favored with higher magnetron power where the atomic vapor is more supersaturated. Based on previous studies, the metastable icosahedra observed in large nanoclusters might be attributed to the kinetic trapping effect, where the large Ih nanoclusters grow on top of small Ih nanoclusters, which is just like the seeds through the completion of the out-layer geometry shells [51,62-63]. This is also confirmed in theory by molecular dynamics (MD) simulations, which suggests the icosahedral isomers are dominated in the ideal atom-wise growth, while the coalescence prefers to produce Dh and Fcc isomers [64]. In the magnetron sputtering gas condensation cluster source, the supersaturated atomic vapor is more dense with increasing magnetron power. The higher density of Au atoms leads to more rapid growth of nanoclusters also driving the states of nanoclusters further away from equilibrium. The Fcc structures are possibly determined by the thermodynamic effect, therefore the proportion of Fcc-Au_{923} nanoclusters is less varied across the parameter space.

4.2.4 Variation of condensation length

The condensation length in the magnetron sputtering gas condensation cluster source is the distance between the magnetron head and the nozzle exit of the condensation chamber. The condensation chamber is the inner chamber inside the generation chamber in the cluster source, which is usually hollow and can be cooled by liquid nitrogen. A nozzle is mounted on the end of the condensation

chamber and the aperture size of the nozzle is adjustable (iris) enable to control the gas pressure in the chamber independent to the gas flow. Clusters are formed inside of the condensation chamber by collisions between vaporized atoms and rare gas atoms. The cluster formation process is finished at the nozzle that they are then extracted out of to form the cluster beam. The position of the nozzle is fixed and the condensation length is varied by moving the position of the magnetron head only, which is mounted through a linear motion as shown in Figure 4.7(a).

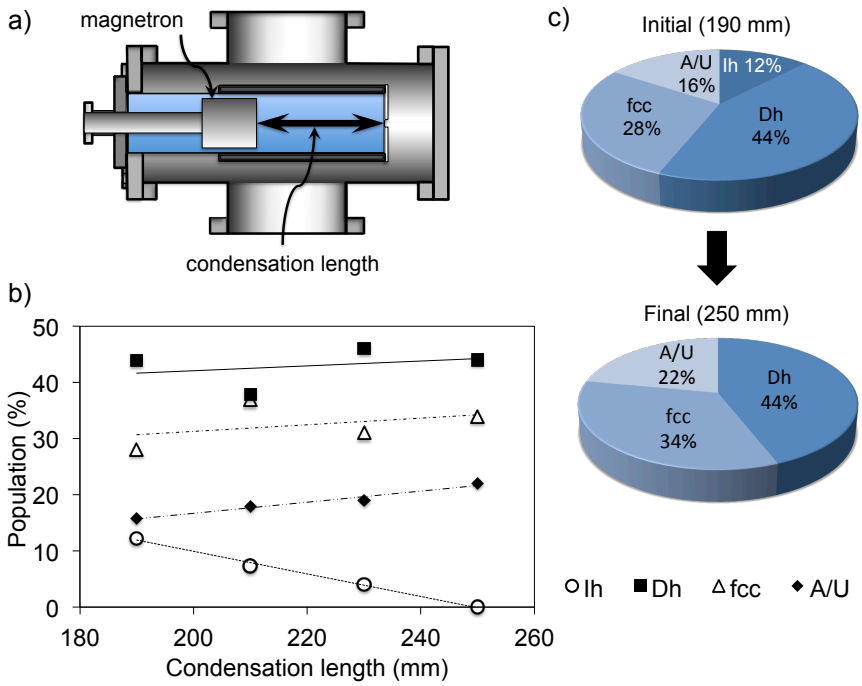

Figure 4.7 (a) Schematic drawing of the condensation chamber inside the cluster generation chamber of the magnetron sputtering cluster source. The condensation length is varied by moving the position of the magnetron head. (b) Proportions of Ih, Dh, fcc and A/U isomers with certain population of Au_{923} clusters prepared with different condensation length. (c) The proportions of the

four compositions at the shortest and longest condensation length. Reproduced from reference [2].

Similar to the different magnetron power, the relative proportions of all three high symmetry isomers, Ih, Dh and Fcc as well as the unidentified category (A/U) within certain populations are plotted as a function of the increasing condensation length from 190 to 250mm as shown in Figure 4.7(b). The magnetron power used here is settled at the lowest 10W. All other parameters remain the same as preparing clusters with different magnetron power in last section, except for there is a difference of 0.04mbar on the pressure of the condensation chamber. This difference might be the reason cause the shifts among the proportions of Ih, Dh and fcc isomers between the two data sets where all other parameters are exactly identical (10W magnetron power and 250mm condensation length in Figure). Similar to the results in the different magnetron power, the Dh-Au_{923} isomers are still the most abundant proportion here near 40% over parameters range, following by the Fcc structures around 30% and the Ih isomers are the least only 10%. The proportions of all four categories at initial (shortest condensation length) and final (longest condensation length) states are highlighted in Figure 4.7(c). As shown in Figure 4.7(b), the Ih-Au_{923} proportion is declined significantly (gradient -0.20, R^2=0.99) as a function of increasing condensation length and the Ih-Au_{923} isomers are completely devoid at the longest condensation length 250mm. However, both Dh isomers and Fcc isomers are increased with the increasing condensation length and the trend indicates there is interplay between each other. With a fixed magnetron power, the average concentration of the atomic vapor inside the

condensation chamber is defined by the volume of the chamber so that it varies as 1/L (L is the condensation length as the volume of the chamber is bounded by the walls and the magnetron head). The mean free path inside the condensation chamber is indeed increased with longer condensation length resulting slower nanocluster growth prior to be extracted out of the condensation chamber through the nozzle. With increasing condensation length, the reaction kinetics move more toward equilibrium and the kinetic trapping effect is reduced. Therefore, higher proportions of equilibrium structures such as Dh and Fcc are observed.

4.2.5 Conclusion

In summary, in this work we combined the atomic resolution HAADF-STEM images with simulated HAADF-STEM image based on multislice mechanism for the assignment of structures of Au_{923} nanoclusters to obtain the statistical proportions of isomers within certain populations as a function of the parameters (magnetron power and condensation length) used during nanocluster generation stage. We have confirmed that the parameters used during the nanoclusters formation have effects on the structures and moreover we have demonstrated that the atomic structures of nanoclusters can be tuned by controlling the formation parameters. The icosahedral isomers have been found to follow a monotonic relationship as a function of both magnetron power and condensation length over the parameters space, which provides us the possibility to eliminate all the icosahedral isomers using specific parameters setting during nanoclusters formation. With parameters setting for the

nonequilibrium conditions, there is found to be a interplay between icosahedral and decahedral isomers which both exhibit the 5-fold symmetry axes, where proportion of icosahedral isomers is favored from sacrifice of the decahedron. This approach we presented here might have the potential to produce nanoclusters which are isomerically pure and that will enable us to explore the properties of nanoclusters not only as a function of size but atomic structural dependence.

List of references

[1] Plant, Simon R., et al. "Size-dependent propagation of Au nanoclusters through few-layer graphene." Nanoscale 6.3 (2014): 1258-1263.

[2] Plant, Simon R., Lu Cao, and Richard E. Palmer. "Atomic structure control of size-selected gold nanoclusters during formation." Journal of the American Chemical Society 136.21 (2014): 7559-7562.

[3] Palmer, R. E., S. Pratontep, and H-G. Boyen. "Nanostructured surfaces from size-selected clusters." *Nature Materials* 2.7 (2003): 443-448.

[4] Bromann, Karsten, et al. "Controlled deposition of size-selected silver nanoclusters." *Science* 274.5289 (1996): 956-958.

[5] Popok, Vladimir N., et al. "Cluster–surface interaction: From soft landing to implantation." *Surface Science Reports* 66.10 (2011): 347-377.

[6] Claridge, Shelley A., et al. "Cluster-assembled materials." *ACS nano* 3.2 (2009): 244-255.

[7] Wang, Hongtao, et al. "Doping monolayer graphene with single atom substitutions." *Nano letters* 12.1 (2011): 141-144.

[8] Wang, Bo, et al. "Size-selected monodisperse nanoclusters on supported graphene: bonding, isomerism, and mobility." *Nano letters* 12.11 (2012): 5907-5912.

[9] Xu, Chao, Xin Wang, and Junwu Zhu. "Graphene– metal particle nanocomposites." *The Journal of Physical Chemistry C* 112.50 (2008): 19841-19845.

[10] Giovannetti, G. A. K. P. A., et al. "Doping graphene with metal contacts." *Physical Review Letters* 101.2 (2008): 026803.

[11] Zan, Recep, et al. "Metal– Graphene Interaction Studied via Atomic Resolution Scanning Transmission Electron Microscope." *Nano letters* 11.3 (2011): 1087-1092.

[12] Zan, Recep, et al. "Evolution of gold nanostructures on graphene." *Small* 7.20 (2011): 2868-2872.

[13] Zan, Recep, et al. "Interaction of metals with suspended graphene observed by transmission electron microscope." *The Journal of Physical Chemistry Letters* 3.7 (2012): 953-958.

[14] Wang, Hongtao, et al. "Interaction between single gold atom and the graphene edge: A study via aberration-corrected transmission electron microscope." *Nanoscale* 4.9 (2012): 2920-2925.

[15] Robertson, Alex W., et al. "Dynamics of single Fe atoms in graphene vacancies." *Nano letters* 13.4 (2013): 1468-1475.

[16] Shan, Changsheng, et al. "Graphene/AuNPs/chitosan nanocomposites film for glucose biosensing." *Biosensors and bioelectronics* 25.5 (2010): 1070-1074.

[17] Guo, Shaojun, et al. "Platinum nanoparticle ensemble-on-graphene hybrid nanosheet: one-pot, rapid synthesis, and used as new electrode material for electrochemical sensing." *Acs Nano* 4.7 (2010): 3959-3968.

[18] Gutés, Albert, et al. "Graphene decoration with metal nanoparticles: Towards easy integration for sensing applications." *Nanoscale* 4.2 (2012): 438-440.

[19] Bunch, J. Scott, et al. "Impermeable atomic membranes from graphene sheets." *Nano letters* 8.8 (2008): 2458-2462.

[20] Jiang, De-en, Valentino R. Cooper, and Sheng Dai. "Porous graphene as the ultimate membrane for gas separation." *Nano letters* 9.12 (2009): 4019-4024.

[21] Koenig, Steven P., et al. "Selective molecular sieving through porous graphene." *Nature nanotechnology* 7.11 (2012): 728-732.

[22] Palmer, R. E., A. P. G. Robinson, and Q. Guo. "How Nanoscience Translates into Technology: The Case of Self-Assembled Monolayers, Electron-Beam Writing, and Carbon Nanomembranes." *ACS nano* 7.8 (2013): 6416-6421.

[23] Russo, Christopher J., and J. A. Golovchenko. "Atom-by-atom nucleation and growth of graphene nanopores." *Proceedings of the National Academy of Sciences* 109.16 (2012): 5953-5957.

[24] Carroll, S. J., et al. "The impact of size-selected Ag clusters on graphite: an STM study." *Journal of Physics: Condensed Matter* 8.41 (1996): L617.

[25] Carroll, S. J., et al. "Energetic impact of size-selected metal cluster ions on graphite." *Physical review letters* 81.17 (1998): 3715.

[26] Carroll, S. J., et al. "Deposition and diffusion of size-selected (Ag400+) clusters on a stepped graphite surface." *Applied Physics A* 67.6 (1998): 613-619.

[27] Carroll, S. J., K. Seeger, and R. E. Palmer. "Trapping of size-selected Ag clusters at surface steps." *Applied physics letters* 72.3 (1998): 305-307.

[28] Carroll, S. J., et al. "Pinning of size-selected Ag clusters on graphite surfaces." *The Journal of Chemical Physics* 113.18 (2000): 7723-7727.

[29] Couillard, M., S. Pratontep, and R. E. Palmer. "Metastable ordered arrays of size-selected Ag clusters on graphite." *Applied physics letters* 82 (2003): 2595.

[30] Carroll, S. J., et al. "Shallow implantation of “size-selected” Ag clusters into graphite." *Physical review letters* 84.12 (2000): 2654.

[31] Kenny, D. J., et al. "Measuring the implantation depth of silver clusters in graphite." *The European Physical Journal D-Atomic, Molecular, Optical and Plasma Physics* 16.1 (2001): 115-118.

[32] Kenny, D. J., et al. "Implantation depth of size-selected silver clusters into graphite." *Journal of Physics: Condensed Matter* 14.8 (2002): L185.

[33] Sanz-Navarro, C. F., et al. "Scaling behavior of the penetration depth of energetic silver clusters in graphite." *Physical Review B* 65.16 (2002): 165420.

[34] Pratontep, S., et al. "Scaling relations for implantation of size-selected Au, Ag, and Si clusters into graphite." *Physical review letters* 90.5 (2003): 055503.

[35] Seminara, L., et al. "Implantation of size-selected silver clusters into graphite." *The European Physical Journal D-Atomic, Molecular, Optical and Plasma Physics* 29.1 (2004): 49-56.

[36] Claeyssens, F., et al. "Immobilization of large size-selected silver clusters on graphite." *Nanotechnology* 17.3 (2006): 805.

[37] Goldby, I. M., et al. "Gas condensation source for production and deposition of size-selected metal clusters." *Review of scientific instruments* 68.9 (1997): 3327-3334.

[38] Pratontep, S., et al. "Size-selected cluster beam source based on radio frequency magnetron plasma sputtering and gas condensation." *Review of scientific instruments* 76.4 (2005): 045103.

[39] Von Issendorff, B., and R. E. Palmer. "A new high transmission infinite range mass selector for cluster and nanoparticle beams." *Review of Scientific Instruments* 70.12 (1999): 4497-4501.

[40] Asari, E., et al. "Thermal relaxation of ion-irradiation damage in graphite." *Physical Review B* 47.17 (1993): 11143.

[41] Di Vece, Marcel, S. Palomba, and R. E. Palmer. "Pinning of size-selected gold and nickel nanoclusters on graphite." *Physical Review B* 72.7 (2005): 073407.

[42] Smith, Roger, et al. "Modeling the pinning of Au and Ni clusters on graphite." *Physical Review B* 73.12 (2006): 125429.

[43] Young, N. P., et al. "Weighing supported nanoparticles: size-selected clusters as mass standards in nanometrology." *Physical review letters* 101.24 (2008): 246103.

[44] Wang, Z. W., et al. "Counting the atoms in supported, monolayer-protected gold clusters." *Journal of the American Chemical Society* 132.9 (2010): 2854-2855.

[45] Wang, Z. W., and R. E. Palmer. "Intensity calibration and atomic imaging of size-selected Au and Pd clusters in aberration-corrected HAADF-STEM." *Journal of Physics: Conference Series*. Vol. 371. No. 1. IOP Publishing, 2012.

[46] Wang, Z. W., and R. E. Palmer. "Experimental evidence for fluctuating, chiral-type Au55 clusters by direct atomic imaging." *Nano letters* 12.11 (2012): 5510-5514.

[47] Cheng, Hai-Ping, and Uzi Landman. "Controlled deposition, soft landing, and glass formation in nanocluster-surface collisions." *Science* 260.5112 (1993): 1304-1307.

[48] Ramasse, Quentin M., et al. "Direct experimental evidence of metal-mediated etching of suspended graphene." *ACS nano* 6.5 (2012): 4063-4071.

[49] Wang, Z. W., and R. E. Palmer. "Determination of the ground-state atomic structures of size-selected Au nanoclusters by electron-beam-induced transformation." *Physical review letters* 108.24 (2012): 245502.

[50] Ramasse, Quentin M., et al. "Direct experimental evidence of metal-mediated etching of suspended graphene." *ACS nano* 6.5 (2012): 4063-4071.

[51] Baletto, Francesca, and Riccardo Ferrando. "Structural properties of nanoclusters: Energetic, thermodynamic, and kinetic effects." *Reviews of modern physics* 77.1 (2005): 371.

[52] Barnard, A. S. "Modelling of nanoparticles: approaches to morphology and evolution." *Reports on Progress in Physics* 73.8 (2010): 086502.

[53] Barnard, Amanda S., et al. "Nanogold: a quantitative phase map." *ACS nano* 3.6 (2009): 1431-1436.

[54] Barnard, Amanda S. "Direct comparison of kinetic and thermodynamic influences on gold nanomorphology." *Accounts of chemical research* 45.10 (2012): 1688-1697.

[55] Sanchez, A., et al. "When gold is not noble: nanoscale gold catalysts." *The Journal of Physical Chemistry A* 103.48 (1999): 9573-9578.

[56] Boyen, H-G., et al. "Oxidation-resistant gold-55 clusters." *Science* 297.5586 (2002): 1533-1536.

[57] Harding, Chris, et al. "Control and manipulation of gold nanocatalysis: effects of metal oxide support thickness and composition." *Journal of the American Chemical Society* 131.2 (2008): 538-548.

[58] Maier, Stefan A., et al. "Plasmonics—a route to nanoscale optical devices." *Advanced Materials* 13.19 (2001): 1501-1505.

[59] Wu, Yue, et al. "Controlled growth and structures of molecular-scale silicon nanowires." *Nano Letters* 4.3 (2004): 433-436.

[60] Yin, Feng, Zhi Wei Wang, and Richard E. Palmer. "Controlled formation of mass-selected Cu–Au core–shell cluster beams." *Journal of the American Chemical Society* 133.27 (2011): 10325-10327.

[61] Li, Z. Y., et al. "Three-dimensional atomic-scale structure of size-selected gold nanoclusters." *Nature* 451.7174 (2008): 46-48.

[62] Koga, Kenji, Tamio Ikeshoji, and Ko-ichi Sugawara. "Size-and temperature-dependent structural transitions in gold nanoparticles." *Physical review letters* 92.11 (2004): 115507.

[63] Baletto, F., C. Mottet, and R. Ferrando. "Microscopic mechanisms of the growth of metastable silver icosahedra." *Physical Review B* 63.15 (2001): 155408.

[64] Grochola, Gregory, Salvy P. Russo, and Ian K. Snook. "On morphologies of gold nanoparticles grown from molecular dynamics simulation." *The Journal of chemical physics* 126.16 (2007): 164707.

Chapter 5 Proof-of-principle demonstration of the Matrix Assembly Cluster Source (MACS)

In recent years, state-of-the-art cluster beam technology has allowed a range of fundamental studies to be carried out, an example being the demonstration of size-selected clusters as model catalysts. Taking the magnetron cluster source as an example, such developments have been possible through improved control (e.g. cluster formation parameters) and high transmission efficiency through the mass filter. However, even with such developments, althrough the flux rate is sufficient for fundamental studies such as catalytic property demonstration, it is still far behind the demand for chemical tests and industrial applications [1]. This chapter presents the concept idea and demonstration experiments for a new technology for the production of clusters, the matrix assembly cluster source (MACS), also includes the preliminary studies of matrix parameters on cluster size and flux. The scale-up of production rate and systematical investigation of matrix parameters will be discussed in Chapter 6.

The work presented in this chapter was under supervision of Prof. Richard Palmer and co-supervisor Dr. Feng Yin. The idea of the MACS was come up by Prof. Richard Palmer. The instrument development and sample preparation were done together by the author and Dr. Feng Yin. Sample characterization using STEM and data interpretation were done by the author.

5.1 Introduction of the MACS

5.1.1 Overview

The matrix assembly cluster source seeks to generate clusters via a completely new approach. The idea is to assemble the clusters through the ion beam bombardment of a matrix, which is formed by cryogenically condensed (solid) inert gas loaded with metal atoms. In our work, the matrix is formed cryogenically by condensing atomic vapor of the desired cluster material such as Ag or Au, and rare gas atoms such as Ar simultaneously onto a matrix condensation support, which is cooled using liquid helium (to below 20K). Clusters are then produced by high energy Ar ion beam sputtering the matrix.

5.1.2 Transmission and reflection mode

In the MACS, clusters can be produced both in transmission and reflection regimes dependent on the matrix condensation support employed. The matrix condensation support is a sheet of high-density holey membrane (a grid or mesh) for transmission mode. Copper mesh TEM grids, quantifoil or large copper

mesh sheet were all investigated for use as the matrix support. In transmission mode, the matrix forms as an adlayer on the bars of each mesh and is more likely to close the hole when it is small enough (e.g. quantifoil). The matrix with cluster atoms embeded in solid rare gas is then sputtered by high-energy Ar ions (above 1keV). Clusters are produced during the sputtering in transmission regime, as shown in Figure 5.1 (a).

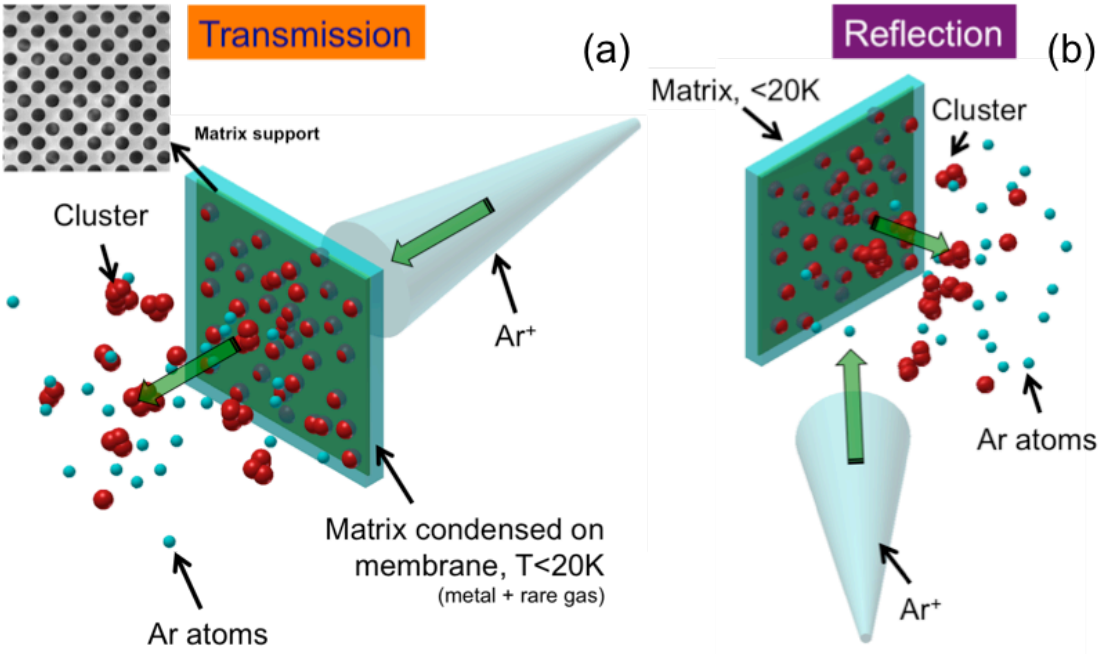

Figure 5.1 Schematic diagram of (a) transmission and (b) reflection modes in Matrix Assembly Cluster Source (MACS). The matrix is formed by vaporizing cluster material atoms (eg. Ag or Au) and rare gas atoms (eg. Ar) condensed onto the matrix condensation grid (less than 20K) at the same time. Clusters are produced by high energy Ar ions sputtering the matrix.

For the reflection mode, the matrix condensation support is replaced by a solid plate, for example, a piece of copper sheet, instead of holey membrane. The orientation of the matrix support is in an angle, usually from 10° to 45° to the

direction of incident ion beam. Clusters are produced following the same procedure just described but collected in reflection regime as shown in Figure 5.1(b). In this chapter, only transmission mode is used to demonstrate the principle of the MACS as well as preliminary study of effects of matrix parameters. Reflection mode will be discussed in chapter 6.

5.1.3 Methodology

The production of clusters in the MACS is based on a high-energy (>1keV) atomic (e.g. Ar^+) ion beam bombarding a condensed matrix of rare gas atoms. The matrix is Ar impregnated with atoms of desired cluster materials, including Ag or Au. The cluster formation process is possible through two mechanisms:

(i) Clusters are preformed during the condensation of the matrix. The matrix is formed by simultaneously condensing of atoms cluster materials and rare gas. In the matrix, cluster material atoms are driven into small clusters by the potential force to minimize the energy [2-5]. This process happens as soon as the cluster material atoms land in the matrix and only lasts around 20ps.

(ii) Clusters are aggregated through the ion impact. Due to the momentum delivered into matrix with high-energy ion impact, small clusters and cluster material atoms inside the matrix become mobile and aggregate into bigger clusters. Clusters keep growing with multiple ion impacts because of successively delivered momentum and the depletion of rare gas atoms [6-8].

The clusters produced in the MACS are formed with the combination of (i) and (ii) and they are emitted out of the matrix through the collision cascade and thermal spike [9-13]. For the collision cascade, sequence of recoils are generated in the sample after the original impact, as shown in Figure 5.2(a). Thermal spike happens when the incoming ion is heavy and energetic where the collisions between ions are not independent, instead they are considered to be many body collisions, as shown in Figure 5.2(b). The clusters produced initially might be a mixture of cluster atoms and rare gas. However, rare gas atoms will later evaporate off while metal atoms will not. The size of clusters depends on several parameters such as metal concentration in the matrix, matrix temperature, incident beam energy and details will be discussed in the results section in chapter 5 and chapter 6.

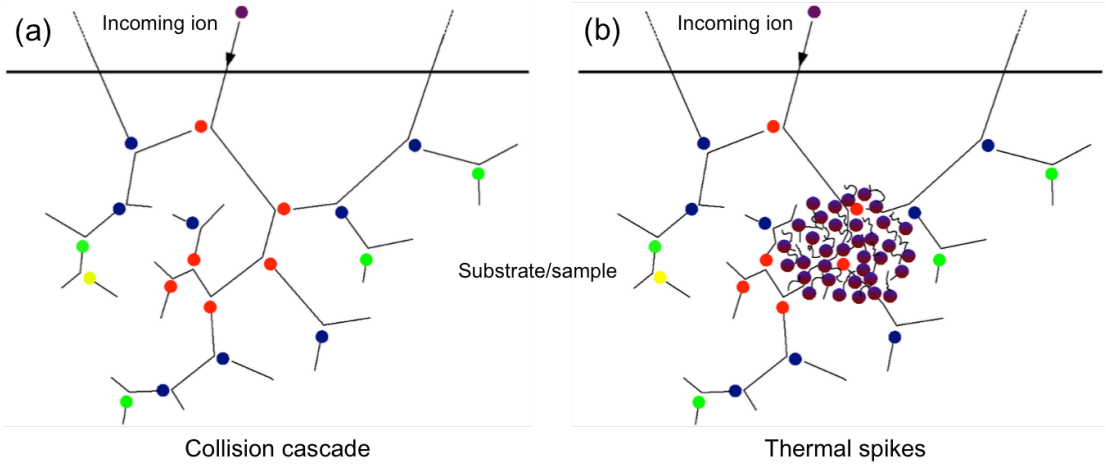

Figure 5.2 Schematic diagrams illustrating collision cascade (a) and thermal spikes (b). Reproduced from reference [14]

5.1.4 Promising features and Potential of scaling-up

Based on the results obtained so far, the clusters produced using the MACS techniques exhibit a "narrow" size distribution ($M/\Delta M>1$) without mass selection. Moreover, the size of clusters can be controlled by the experimental parameters primarily the metal concentration in the matrix. These two features enable the production of size-selected clusters, e.g. for catalysis purpose, using the MACS techniques without additional mass selection, which results in a higher-usage ratio of the clusters. The aim of the MACS technology is to scale up the cluster production rate by ~7 order of magnitude, from 0.1-1nA to 1-10mA, which is equivalent to grams of clusters per day. In principle, the cluster production rate in the MACS is a function of the incident ion beam current, and ion beam sources with output current up to 10A are available. The ion to cluster ratio (how many incident ions are required to produce one cluster) based on our current experimental results is 0.05% for transmission mode and nearly 0.5% for reflection mode. Therefore, a cluster beam current equivalent to 10mA is achievable. Of course the precondition is the matrix has a sufficient replenishment rate.

This chapter concentrates on the proof-of-principle of the MACS idea and preliminary studies of effect of experimental parameters on cluster production using MACS demonstration apparatus. In chapter 6, we report the development of the upgraded apparatus, MACS 1, to scale up the cluster production rate and systematically investigate the controlled cluster production to better understand the methodologies.

5.2 MACS demonstration apparatus

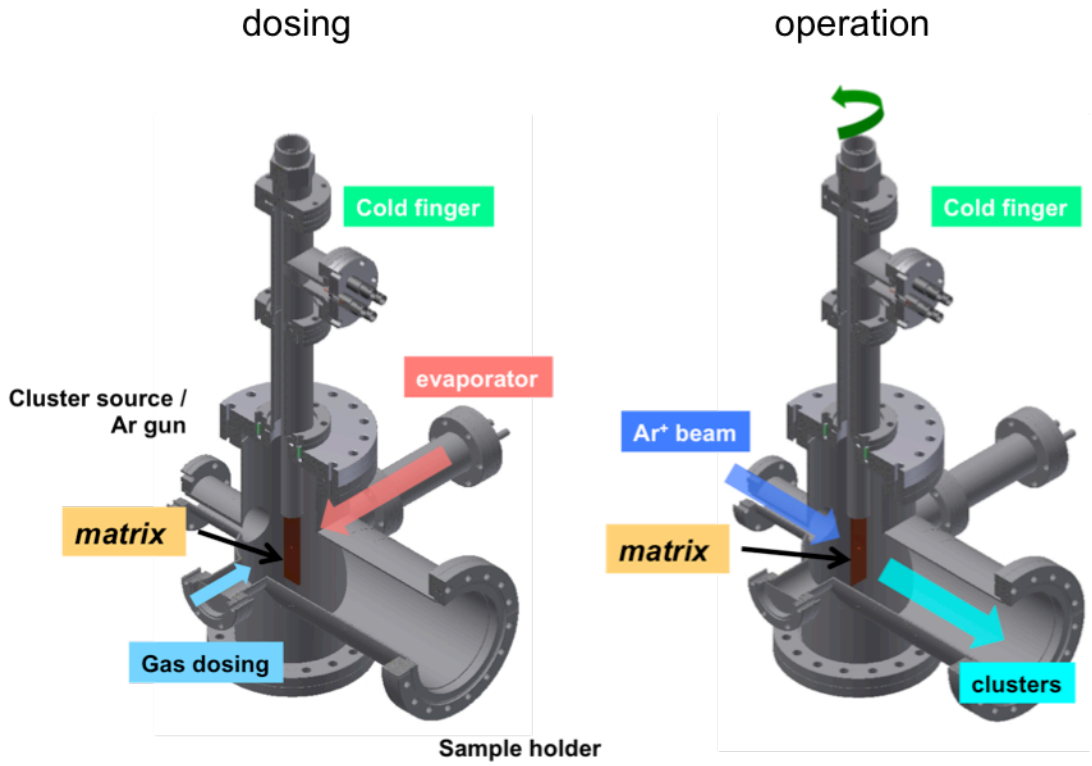

Figure 5.2 Schematic diagrams of MACS demonstration apparatus. The matrix condensation grid is mounted on a rotatable cold finger on top of the chamber. The matrix condensation grid is faced to the evaporator first for matrix condensation then rotated to face the ion beam for cluster production.

In the MACS demonstration system, clusters are only produced in transmission mode. As shown in Figure 5.3, the principle demonstration experiments were carried out in a six way cross chamber containing three DN100CF flange ports and three DN35CF ports, as show in Figure 5.2. The matrix condensation grid is clamped on the head of cold finger mounted on the top DN100CF flange through a rotary drive so rotentional orientation of the matrix support can be changed. A leak valve is mounted on the side DN35CF flange for gas dosing and the gas

dosing rate is monitored by the Penning gauge. The evaporator is mounted on the other side for cluster materials vaporization. The whole chamber is connected to a magnetron sputtering cluster source as the Ar ion beam used to sputter the matrix is generated in the cluster source at the early stage. A sample holder containing 6 TEM grids is mounted on the back DN100CF flange port in line with Ar beam and matrix to collect produced clusters.

5.2.1 Matrix condensation support

Several different types of grids for matrix condensation were tested in the demonstration experiments, in order to study the effects on cluster size and flux. The grid types includes 400, 1000, 2000 mesh copper grid and quantifoil (15-20nm carbon film with array of same size holes). All of them are 3 mm in diameter. The specifications for each grid are summarized in Table 5.1.

Matrix support grid type	Hole width/diameter	Bar width/diameter	Transmission ratio
400 mesh	37μm	25 μm	37%
1000 mesh	19 μm	6 μm	57%
2000 mesh	6.5 μm	6 μm	41%
Quantifoil 1.2/1.3	1.2 μm	1.3 μm	11%

Table 5.1 Specification of different type matrix condensation grid.

5.2.2 Cryogenic cooling

The cold finger used in the principle demonstration system is made of a hollow stainless steel tube with an oxygen-free copper block welded on the top to hold the matrix support. The matrix support is clamped on the copper part and is electrically isolated from the whole cold finger using a sapphire plate. This

arrangement allows for a bias voltage to be applied to the matrix support and current of the incident ion beam to be measured. The incident beam current on the matrix support is read by the Keithley 6485 picoammeter. To maintain the good thermal conductivity, the sapphire was coated with gold on both sides using Edwards commercial evaporator. The cooling is provided by injecting liquid helium flow from Dewar bottle directly deliver to the copper part of cold finger through a transfer line. An oil free scroll pump is used to maintain the flow by pumping helium gas out. The cooling power can be controlled by adjusting the regulator in the pumping line.

5.2.3 Temperature measurement

The temperature of the matrix support can be cooled to below 20K in ~1.5 hours and the lowest temperature recorded was 9K. The temperature of the matrix condensation support is measured using the Rhodium-Iron temperature sensor mounted on top of the cold finger just beside the matrix condensation support. The Lakeshore 340 temperature controller is used to monitor the temperature. The calibration curve for the temperature sensor has been calibrated at 3 points, ice water, liquid nitrogen and liquid helium, to achieve accuracy measurement.

5.2.4 Evaporation

A thermal evaporator is used to vaporize cluster material in the demonstration system. The cluster material (e.g. Au and Ag) is filled in a Tantalum boat and the boat is heated up by high DC current. A quartz crystal microbalance (QCM, from

Digi-key ATS060, 6MHz) is mounted in front of the evaporator to monitor the evaporation speed. The evaporation speed is monitored by reading the frequency of the QCM using the thin film rate/thickness transducer from Sycon instruments. In order to determine the correct evaporation speed on the matrix, another QCM is mounted on the cold finger temperately, at the same position as the matrix support, for calibration before carrying out cluster production. The QCM on the cold finger is removed when preparing clusters as it will affect the cooling of the matrix condensation support. Five different evaporation speeds have been tested for the calibration and the real evaporation speed on the matrix is approximately 5 times less than the reading from QCM in front of evaporator. Details are shown in Table 5.2.

QCM in front of evaporator	QCM at position of matrix condensation grid
0.3Å/s	0.05Å/s
0.6Å/s	0.11Å/s
1Å/s	0.18Å/s
1.2Å/s	0.25Å/s
2Å/s	0.36Å/s

Table 5.2 Evaporation speed measured by QCM mounted in front evaporator and on the position same as the matrix condensation grid.

To provide additional verification of the evaporation rate, we also measured the thickness of metal deposited to a silicon wafer mounted at same position as the matrix condensation grid comparing to the QCM value. A 400 mesh TEM grid is attached to the silicon wafer as the mask to create patterns. The height of Ag film

thickness on silicon wafer is measured in AFM comparing with the thickness read from QCM. More than three patterns are measured, as shown in Figure 5.6. The average height is 62nm which is just about 5 times less than the reading form QCM in front of evaporator, 300nm.

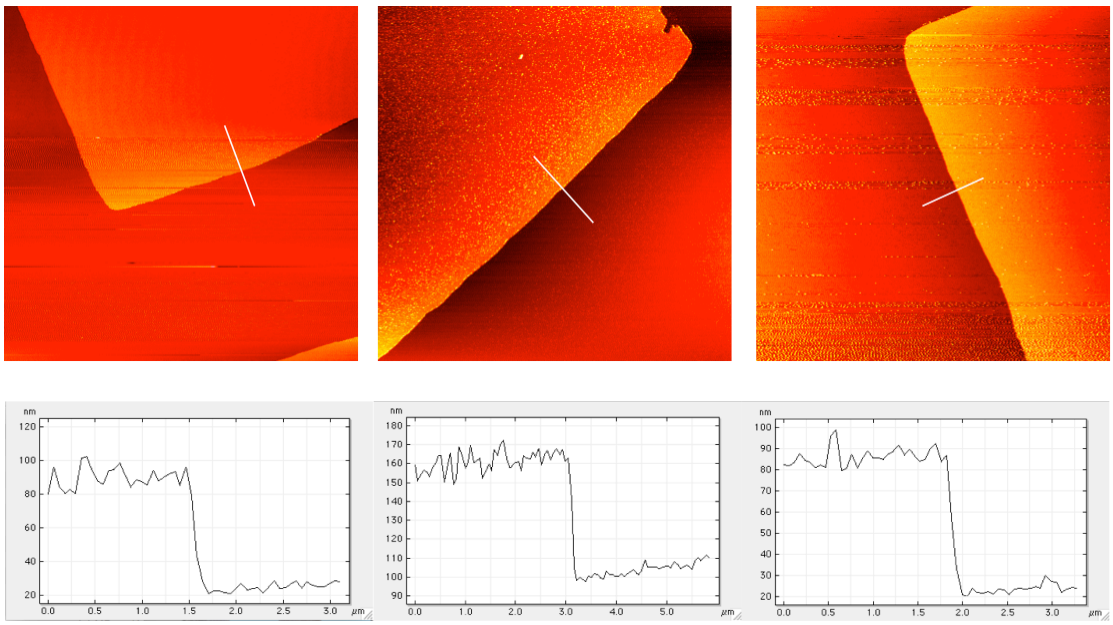

Figure 5.6 Top row: AFM images of evaporation patterns on a silicon wafer mounted at the same position as the matrix condensation grid. Bottom row: line profiles across the edge of patterns.

5.2.5 Gas dosing

Gas dosing in the MACS principle demonstration apparatus is through a leak valve and the gas dosing rate is monitored using a Penning gauge (range from 10^{-8} to 10^{-2} mbar) mounted on the side of the chamber. No local dosing is used in the experiments and gas is filled in the whole chamber with a dosing pressure

between 10^{-7} and 10^{-6} mbar when preparing clusters. The matrix formation gas used is Ar here and the base pressure in the chamber is 10^{-8} mbar.

5.2.6 Ar ion beam

Two different Ar^+ ion beam sources are used in the principle demonstration experiments: Ar^+ ion beam from magnetron sputtering source and Ar ion gun for scale-up the cluster flux. When using the Ar^+ ion beam from magnetron sputtering cluster source, the cluster generation chamber is connected to the exit of ToF mass filter of the magnetron sputtering cluster source. The Ar ion beam is generated in the magnetron sputtering cluster source and filtered out by the ToF mass filter to avoid any metal ions produced by sputtering. As mentioned previously, in the magnetron sputtering cluster source the Ar plasma is ignited by the potential applied on the magnetron head, powered by either DC power supply or RF power supply. The Ar plasma formed in the generation chamber is then extracted and focused into a beam by electrical fields applied on a set of ion optics. Finally the Ar ion beam is filtered out by the ToF mass filter and delivered to the MACS chamber through another set of ion optic lenses [15-16]. The energy of Ar beam generated from magnetron sputtering cluster source is defined by the potential applied on the terminal plate, which is the matrix here. In most cases the bias voltage on the cold finger is -950V meaning the energy of Ar ion beam hitting the matrix is 950eV. The maximum voltage we are able to apply on the cold finger is ±3000V. The spot size of Ar ion beam is around 5mm in diameter and maximum current detected on cold finger can be up to 10nA at 950V bias voltage.

The Ar ion gun used is a cold cathode ion source ISE 5 from Omicron, which is able to generate a maximum ion beam current of 80μA with beam energy from 250eV to 5keV. The Ar ion beam generated in this ion source is via the mechanism of gas discharge between cathode and anode in a gas cell when a high voltage is applied. The gas discharge region is surrounded by a longitudinal magnetic field forcing electrons to spiral which extends the path to generate a large quantity of ions and electrons. The ions generated inside gas cell are then extracted through an aperture on the kinetic plate into flight tube. The energy of the Ar beam generated in Ar ion gun can be controlled by tuning the voltage difference between the kinetic plate and flight tube. Also an electrical ion optic lens is mounted in the front of the flight tube of the ion source to control the spot size of out coming ion beam. The incident Ar ion beam current on the cold finger is measured by the picoammeter, Keithley 6485. The picoammeter is floated and a circuit (based on Keithley manual) is built connecting to the picoammeter enabling to apply bias voltage on the cold finger while measuring the current. The picoammeter is biased at the same potential as the cold finger, and in order to isolate the picoammeter from the operator and other equipment it is enclosed in insulating box.

5.3 Sample preparation

Samples were produced to demonstrate the principle of the matrix assembly cluster source, as well as study effects of different parameters on cluster size and flux. The sample preparation procedures can be divided into the following steps.

(a) Preparation work

The chamber is pumped down to below $5x10^{-8}$ mbar before starting the experiments, which is almost the best vacuum that can be achieved at room temperature without baking the system. The evaporator is degassed by heating up to above 600°C for 30mins. Ar ion beam is optimized to reach the certain beam current on cold finger. For Ar ion beam from cluster source, the beam current is optimized by tuning the gas flow, voltages on nozzle, skimmers and ion optic lenses. For the Ar ion gun, the beam current can be tuned just on the front panel on the controller to set beam energy, emission current as well as focus. After preparation of the incident Ar ion beam, the cold finger is cooled down by liquid helium to below 20K. The pressure of the chamber reaches to 10^{-9} mbar after cooling as the cooled cold finger is working as a cryogenic pump.

(b) Condensation of the matrix

The matrix condensation support is rotated to face the evaporator for matrix condensation. The evaporator is heated up to achieve a stable evaporation flux measured by the QCM in front of the evaporator, before opening the shutter. The evaporation and gas dosing start simultaneously. Gas dosing rate on the matrix is controlled by the gas pressure monitored by the penning gauge. The matrix growth time is recorded by a stop watch.

(c) Deposition of clusters

After the matrix condensation, the cold finger is rotated back in line with ion beam and sample holder. Similar to that in magnetron source, the sample holder is biased by high voltage power supply and connected to ground through the

picoammeter to avoid charging effect. The bias voltage is applied to both the cold finger and sample holder in order to control the incident beam energy and create a free-flight region between the matrix and sample. The incident Ar ion beam is then switched on to bombard the matrix that clusters are produced in transmission regime and deposited on sample holder. The incident beam current is monitored both on cold finger and sample holder by the picoammeter.

5.4 Results and discussion

5.5.1 Demonstration of cluster production in MACS

The proof-of-principle of the MACS was demonstrated by successful production of Ag and Au clusters. Figure 5.7 are the HAADF STEM images of silver clusters and gold clusters produced using the MACS demonstration apparatus. Gold clusters are much brighter than the silver clusters because of Au has a large atomic value.

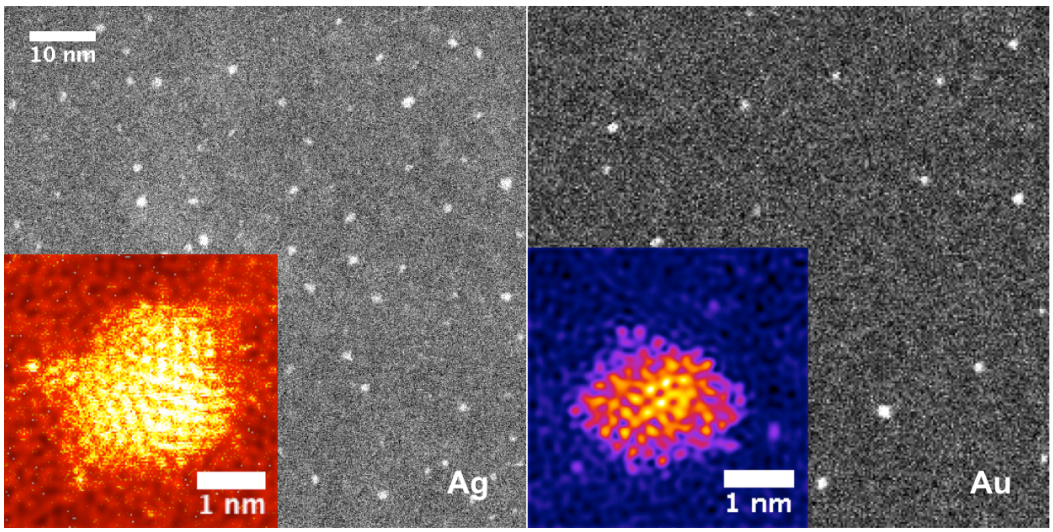

Figure 5.7 HAADF STEM images of Ag (left) and Au (right) clusters produced in MACS. Related parameters: matrix condensation support, 400 mesh grid; matrix temperature, 13K, gas dosing pressure, $3x10^{-6}$ mbar; matrix condensation time, 200s; metal concentration in the matrix, 1.1%; matrix thickness, ~85nm; incident Ar beam current, 10nA; incident beam energy, 950eV; deposition time, 120s.

5.5.2 Size distribution

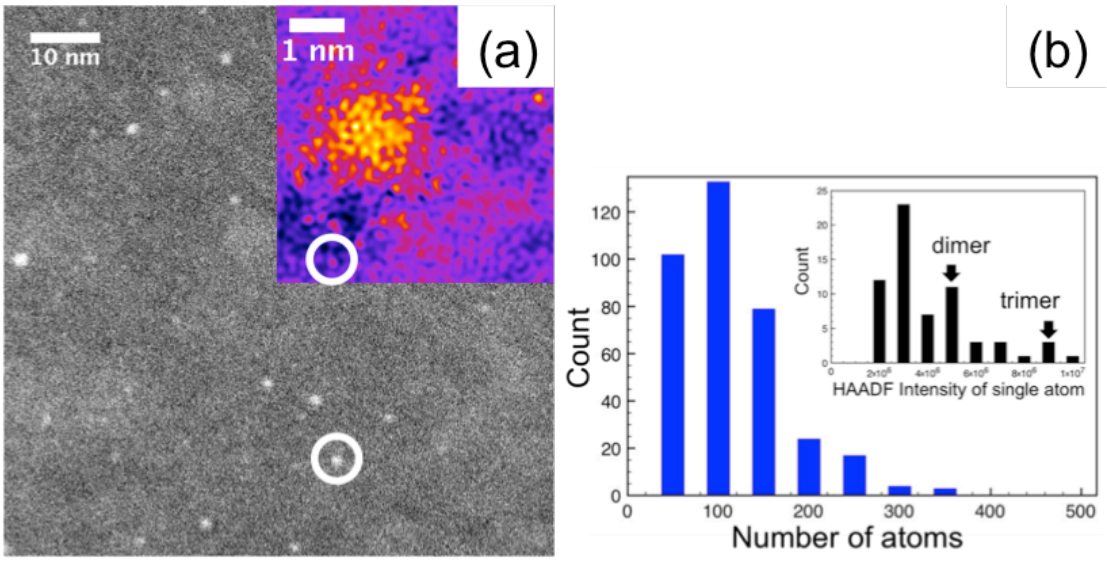

Figure 5.8 (a) HAADF STEM image and atomic resolution image of Ag clusters produced in MACS. (b) Size distribution of the clusters and the HAADF intensity distribution of single atoms. The size of clusters is measured from the HAADF intensity of clusters comparing with mass balance which is single atoms. Related parameters: matrix condensation support, 400 mesh grid; matrix temperature, 12K, gas dosing pressure, $3x10^{-6}$ mbar; matrix condensation time, 200s; metal concentration in the matrix, 1.1%; matrix thickness, ~85nm; incident Ar beam current, 10nA; incident beam energy, 950eV; deposition time, 60s.

Figure 5.8(a) shows the HAADF STEM image and atomic resolution image of Ag clusters produced in the MACS demonstration apparatus. The size of clusters is measured from the HAADF intensity of clusters comparing with the mass balance, which is single atoms. The size distribution of the clusters and the HAADF intensity distribution of single atoms are shown in Figure 5.8(b). From the size distribution, most clusters in this sample contain about 100-150 atoms and the largest clusters found only contain 350 atoms. The full width at half maximum of the size distribution is about 100 atoms, which give a mass resolution, $m/\Delta m \sim 1$. The result indicates the clusters produced by the MACS at certain experimental conditions have a relatively narrow size distribution.

5.5.3 Flux of clusters

The flux of clusters is estimated from the density of clusters deposited on the substrate as not all clusters are positively charged and current detected on the sample holder is also contributed by Ar ion beam and secondary electrons. The cluster density is therefore measured from the HAADF STEM images in order to get total number of clusters on the sample then divided into the deposition time to determine the cluster flux. For the sample deposited with Ag clusters shown in Figure 5.8(a) has a cluster density of 5300 clusters/μm^2 with deposition time of 60s and cluster production area of 3mm in diameter. Therefore the cluster flux is 6.08×10^8/s using the equation below.

$$cluster\ flux = \frac{cluster\ density \times production\ area}{deposition\ time}$$

5.5.4 Size control

In addition to the clusters produced in MACS has relatively narrow size distribution, m/Δm~1, the cluster size can be controlled by tuning the parameters especially the metal concentration in the matrix. In this work, the metal concentration in the matrix is determined only by the evaporation speed as the gas dosing rate is fixed. HAADF STEM images and atomic resolution images of eight samples prepared with metal concentration from 0.38% to 5.66% are shown in Figure 5.9 (a-h) as well as the histograms of size distribution measured from the integrated HAADF intensity in (i-p). A plot of cluster size and calculated cluster flux as a function of metal concentration in the matrix is shown in Figure 5.10.

As shown in the plot, it is clear that the size of clusters produced by the MACS is increased significantly, with a power of 2, with the metal concentration in the matrix. However, the flux of clusters decreases rapidly with a power of 2.5. The size distributions of clusters produced remain relatively narrow, m/Δm~1, across the parameter space.

As mentioned in the methodology section, cluster formation process is probably through two mechanisms. For both routines, with higher metal concentration in the matrix, clusters more easily capture other atoms to grow larger due to the higher density of cluster material atoms. The decrease in the cluster flux is due to the fact that a matrix with a heavier metal loading matrix is harder to sputter and larger clusters are relatively harder to be knocked out the matrix [19-23].

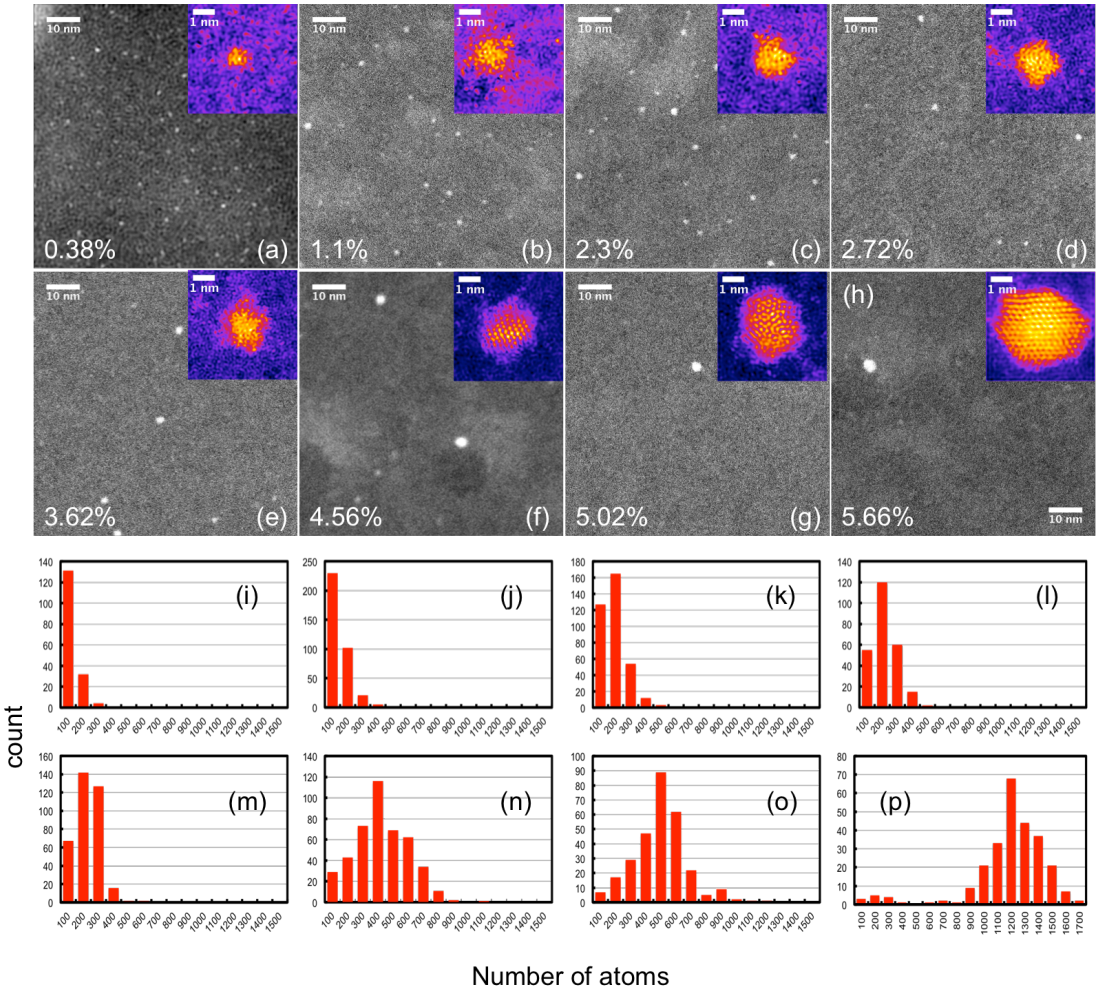

Figure 5.9 (a-h) HAADF STEM images and atomic resolution images of clusters prepared with different metal concentration in the matrix from 0.38% to 5.66%. (i-p) Histograms of size distributions of clusters prepared with different metal concentrations. The size of clusters is measured from the integrated HAADF intensity. Related parameters: matrix condensation support, 400 mesh grid; matrix temperature, 12K, gas dosing pressure, $3x10^{-6}$ mbar; matrix condensation time, 200s; matrix thickness, ~85nm; incident Ar beam current, 10nA; incident beam energy, 950eV; deposition time, 60s.

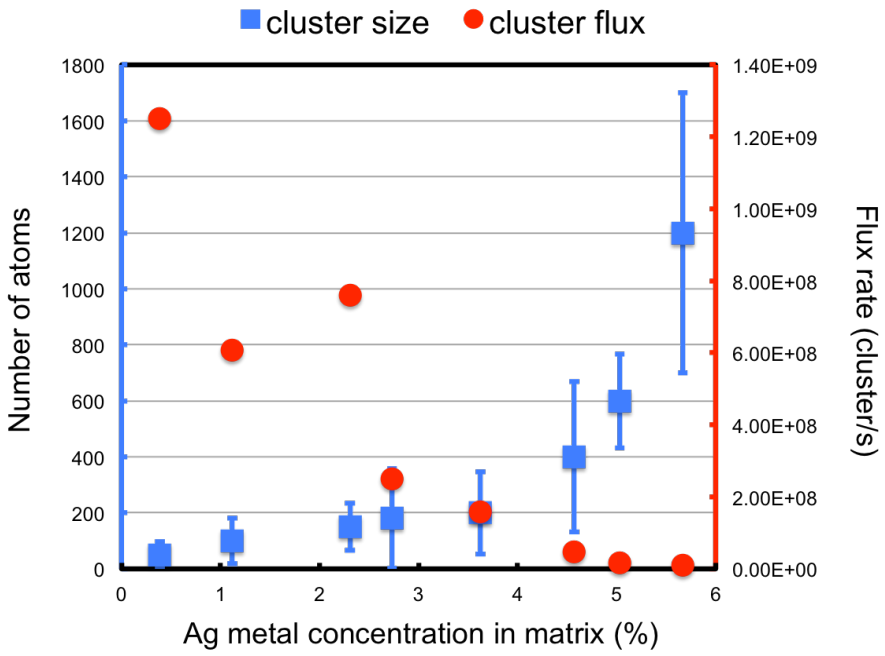

Figure 5.10 A plot of cluster size and calculated cluster flux as a function of metal concentration. Blue blocks are the cluster size and red dots represent cluster flux. The size of cluster is measured from the integrated HAADF intensity comparing with the HAADF intensity of single atoms and the error bar is obtained from the half width of the standard deviation of the size distributions. The cluster flux is calculated from the cluster density in HAADF STEM images.

5.5.5 Effects of beam energy

The effects of beam energy on cluster production in MACS was also studied in the demonstration apparatus. The energy of the Ar^+ ion beam generated from the cluster source is controlled by the bias voltage on the cold finger. The bias voltage on the sample holder is kept same as that on the cold finger, so that the region between the sample holder and the cold finger is electrical field free. Metal concentration is kept the same, 1.1%, for all samples. Figure 5.11(a-d)

shows the HAADF STEM images of Ag clusters prepared with incident beam energy from 950eV to 2450eV. The histograms of size distributions are shown in Figure 5.11 (e-h).

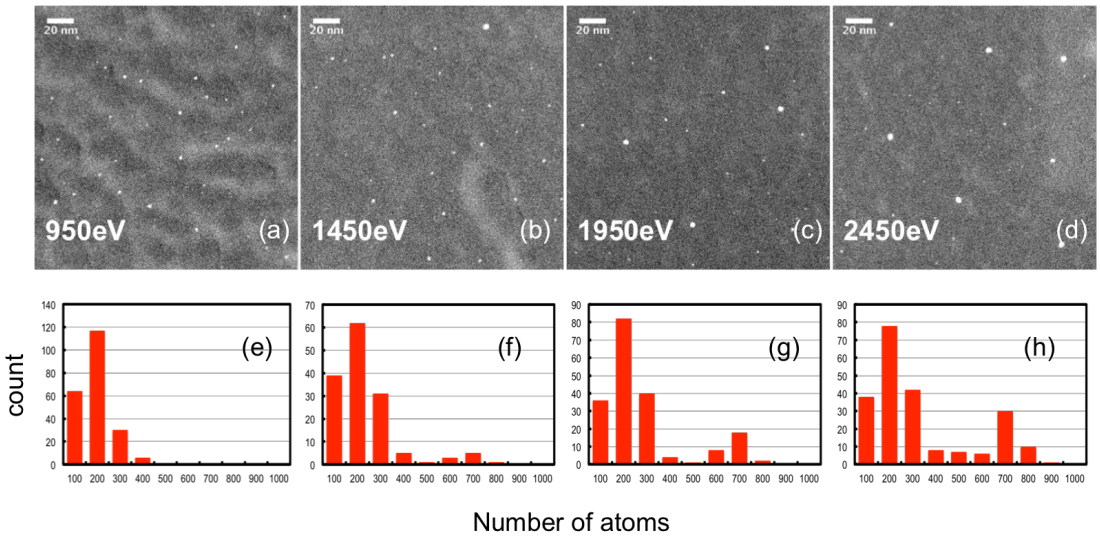

Figure 5.11 (a-d) HAADF STEM images of Ag clusters prepared with incident beam energy from 950eV to 2450eV. (e-h) The histograms of size distributions of clusters measured from the integrated HAADF intensities. Related parameters: matrix condensation support, 400 mesh grid; matrix temperature, 12K, gas dosing pressure, $3x10^{-6}$ mbar; metal concentration in the matrix, 1.1%; matrix condensation time, 200s; matrix thickness, ~85nm; incident Ar beam current, 10nA; deposition time, 60s.

As shown in the HAADF images and histograms, double peaks starts to appear in the size distributions when using high incident beam energy. For example, in the histogram of size distribution shown in Figure 5.11 (h), which is the clusters prepared using 2450eV incident ion beam, there are two peaks at 200 and 700 atoms respectively. However, in the histogram shown in Figure 5.11 (e), which is the low incident beam energy, 950eV, the second peak is invisible. The

observation of bi-model distribution with high-energy incident ion beam proves our speculation of the multiple mechanisms of cluster formation in the MACS. The clusters aggregated during the ion impact receive more momentum to capture more atoms to form large clusters, when using high-energy ion beam [19,22,24-26]. However, the dominant parameter determining the overall size distribution is still the metal concentration.

5.5.6 Improvements to increase cluster flux

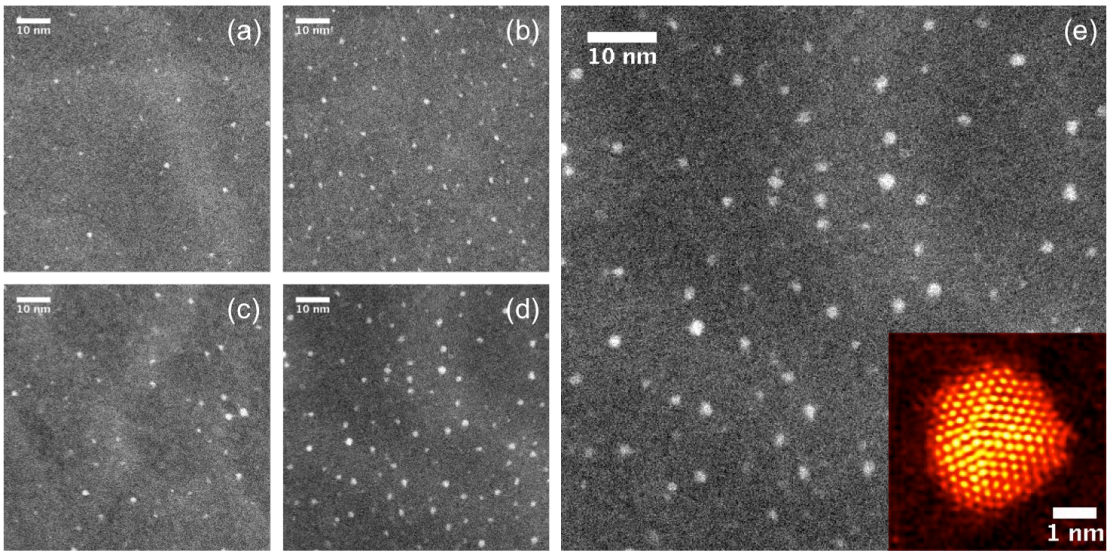

Figure 5.12 HAADF STEM images of Ag cluster samples prepared with different matrix condensation support and different deposition time, (a) 400 mesh grid, 60s; (b) 1000 mesh grid, 60s; (c) 2000 mesh grid, 5s; (d) quantifoil, 5s. (e) is the highlight of (d) with atomic resolution of a Ag cluster. Related parameters: matrix temperature, 12K, gas dosing pressure, $3x10^{-6}$ mbar; metal concentration in the matrix, 1.1%; matrix condensation time, 200s; matrix thickness, ~85nm; incident Ar beam current, 10μA.

Two improvements have been applied to the MACS demonstration system to increase the cluster flux. Firstly, a high flux ion source, Omicron ISE5, was used to replace the Ar ion beam generated using the magnetron cluster source. The ion source is able to generate up to Ar ion beam current of 80μA and 12% of which, ~10μA, is able to be focused on cold finger at beam energy of 1keV. Secondly, several high density mesh matrix condensation supports were used to replace the 400 mesh TEM matrix condensation grid such as 1000, 2000 mesh copper grid and quantifoil.

Matrix support	Density of holes/inch^2	Deposition time (s)	Cluster flux/s	Flux mg/hour
400 mesh	$1.6x10^5$	60	1.1E9	1.42E-4
1000 mesh	$1x10^6$	60	2.3E9	2.97E-4
2000 mesh	$4x10^6$	5	1.1E10	1.42E-3
Quantifoil	$1x10^8$	5	3.3E10	4.26E-3

Table 5.3 Calculated cluster flux prepared with different type matrix condensation supports and deposition time. Cluster flux is measured based on the cluster density on HAADF STEM images.

Figure 5.12 (a-d) shows the HAADF STEM images of four samples prepared with different matrix condensation supports and different deposition times in order to investigate the effects on cluster flux. The calculated cluster flux is summarized in the Table 5.3. As shown in the table, cluster flux is increased with the density of holes in the matrix condensation support as the matrix grows as an adlayer on the bars of each mesh and matrix supports with higher density

holes lead to a higher matrix coverage. For example, quantifoil has a density of holes 25 times than that of 400 mesh grid, therefore the cluster flux using quantifoil as the matrix support is 3 times higher. Compared to the cluster flux generated using Ar ion beam from the magnetron source, the cluster flux using Ar ion gun and quantifoil has been increased over 50 times, from 6.1E8/s (7.8E-4 mg/hour) to 3.3E10/s (4.3E-3 mg/hour).

5.5.7 Continuous production

When using high flux Ar ion source for cluster production, the matrix is depleted quickly (only last for few minutes) unless replenished. As shown in Figure 5.13, the cluster flux of two samples prepared successively from the same matrix without replenishment is dropped rapidly from 1.9×10^{10}/s (2.5E-3 mg/hour) for the first sample to 8×10^{9}/s (1E-3 mg/hour) after 10s sputtering. Therefore, continuous replenishment of the matrix is a necessity to remain the high cluster flux.

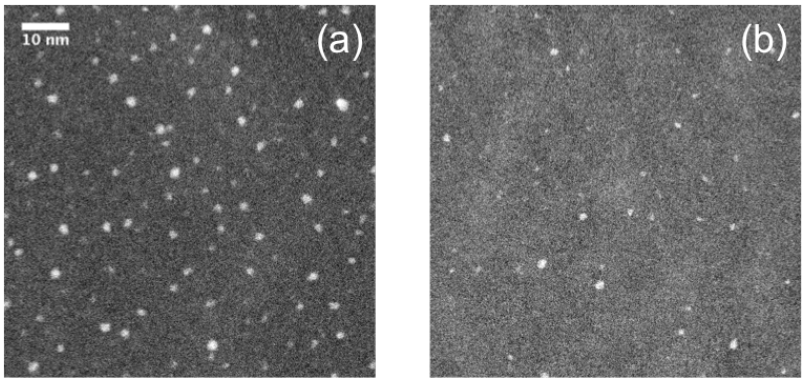

Figure 5.13 HAADF STEM image of clusters prepared successively from the same matrix without replenishment. Related parameters: matrix temperature, 12K,

matrix support, quantifoil; gas dosing pressure, $3x10^{-6}$ mbar; metal concentration in the matrix, 1.1%; matrix condensation time, 200s; matrix thickness, ~85nm; incident Ar beam current, 10μA; deposition time, 10s.

To sustain the production of clusters in high flux, replenishment of the matrix during the cluster production/ion bombardment was tested. Metal atoms and rare gas are re-condensed onto the matrix condensation grid every 20s between the cluster production by rotating cold finger 90 degree to face the evaporator. The old finger is rotated back after the replenishment to continue producing clusters. The HAADF STEM images of six samples prepared using this approach are shown in Figure 5.14 as well as the calculated cluster flux.

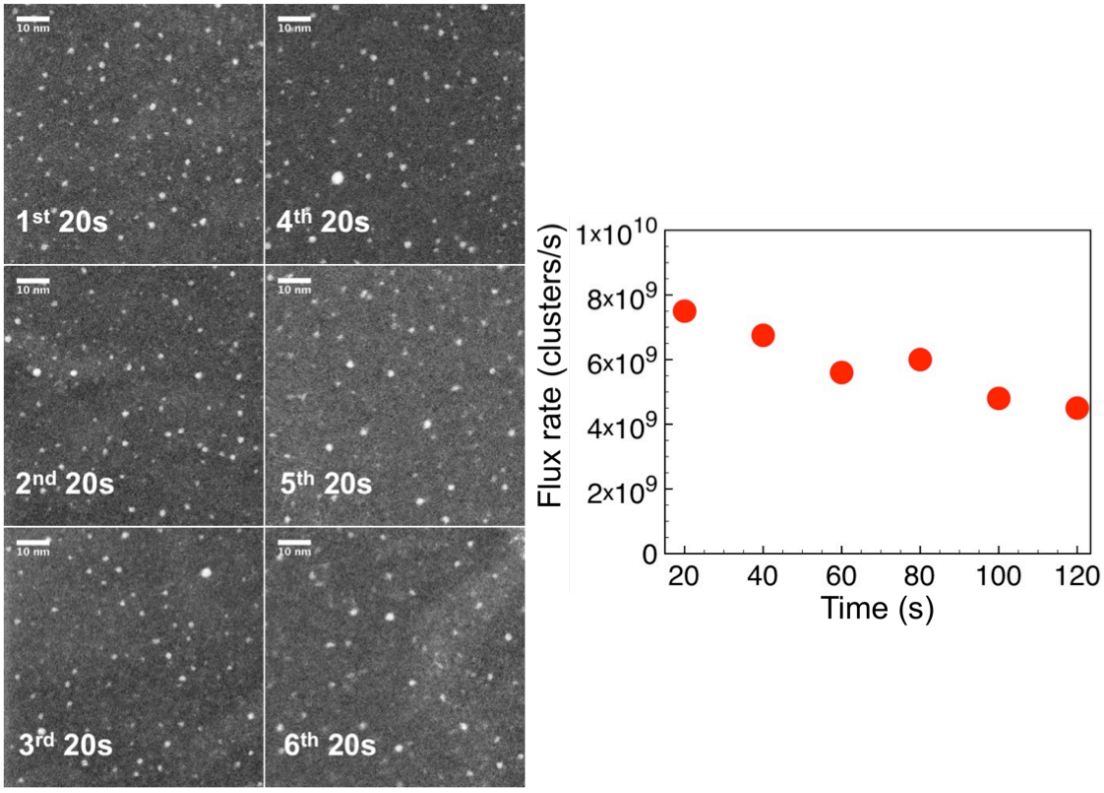

Figure 5.14 HAADF STEM images of six Ag cluster samples produced with the replenished matrix (left) and the calculated cluster flux based on the cluster

density in HAADF STEM images (right). Related parameters: matrix temperature, 12K, matrix support, quantifoil; gas dosing pressure, $3x10^{-6}$ mbar; metal concentration in the matrix, 1.1%; matrix replenishing time, 100s; matrix thickness, ~85nm; incident Ar beam current, 10μA; deposition time, 20s.

With the replenishment, cluster flux only decreases slightly (less than 50% after 2 minutes) with time and the downward trend seems reach a stable flux of clusters around 4×10^{9}/s (5.2E-4 mg/hour) after 120s, which indicates high flux of clusters can be continuously produced by simply replenishing the matrix. In our MACS demonstration apparatus, the cluster production has to be interrupted during the matrix replenishment. However, with a new chamber design in the future, the evaporator will be mounted in line with the Ar^{+} ion gun, matrix support and sample holder. The condensation of matrix and the deposition will be taking place at the same time. The continuous high flux of clusters will be achieved with careful selected condensation rate and the deposition rate.

5.6 Summary

In this chapter, the idea of cluster production using MACS technology has been introduced. The MACS demonstration experimental apparatus was designed and built. The methodology of cluster formation in the matrix was explained. The proof-of-principle of cluster production in the MACS was demonstrated by the successful production of Au and Ag clusters. The effects of parameters such as metal concentration and incident beam energy on cluster production were preliminarily studied. Results show the clusters produced using the MACS

method had relatively narrow size distributions ($M/\Delta M \sim 1$) and cluster size was sensitive to the metal concentration in the matrix, with a higher metal concentration making larger clusters. However, the flux of cluster decreases with the metal loading percentage in the matrix. Incident beam energy also affected the cluster size. Two improvements, high flux ion source and high-density matrix supports, were applied to scale up the cluster production rate. At last continuous production was tested by the replenishment of the matrix.

In the next chapter, we will introduce an upgraded MACS apparatus, the MACS 1, in order to scale up the cluster production rate. Also systematically investigation cluster formation mechanisms, charge fraction and the mass spectra measurement of clusters are discussed.

List of references

[1] Habibpour, Vahideh, et al. "Catalytic oxidation of cyclohexane by size-selected palladium clusters pinned on graphite." *Journal of Experimental Nanoscience* 8.7-8 (2013): 993-1003.

[2] Silvera, Isaac F., and Victor V. Goldman. "The isotropic intermolecular potential for H2 and D2 in the solid and gas phases." The Journal of Chemical Physics 69.9 (1978): 4209-4213.

[3] Mirsky, Kira. "Carbon monoxide molecules in an argon matrix: empirical evaluation of the Ar· Ar, C· Ar and O· Ar potential parameters." Chemical Physics 46.3 (1980): 445-455.

[4] Tang, K. T., and J. Peter Toennies. "New combining rules for well parameters and shapes of the van der Waals potential of mixed rare gas systems." Zeitschrift für Physik D Atoms, Molecules and Clusters 1.1 (1986): 91-101.

[5] Mann, D. E., N. Acquista, and David White. "Infrared Spectra of HCl, DCl, HBr, and DBr in Solid Rare‐Gas Matrices." The Journal of Chemical Physics 44.9 (1966): 3453-3467.

[6] Makeev, Maxim A., and Albert-László Barabási. "Ion-induced effective surface diffusion in ion sputtering." Applied physics letters 71.19 (1997): 2800-2802.

[7] Winters, Harold F., et al. "Energy transfer from rare gases to surfaces: Collisions with gold and platinum in the range 1–4000 eV." *Physical Review B*41.10 (1990): 6240.

[8] Coufal, H., et al. "Energy transfer from noble-gas ions to surfaces: Collisions with carbon, silicon, copper, silver, and gold in the range 100–4000 eV."*Physical Review B* 44.10 (1991): 4747.

[9] Averback, R. S., and T. Diaz de la Rubia. "Displacement damage in irradiated metals and semiconductors." Solid State Physics 51 (1997): 281-402.

[10] Smith, Roger. Atomic and ion collisions in solids and at surfaces: theory, simulation and applications. Cambridge University Press, 2005.

[11] De La Rubia, T. Diaz, et al. "Role of thermal spikes in energetic displacement cascades." Physical review letters 59.17 (1987): 1930.

[12] Aderjan, Ralf, and Herbert M. Urbassek. "Molecular-dynamics study of craters formed by energetic Cu cluster impact on Cu." Nuclear Instruments and Methods in Physics Research Section B: Beam Interactions with Materials and Atoms 164 (2000): 697-704.

[13] Nordlund, K., et al. "Defect production in collision cascades in elemental semiconductors and fcc metals." Physical Review B 57.13 (1998): 7556.

[14] https://en.wikipedia.org/wiki/Collision_cascade

[15] Pratontep, S., et al. "Size-selected cluster beam source based on radio frequency magnetron plasma sputtering and gas condensation." *Review of scientific instruments* 76.4 (2005): 045103.

[16] Von Issendorff, B., and R. E. Palmer. "A new high transmission infinite range mass selector for cluster and nanoparticle beams." *Review of Scientific Instruments* 70.12 (1999): 4497-4501.

[17] Young, N. P., et al. "Weighing supported nanoparticles: size-selected clusters as mass standards in nanometrology." *Physical review letters* 101.24 (2008): 246103.

[18] Abràmoff, Michael D., Paulo J. Magalhães, and Sunanda J. Ram. "Image processing with ImageJ." *Biophotonics international* 11.7 (2004): 36-42.

[19] Balaji, V., et al. "Sputtering yields of condensed rare gases." *Nuclear Instruments and Methods in Physics Research Section B: Beam Interactions with Materials and Atoms* 46.1 (1990): 435-440.

[20] Sigmund, Peter. "Theory of sputtering. I. Sputtering yield of amorphous and polycrystalline targets." *Physical review* 184.2 (1969): 383.

[21] Behrisch, Rainer, and Klaus Wittmaack, eds. *Sputtering by particle bombardment*. Vol. 3. Berlin: Springer, 1983.

[22] Laegreid, Nils, and G. K. Wehner. "Sputtering yields of metals for Ar+ and Ne+ ions with energies from 50 to 600 eV." *Journal of Applied Physics* 32.3 (1961): 365-369.

[23] Smith, Roger. *Atomic and ion collisions in solids and at surfaces: theory, simulation and applications*. Cambridge University Press, 2005.

[24] Steinbrüchel, Christoph. "Universal energy dependence of physical and ion-enhanced chemical etch yields at low ion energy." *Applied physics letters* 55.19 (1989): 1960-1962.

[25] Sigmund, Peter. *Elements of sputtering theory*. press, 2009.

[26] Zalm, P. C. "Energy dependence of the sputtering yield of silicon bombarded with neon, argon, krypton, and xenon ions." *Journal of Applied Physics* 54.5 (1983): 2660-2666.

Chapter 6 Development of the Matrix Assembly Cluster Source (MACS)

In the previous chapter, the first experimental apparatus of the Matrix Assembly Cluster Source (MACS) was introduced and the principle of the MACS was demonstrated by the production of Au and Ag clusters as well as preliminary studies of effects of matrix parameters on cluster production. This Chapter introduces an upgraded experimental setup of the MACS system, the MACS 1, for scaling up the cluster production rate, not only transmission mode, but also using the reflection mode. It also includes systematic investigation of the effects of metal concentration, matrix temperature and incident beam energy on cluster size and flux. Also, measurements of charge fractions and mass spectra are reported.

The work presented in this chapter involve a few collaborators. The instrument design and development were done together by the author and William Terry. The software and computer interface development for the MACS apparatus were done by William Terry. The SIMION simulation was done by the author and

William Terry. The sample preparations were done by the author, William Terry (Ag clusters) and Dr. Richard Balog (Au clusters). Charge fractions and mass spectra measurements were done by the author and Rongsheng Cai.

6.1 Experimental apparatus of MACS 1

6.1.1 Overview

The MACS 1 is the upgraded apparatus based on the principle demonstrated in the MACS demonstration system discussed in last chapter. The MACS is designed to scale up the cluster production rate and understand cluster formation mechanisms by systematic investigation of the experimental parameters. Compared to the demonstration apparatus, the improvements having been applied in MACS 1 are highlighted below.

(i) Cooling system; A closed-cycle cryocooler was installed to provide the cooling power for the condensation of the matrix.

(ii) Evaporator; A high temperature effusion cell (up to 2000°C with a crucible size of 10cc) was employed for the evaporation of cluster materials.

(iii) Ion source and ion optics; High flux ion source with maximum output current of 4mA was installed. Ion optics was designed and built to focus more ions onto matrix.

(iv) Matrix condensation support; 1 inch by 1 inch matrix condensation support was used.

(v) Cluster production approaches; Both transmission mode and reflection mode were used in the MACS 1 for cluster productions.

(vi) Analysis methods; Lateral time-of-flight mass spectrometer was involved in in-flight analysis of clusters produced in the MACS 1 in addition to the STEM measurement of deposited clusters.

The schematic diagram of the MACS 1 is shown in Figure 6.1. The apparatus can be switched from transmission mode (6.1a) to reflection mode (6.1b) by rotating the matrix support. Figure 6.1(c) shows the MACS 1 apparatus in Nanoscale Physics Research Laboratory in University of Birmingham.

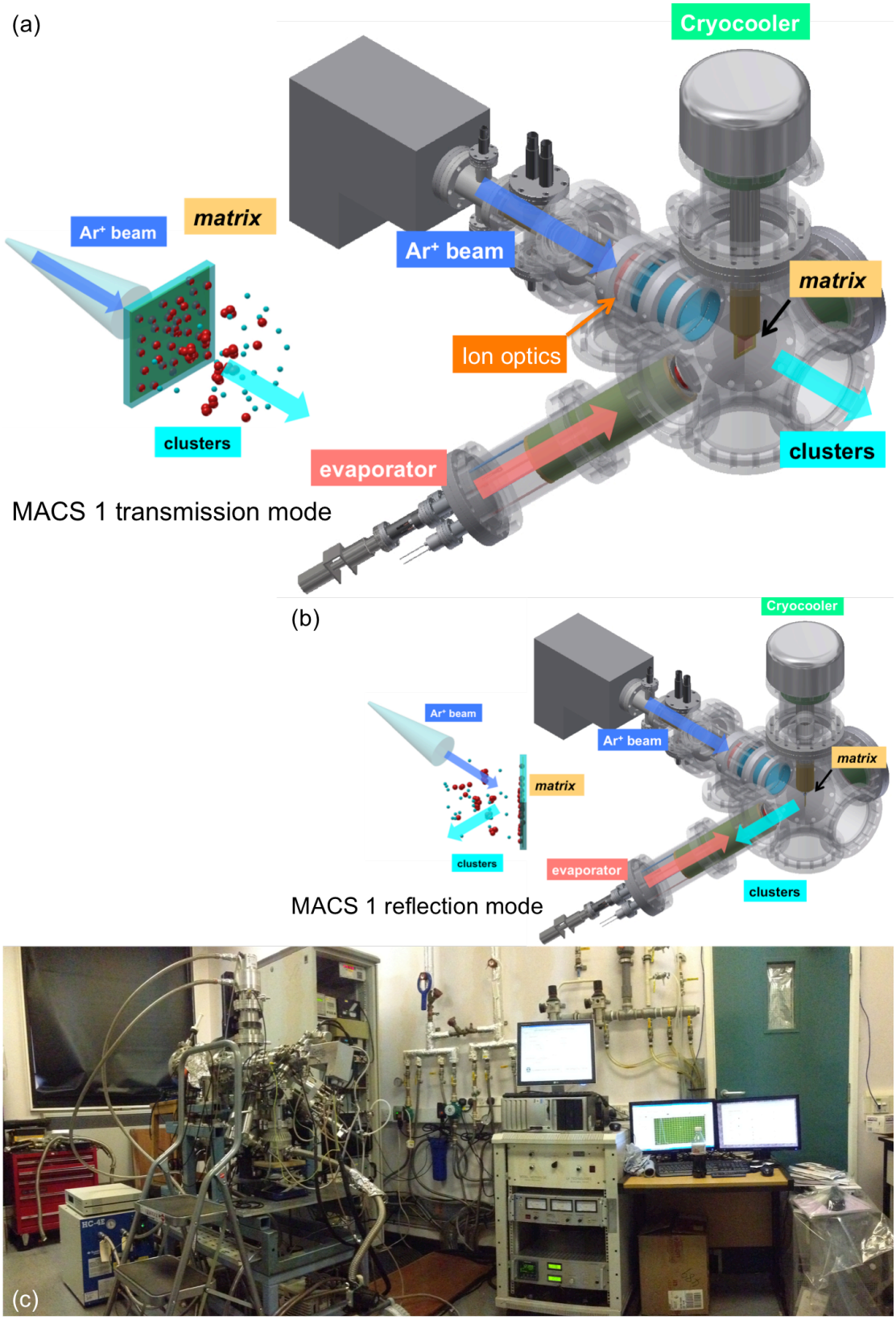

Figure 6.1 The schematic diagram of the MACS 1 transmission mode (a) and reflection mode (b). The apparatus can be switched between the two modes by

rotating the matrix support. (c) The MACS 1 apparatus in Nanoscale Physics Research Laboratory in University of Birmingham.

6.1.2 Cryocooler

The cooling system used in the MACS 1 is a closed cycle cooling system, which is able to cool down the matrix to around 10K in around 2 hours with a power of 6.7W. The cooling system consists of a cooling head and a compressor both of which are from Sumitomo cryogenics, the CH-204 series. The cooling head is mounted on top of the generation chamber and it is connected with the compressor via two transfer lines (supply and return). The working principle of the cryocooler is similar to a refrigerator in which the cooling head is cooled by the cold helium gas delivered from the compressor and the hot gas is pumped back for recycle after cooling.

6.1.3 Matrix condensation support

A 1-inch by 1-inch matrix condensation support is used in the MACS 1 instead of 3mm grid in the MACS demonstration apparatus to scale up the cluster production rate. The matrix support used for transmission mode is 1000 copper mesh with 10μm opening, 15μm line width and 13μm thickness. For transmission mode, it is a solid copper plate with a thickness of 100μm. The matrix support is fixed on a sample stage on top of the cryocooler. The stage to fix the matrix support is a window frame and thin gold foil is filled in the gap between the stage and the matrix support to maintain good thermal transfer as

show in Figure 6.2(a). A silicon diode temperature sensor, DT-670-CU from Lakeshore, is fixed against the matrix support to monitor the temperature of the matrix as shown in Figure 6.2(b). The reading curves of the temperature sensor is calibrated with three points, ice water, liquid nitrogen and liquid helium. The top of the cryocooler is electrical insulated from the whole body by a sapphire in order to monitor the incident beam current on the matrix. The current is read from the Keithley 6485 picoammeter.

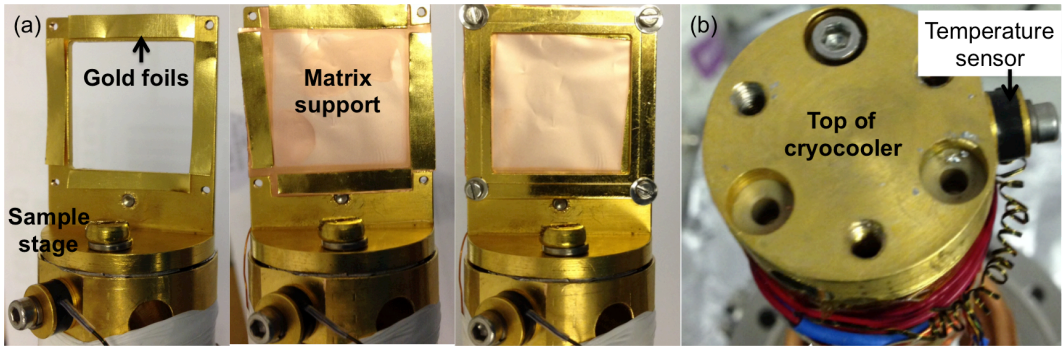

Figure 6.2 (a) Photograph illustrates the sample stage and matrix support on the top of the cryocooler. Thin gold foil is filled in the gap between the stage and the matrix support to maintain good thermal transfer. (b) Photograph shows the position of the silicon diode temperature sensor (DT-670-CU from Lakeshore).

6.1.4 Evaporation

The evaporator installed in the MACS 1 is the high temperature effusion cell, from Createc with a maximum evaporation temperature of 2000°C and a crucible size of 10cc. The effusion cell is mounted on the angled DN80CF flange facing the center. The evaporation temperature is controlled precisely using a PID controller with an accuracy of 0.1K. To minimize the thermal radiation on the

matrix, the evaporator is surrounded by a hollow cylinder tube, which is water cooled. Additionally a radiation shield, made of tantalum, is mounted on top of the evaporator, which is also attached to the water cooling cylinder. Therefore, the matrix temperature only fluctuates less than 1K when evaporator is heated up to 1300°C and about 1.5~2K when it is up to 1500°C. The evaporation rate is measured using the quartz crystal microbalance mounted next to the matrix support (5mm away from the matrix), similar to that used in the original MACS system. The evaporation speed for Ag on the matrix as a function of heating temperature is shown in Figure 6.3.

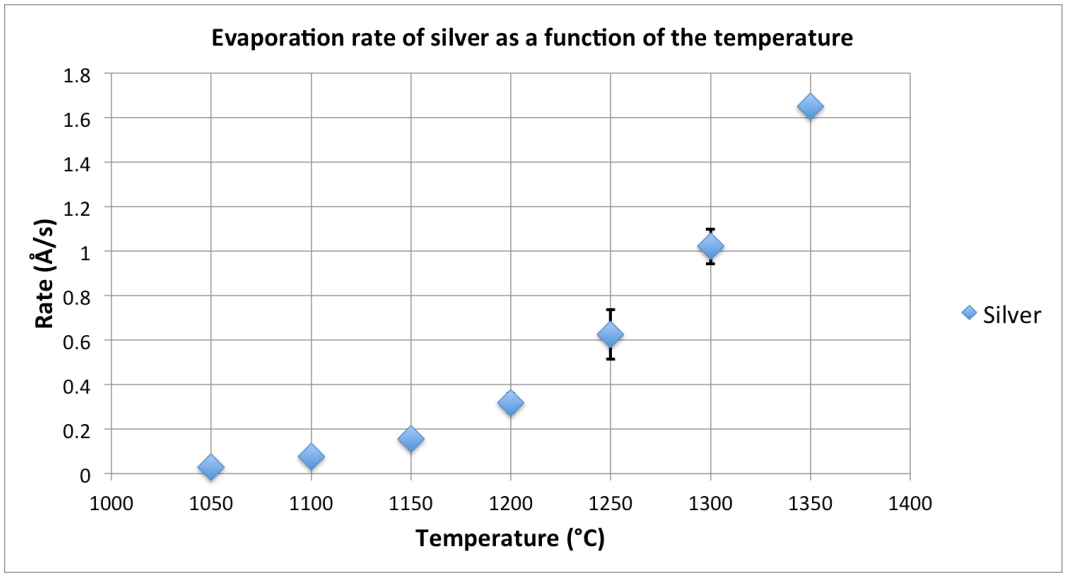

Figure 6.3 Calibrated evaporation speed of silver on the matrix as a function of heating temperature.

6.1.5 Ion source

The ion source employed in the MACS 1 is a sputter ion gun from Tectra with a maximum output current of 4mA to replace the Omicron ion source used in the

demonstration apparatus, which is only up to 100μA. The new ion source is filamentless, and plasma is ignited from gas phase via the mechanism of microwave plasma discharge [1]. A microwave generator is mounted in the back of the ion gun and the energy of the generated microwave is coupled into a coaxial waveguide and delivered into the plasma cup in front of the ion source. The injected inert gas, Ar here, is breakdown and discharged in the plasma cup because of the intense oscillating electrical fields created by the microwave. Moreover, a quadrupole magnetic field surrounds the plasma cup to enhance the plasma density. Ions are then extracted out from the plasma cup by extraction optics consisting of two grid elements. The energy of the ions is controlled by one of the extraction grids. The beam energy can be varied between 25eV to 5keV.

6.1.6 Ion optics and SIMION simulations

Although high flux ion beam can be generated using the new sputter gun, the initial beam direction is divergent as measured experimentally by beam profile as shown in Figure 6.4. The increased beam current as a function of energy is because the electrical field that drives ions out has a linear relationship with the voltage applied on the grid, which exactly determines the beam energy. In order to focus more most of ions onto matrix, ion optics were designed. The design of the ion optics is inspired by the Wehnelt idea, which is a well-established technique used in many FIB-SEM systems [2-3]. The designed ion optics for the sputter gun in MACS 1 system consists of four ion optic lens elements including the Wehnelt and a set of three Einzel lenses. With the ion optics the trajectory of

the divergent ion beam is squeezed by the wehnelt at the entrance and then focused by the einzel lenses. To obtain the optimal performance, the voltage settings and dimensions of each lens element are tested in the SIMION simulation [4].

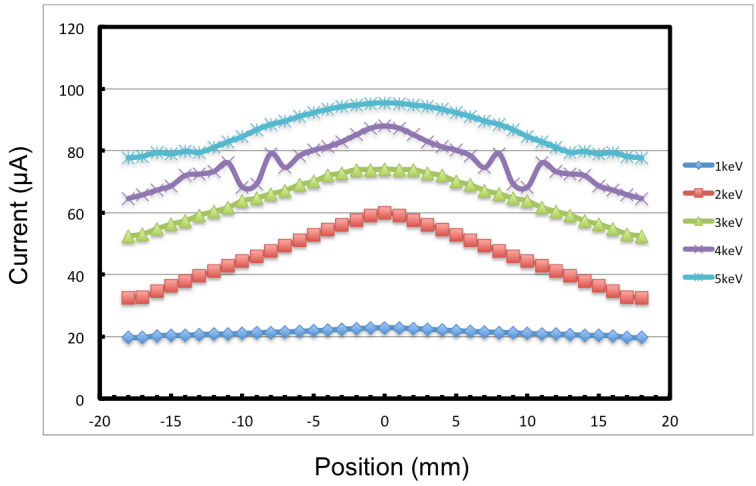

Figure 6.4 Experimentally measured Ar ion beam profile generated from the Tectra sputter gun at different ion beam energies.

The version of the simulation software we used is SIMION 8.1. In the SIMION, the dimensions of each lens element are defined by the geometry file, which includes the geometries and locations of the lenses. As shown in Figure 6.5(a), four lenses are created in front of the ion source and a plate is placed in the end, the same position but bigger than the matrix, to record the spatial distribution of ions. The incident ion beam in the simulation is defined by the .fly file, which includes source position, source geometry, energy spread, divergent angle and all the parameters are exactly identical with the Ar beam profile experiment results. The dimensions (with range of 0~100mm) and corresponding voltage settings (0~±20000V) of each lens element are automatically tuned in the program. The

divergence and transmission ratio of the ion beam passing through the ion optics is figured out by analyzing positions of ions hitting the plate. Following parameters are varied in the simulation to achieve the best performance of the ion optics, such as Wehnelt size (OD, ID, aperture size, aperture thickness), lens size (OD, ID, length), and gaps between each lens element. 2keV ions (red) and 5keV ions (blue) are tested in the simulations as two examples.

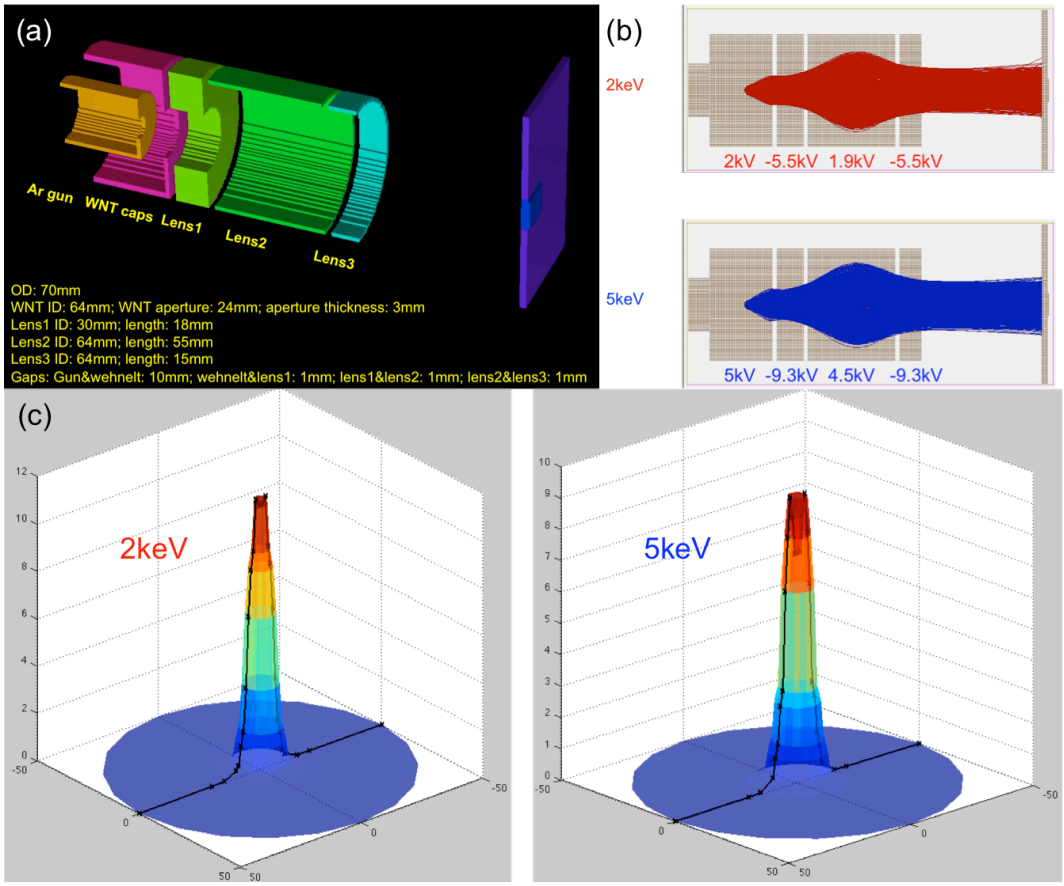

Figure 6.5 (a) The geometry of the ion optics created in SIMION 8.1 including the Wehnelt (WNT) and other three Einzel lenses and optimal dimensions obtained from simulations. Each color represents one electrode. A plate is placed at the end to monitor the spot size of ion beam after passing through the ion optics. (b) Simulations of the trajectories of 2keV and 5keV Ar ion beam with the optimally configured ion optics. The optimal voltage settings for each lens are also shown.

(c) Spatial distributions of the 2keV and 5keV Ar ions hitting on the matrix after focused by the ion optics.

The optimal dimensions obtained from simulations are also shown in Figure 6.5(a), which is a balance of transmission ratio (>90%), focus (over 85% onto matrix), required voltages (less than 10kV) and dimensions (less than 100mm in order to fit in DN100CF flange). The trajectories of 2keV and 5keV ion beams passing through the optimal ion optics configuration are shown in Figure 6.5(b). The required voltages are also shown. The spot size of the Ar ions impinging on the matrix (which is the final plate in the simulation) is recorded spatially and the data analyzed in Matlab (by William Terry). The 3D plot of the spatial distributions of Ar ions landing on the matrix at energies of 2keV and 5keV are shown in Figure 6.5(c). The results obtained from the simulation show we are able to focus over 85% ions onto matrix area (1 inch by 1 inch) with required voltages less than 10kV.

6.1.7 Design of ion optics

The ion optics designed for the ion source are integrated on a DN100CF flange. As shown in the schematic diagram in Figure 6.6 (a), two stainless steel rods are fixed on the inner side of the flange to support the whole ion optics. For electrical insulation, PTFE washers are used to mount the set of lenses on the supporting rods. The designed ion optics were manufactured by the workshop based in University of Birmingham and the assembled ion optics with ion source is shown in Figure 6.6 (b-d). Each ion optic lens is connected to high voltage feedthroughs

via kapton wires. Four high voltage power supplies are used to apply voltages to create the electrical field on each lens, two positive (up to 5kV, 10mA) and two negative (up to 10kV, 5mA). The power supplies are MK series from Glassman, all controlled using Labview (developed by William Terry).

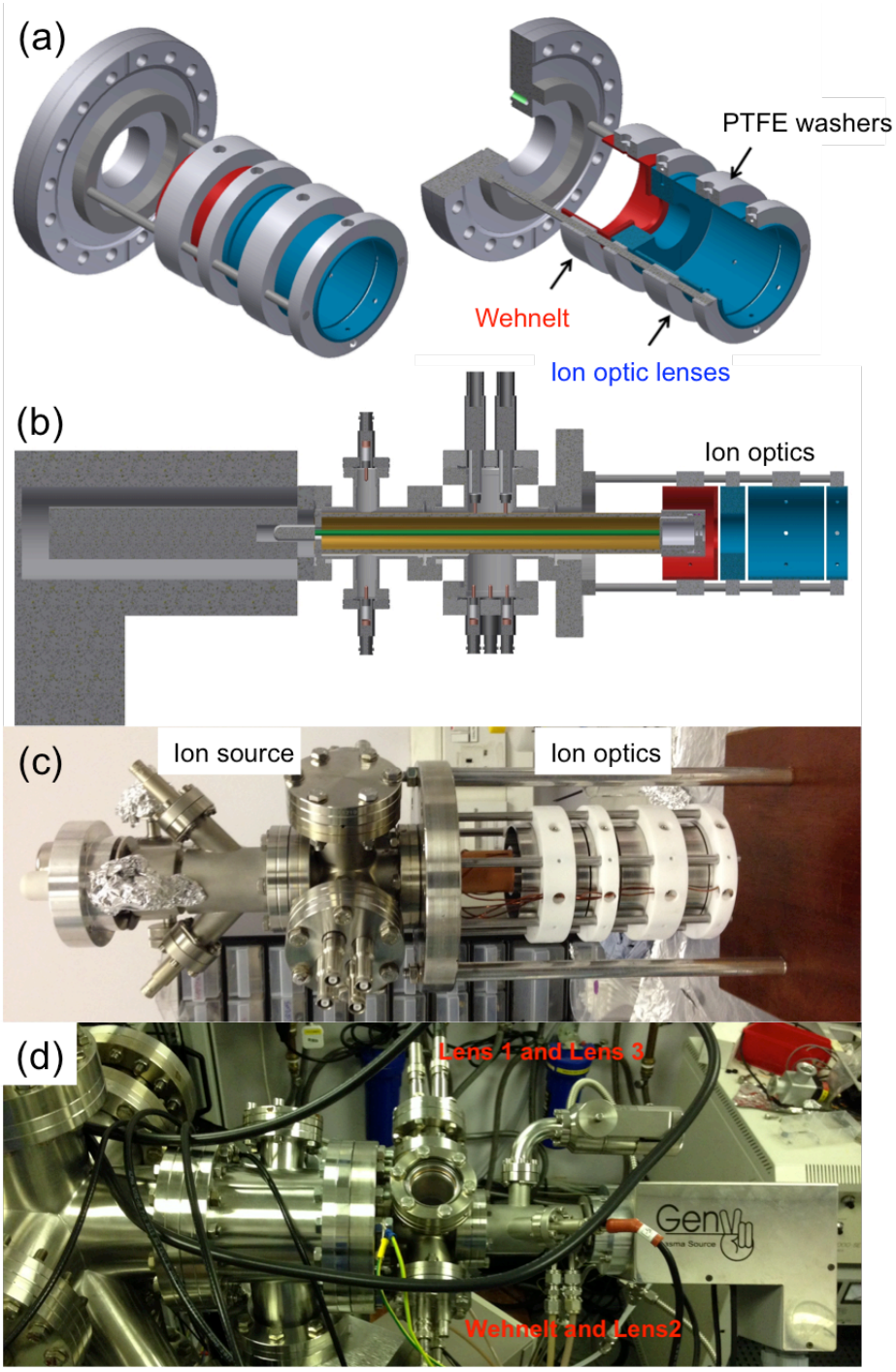

Figure 6.6 (a) Schematic diagram of the designed ion optics integrated on a DN100CF flange. (b) Schematic diagram of the designed ion optics assembled in

front of the ion source. (c) Photograph of the assembled ion optics with ion source. (d) Photograph of the ion source with ion optics installed in the MACS 1.

6.1.8 Ar beam profile with ion optics

To evaluate the practical effect that the ion optics has over the ion beam, the beam profile was measured experimentally using the optimal voltage settings obtained from the simulations. As shown in the Figure 6.7(a), with the help of ion optics most ions are focused inside the matrix area (from -12.7mm to 12.7mm) as the half width of the ion beam at all different energies is around 20mm. The peak current for 5keV ion beam is increased from 100μA to nearly 300μA.

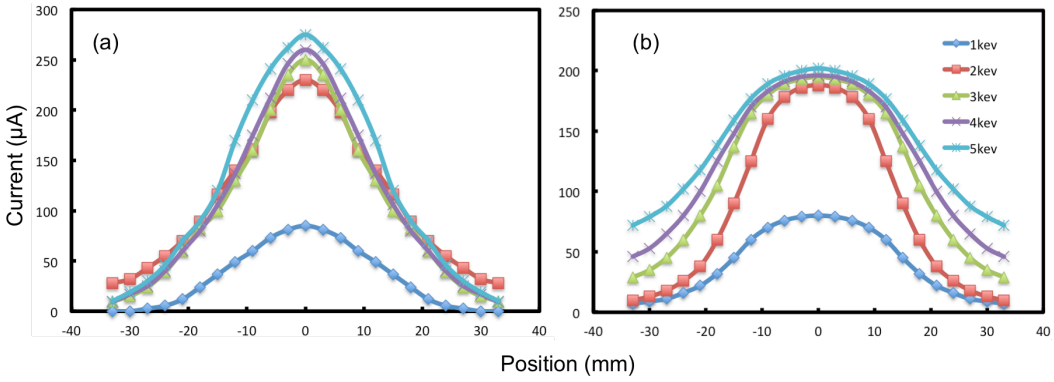

Figure 6.7 (a) Ar ion beam profile measured for different beam energies using the lens voltage settings obtained from simulations. (b) Ar ion beam profile measured for different beam energies using defocused lens voltage settings.

However, in order to keep the matrix being uniformly sputtered during the experiment, the Ar ion beam is deliberately defocused slightly to achieve uniform beam current across the whole matrix area. To achieve this, voltages on negative

lenses are decreased about 5% and voltages on positive lenses are slightly tuned up about 7%. The profile of Ar ion beam at the defocused settings is shown in Figure 6.7(b).

6.2 Ag clusters produced in MACS 1

The performance of the MACS 1 was first tested by generating Ag clusters, especially in terms of the cluster production rate and cluster size control. Similar to the work conducted using the MACS demonstration system, the effects of parameters such as evaporation speed, incident Ar ion beam current and energy and matrix temperature on the cluster flux and size were systematically investigated under more precise control and with a relatively larger range.

6.2.1 Cluster flux

The flux of clusters produced in the MACS 1 is measured from the density of clusters deposited on the substrate within certain time. For this purpose, a sample holder here contains an array of amorphous carbon film TEM grids was installed as shown in Figure 6.8(a). The equivalent cluster flux is calculated based on the average cluster density measured from HAADF STEM images times multiplied by total production area and then divided by the deposition time. The sample holder used here covers an area of 30mm by 30mm, which is approximately the area of the matrix condensation support (1 inch by 1 inch). In order to achieve the maximum cluster flux, the highest beam energy 5keV is used to sputter the matrix as sputtering yield and maximum output beam current are

increased with the incident beam energy [9]. Clusters are produced in transmission mode. Figure 6.8(b) shows HAADF STEM images of clusters deposited on each sample. To minimize the statistical error, at least 25 images are taken on each sample. The average cluster density across all these samples was approximately $1.8\text{x}10^5 \pm 1200/\mu m^2$. Additionally we have demonstrated that clusters production area is at least 30mm by 30mm. Therefore the total cluster flux is

$$cluster\ flux = \frac{average\ cluster\ density \times matrix\ area}{deposition\ time}$$

$$= (5.83 \pm 0.4) \times 10^{11}/s$$

If all the clusters produced are positive charged, the cluster flux is equivalent to nearly 100nA (0.2 mg/hour).

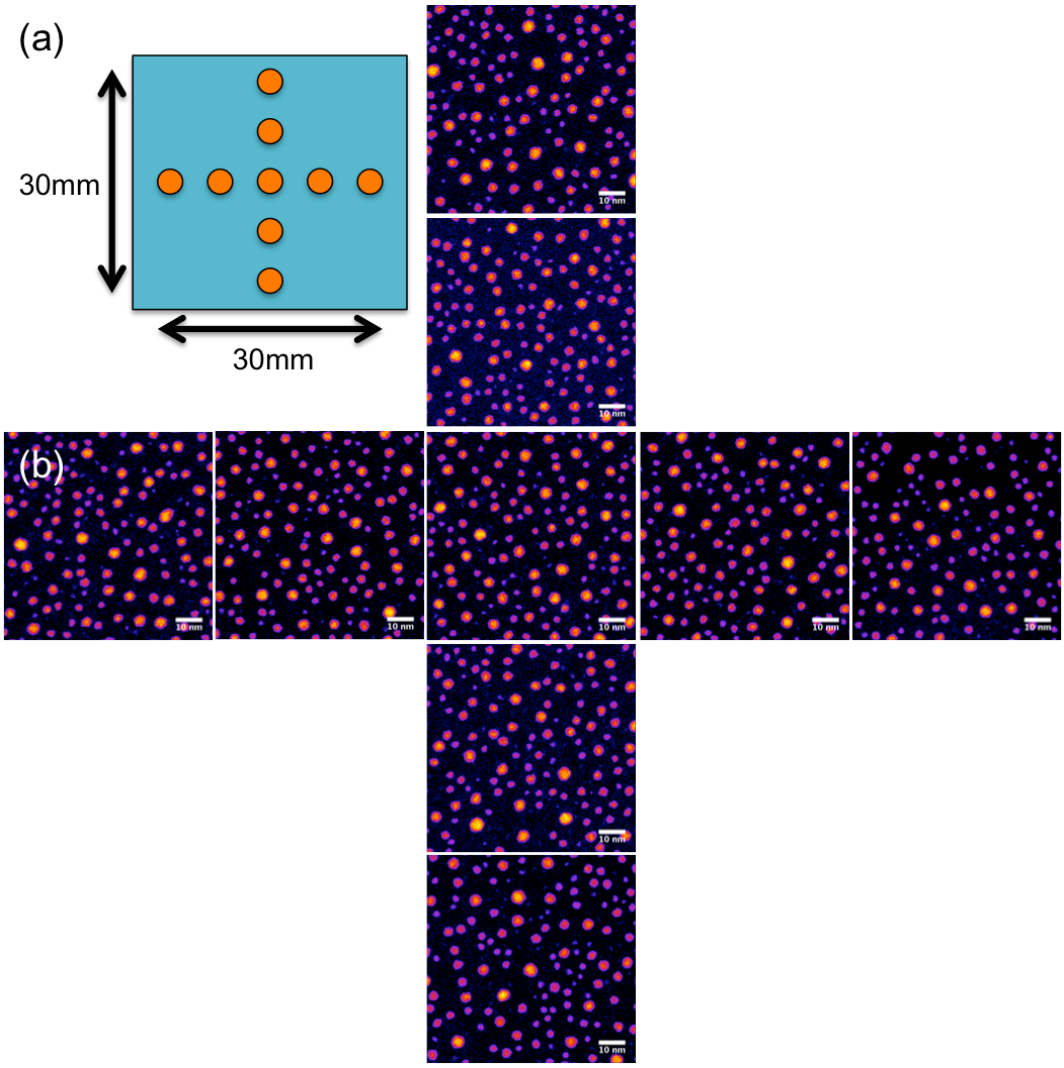

Figure 6.8(a) Schematic diagram of the sample holder installed to measure the cluster flux. The sample holder consists a cross array of TEM grids covering an area of 900mm^2. (b) HAADF STEM images of clusters deposited on each sample. The area cluster density is approximately 1.8x10^5/μm^2. Related parameters, matrix condensation support, 1000 mesh copper grid; matrix temperature, 9K; condensation time, 300s; metal concentration, 2.2%; Ar gas dosing pressure, 6E-8mbar; matrix thickness, ~128nm; incident ion beam current on matrix, 300μA; beam energy, 5keV; deposition time, 20s.

6.2.2 Large area coating using clusters produced in MACS 1

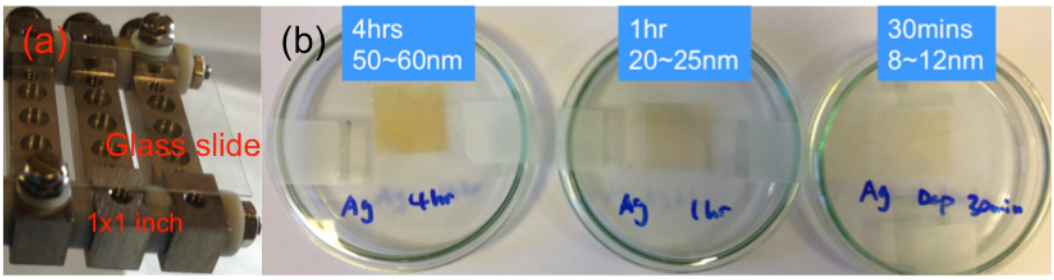

Figure 6.9(a) Photograph of 1 inch by 1 inch glass slide mounted on the sample holder. (b) Three glass slides coated with Ag clusters with deposition time of 30mins, 1 hour and 4 hours respectively. The color of the glass slides changed after being coated with the clusters and the longer the deposition glass, the more intense the darker color. The thickness of the coated clusters on the glass slides have been measured under the Surface Profile equipment (bench-top AFM) based in the clean room in NPRL, University of Birmingham. The measured thickness of these samples is 10±2nm, 22±3nm and 55±5nm respectively. Related parameters, matrix condensation support, 1000 mesh copper grid; matrix temperature, 9K; metal concentration, 1.2%; Ar gas dosing pressure, 6E-8mbar; matrix thickness, ~128nm; incident ion beam current on matrix, 50μA; beam energy, 1keV; matrix condensation time, 300s and deposition time, 300s for each cycle.

Since it has been demonstrated that clusters can be produced at high flux, equivalent to nearly 100nA, covering area of 30mm by 30mm, we attempted coating large area glass slides (1 inch by 1 inch, as shown in Figure 6.9a) with clusters produced in the MACS 1 in transmission mode. This would demonstrate large area coating and stable cluster production over a long deposition time, which that is essential for applications e.g. biochips. The coating process,

including matrix condensation and cluster deposition, was non-continuous. In order to avoid contaminating the samples with vaporized materials, the glass slide was covered by a shutter during the matrix condensation. During the deposition the shutter on the evaporator was fully closed. Each cycle was 5mins. The glass slides have been coated with Ag clusters with deposition time of 30mins, 1 hour and 4 hours respectively as shown in Figure 6.9b. The color of the glass slides changed after being coated with the clusters and the longer the deposition glass, the more intense the darker color. The thickness of the coated clusters on the glass slides have been measured under the Surface Profile equipment (bench-top AFM) based in the clean room in NPRL, University of Birmingham. The measured thickness of these samples is 10±2nm, 22±3nm and 55±5nm respectively.

6.2.3 Size distribution

The clusters produced in the high flux samples have an average size of 3.1±1nm, which is not as narrow as expected when compared to samples produced by the MACS demonstration system 1.6±0.4nm. The explanation for the "narrow" size distribution not being maintained in high flux sample is probably due to the high energy (5keV) of the incident Ar ion beam used to sputter the matrix to achieve high flux. With such a high energy incident ion beam, significantly more momentum and energy is delivered to the matrix leading to massive aggregation of metal atoms inside the matrix which causes the non-uniform distribution of the metal atoms across the matrix during the sputtering and this non-uniform matrix eventually leads to broad size of produced clusters [5-10]. However,

when lowering incident beam energy for example 1keV instead of 5keV, the clusters exhibit "narrow" size distribution again as shown in Figure 6.10(a). The size distribution measured from the integrated HAADF intensity of shown in Figure 6.10(b).

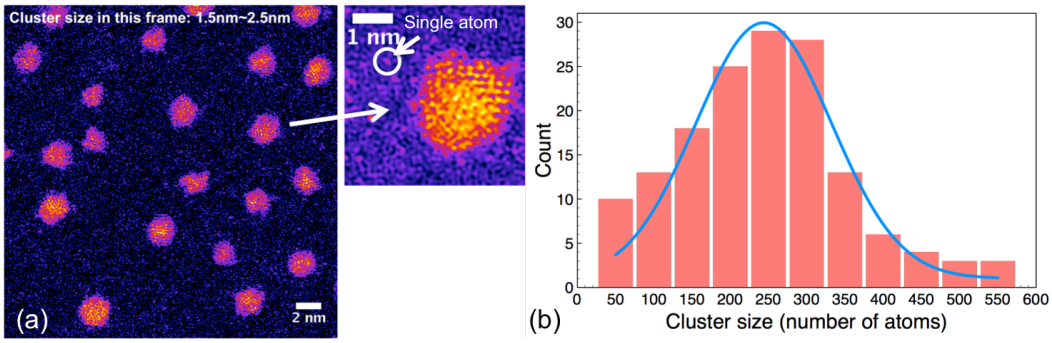

Figure 6.10(a) HAADF STEM image and atomic resolution image of Ag clusters prepared in MACS 1 using 1keV incident beam energy. All clusters in this image have diameter of 2±0.5nm. (b) Histogram of size distribution of the Ag clusters. The number of atoms is measured from the integrated HAADF intensity comparing to the HAADF intensity of single atoms. The histogram shows the clusters contain a average size of 250 atoms and half width of the distribution is from about 150 to 350, which gives a mass resolution around M/ΔM=1.25. Related parameters, matrix condensation support, 1000 mesh copper grid; matrix temperature, 9K; condensation time, 200s; metal concentration, 1.2%; Ar gas dosing pressure, 6E-8mbar; matrix thickness, ~85nm; incident ion beam current on matrix, 50μA; beam energy, 1keV; deposition time, 120s.

As shown in the STEM image, all clusters in this image have a diameter of 2±0.5nm. The histogram of size distribution shows the clusters contain a average size of 250 atoms and half width of the distribution is from about 150 to 350,

which gives a mass resolution around M/ΔM=1.25. More details of effects of incident beam energy on cluster size will be discussed later in the effect of incident beam energy part.

6.2.4 Size control

As preliminary demonstrated using the MACS demonstration apparatus, the size of clusters can be controlled during the formation stage without any additional mass selection. Results show cluster size is sensitive to several parameters, especially the metal concentration in the matrix. This work was repeated in the MACS 1 system but more systematically and with much better control of all the parameters. HAADF STEM images (2Mx) and atomic resolution images (12Mx) of Ag clusters prepared with different metal concentration (from 0.6% to 4.8%) are shown in Figure 6.11(a). The corresponding histograms of cluster size distribution measured from the integrated HAADF intensity are shown in Figure 6.11(b). The Gaussian function was used to fit the histograms of size distribution in order to obtain the average sizes and size spreads. The cluster size and flux as a function of metal concentration in the metal are plotted in Figure 6.11(c) and (d) respectively.

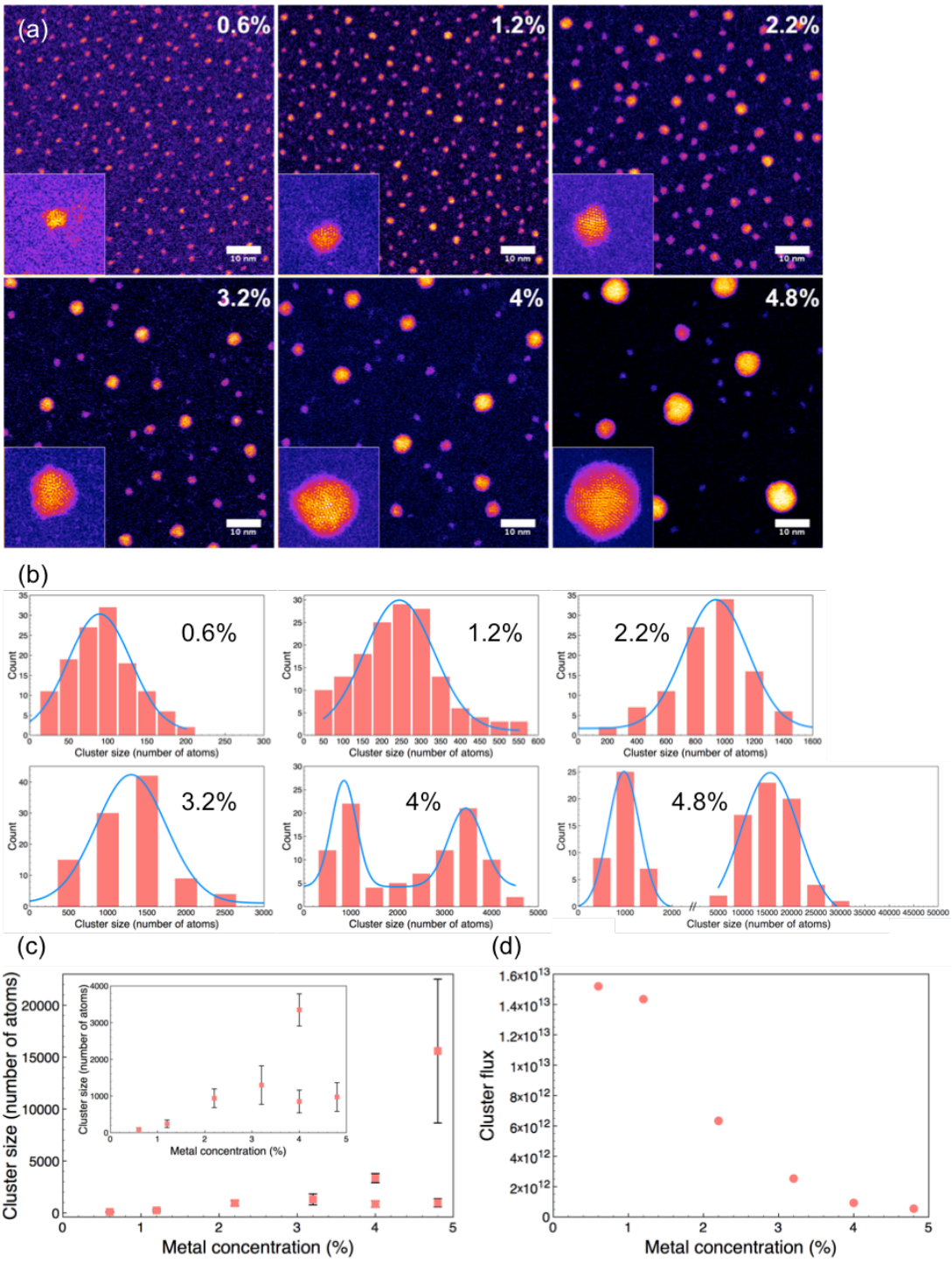

Figure 6.11 (a) HAADF STEM images (2Mx) and atomic resolution images of Ag clusters prepared with different metal concentration in the matrix from 0.6% to 4.8%. (b) Histograms of size distributions of the Ag cluster with different metal concentration in the matrix. The size of clusters is measured from the integrated HAADF intensity compared with HAADF intensity of single atoms. (c) The plot of

size of clusters as a function of metal concentration. (d) The plot of cluster flux as a function of metal concentration. The cluster flux is measured from the cluster density on HAADF STEM images. Related parameters, matrix condensation support, 1000 mesh copper grid; matrix temperature, 9K; condensation time, 200s; Ar gas dosing pressure, 6E-8mbar; matrix thickness, ~85nm; incident ion beam current on matrix, 50μA; beam energy, 1keV; deposition time, 120s.

As mentioned before, the cluster formation in the MACS is possibly through two mechanisms: clusters preformed due to the potential force [11-14] and aggregated because of the ion impacts [15-23]. With higher metal concentration in the matrix, clusters formed in both mechanisms are grown larger by capturing more atoms, as there is a higher density of cluster material atoms when metal concentration is high. However, the effects of the metal concentration on each formation mechanism have different levels. The clusters formed driven by potential force have limited mean free path that they are only able to capture atoms within few angstroms (as simulated by Dr. Lanqing Xu). While the clusters formed due to the aggregation under ion impacts are more energetic that larger clusters are more likely to be formed with the help of ion-induced diffusion. This difference leads to the spread size distribution of clusters prepared at higher metal concentration matrix (4% and 4.8%). The trend of total cluster flux decreases as a function of metal loading percentage in the matrix is probably due to the fact that heavier metal loaded matrix is hard to sputter and has a lower sputtering yield [5-10].

6.2.5 Different deposition time

To verify that clusters are produced from the matrix rather than through aggregation at the substrate [24], we deposited with different deposition times. If clusters are produced and directly deposited, the size distribution should remain constant. On the other hand, if single atoms are aggregating into clusters on the substrate, the size of clusters will be increased significantly with deposition time, as clusters will be able to grow larger with more atoms on the surface. HAADF STEM images of Ag clusters prepared at two different matrix metal concentrations (1.2% and 3.2%) and different deposition times are shown in Figure 6.12 (a) and (c). The histograms of size distributions of these two sets of samples are shown in Figure 6.12 (b) and (d).

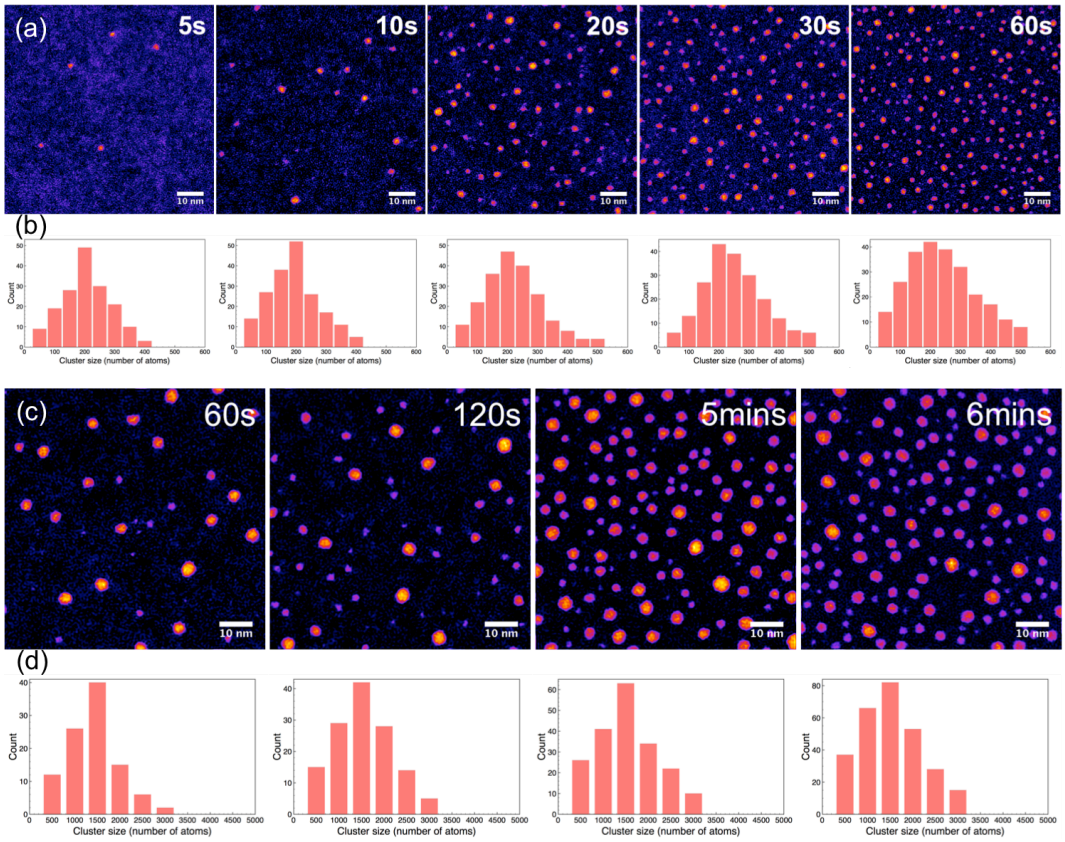

Figure 6.12(a) HAADF STEM images of Ag clusters prepared at matrix metal concentration of 1.2% with different deposition times from 5s to 60s. (b)

Histograms of size distribution of the produced Ag clusters. (c) HAADF STEM images of Ag clusters prepared at matrix metal concentration of 3.2% with different deposition times from 60s to 6mins. (d) Histograms of size distribution of the produced Ag clusters. The size of clusters is measured from the integrated HAADF intensity compared to the HAADF intensity of single atoms. Related parameters, matrix condensation support, 1000 mesh copper grid; matrix temperature, 9K; condensation time, 300s; Ar gas dosing pressure, 6E-8mbar; matrix thickness, ~128nm; incident ion beam current on matrix, 50μA; beam energy, 1keV.

As shown in the HAADF STEM images and histograms of size distributions, the size of clusters prepared at both matrix metal concentration remains the same with different deposition time and the size distributions are quite similar. However, the distribution does shift slightly towards larger size as the deposition time increases due to clusters landing on top of each other with such high density. The results provide indirect evidence that the clusters are produced from the matrix rather than from single atoms aggregation. The direct proof is taking mass spectra of the clusters that will be discussed in mass spectra part.

6.3 Au clusters produced in MACS 1

Similar to the work done on Ag clusters, effects of different parameters (metal concentration, incident beam energy, matrix temperature etc.) on size and flux of

Au clusters produced in MACS 1 using transmission mode have also been investigated.

6.3.1 Metal concentration

HAADF STEM images of Au clusters prepared with different metal concentrations are shown in Figure 6.13(a). The histograms of size distribution measured from the integrated HAADF intensity compared from the HAADF intensity of size-selected Au_{923} clusters prepared using the magnetron sputtering cluster source (with a mass resolution of ±5%) are shown in Figure 6.13(b). The size and flux of clusters as a function of metal concentration in the matrix are plotted in Figure 6.13(c-d).

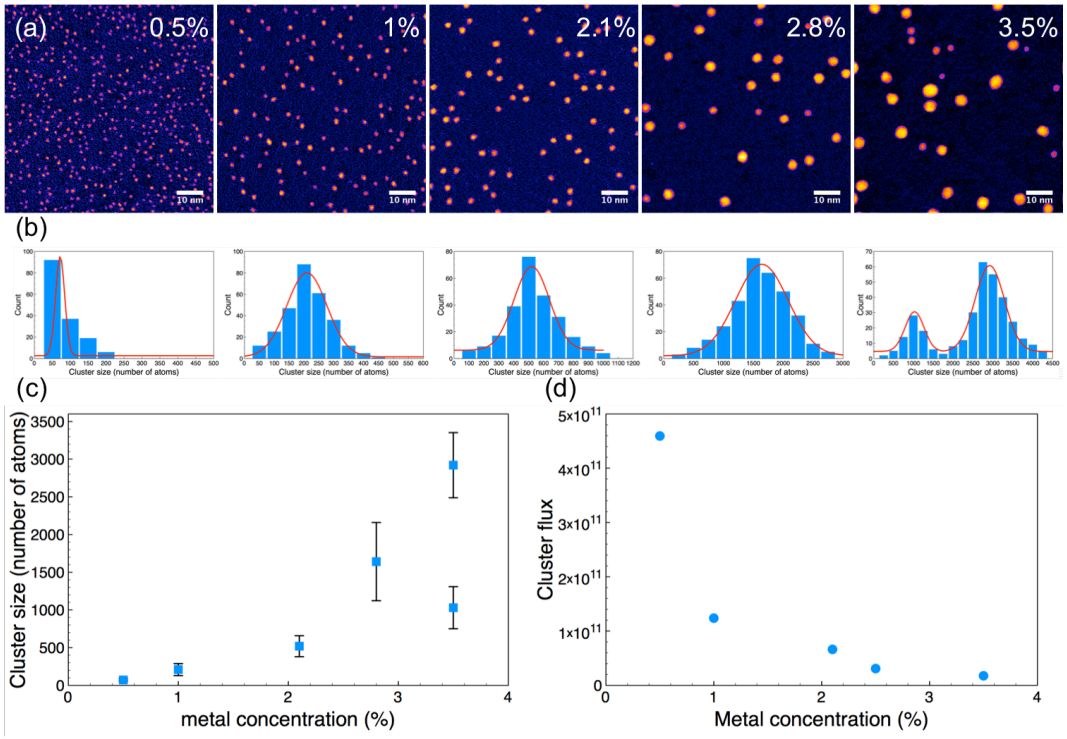

Figure 6.13 (a) HAADF STEM images of Au clusters prepared with different metal concentration in the matrix from 0.5% to 3.5%. (b) Histograms of size

distribution of the prepared Au clusters. The size of clusters is measured from the integrated HAADF intensity compared with HAADF intensity of size-selected Au_{923} clusters prepared using the magnetron sputtering cluster source (with a mass resolution of ±5%). (c) The plot of cluster size as a function of metal concentration in the matrix. (d) The plot of cluster flux as a function of metal concentration in the matrix. Related parameters, matrix condensation support, 1000 mesh copper grid; matrix temperature, 9K; condensation time, 200s; Ar gas dosing pressure, 6E-8mbar; matrix thickness, ~85nm; incident ion beam current on matrix, 50μA; beam energy, 1keV; deposition time, 120s.

As shown in Figure 6.13, cluster size increases as a function of the metal concentration in the matrix, while the flux of clusters decreases with the metal loading percentage in the matrix. The explanations are exactly same as that of Ag clusters based on the speculated the cluster formation mechanisms in the MACS. Another fact also consistent with the Ag cluster results is the size distribution of clusters starts to bifurcate into two peaks when the metal concentration is sufficiently high, as shown clearly in the STEM image and histogram of size distribution of 3.5% metal concentration sample. This behavior indicates the bimodal clusters formation mechanisms in the MACS.

6.3.2 Matrix temperature

The effect of matrix temperature on cluster size has also been investigated in the MACS 1 with the Au clusters produced in transmission mode. The temperature of the matrix is controlled through the flow of helium gas, the higher flow the

higher cooling power and therefore lower temperature. The temperature of the matrix fluctuates less than 1K during experiments. HAADF STEM images of Au clusters prepared with four different matrix temperatures from 9K to 22K are shown in Figure 6.14(a). The histograms of size distribution are shown in Figure 6.14(b).

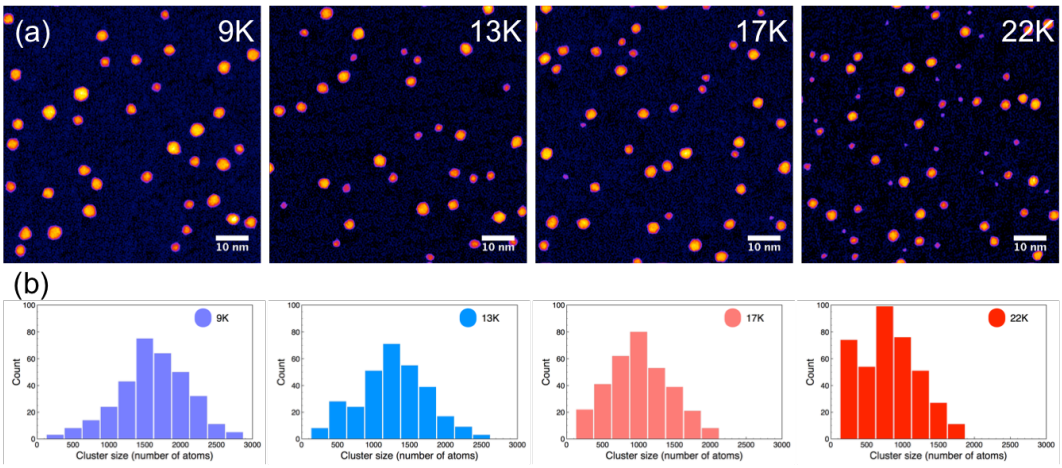

Figure 6.14 (a) HAADF STEM images of Au clusters prepared with different matrix temperature from 9K to 22K. The temperature of the matrix fluctuates less than 1K during experiments. (b) The histograms of size distribution of the Au clusters. The number of atoms in cluster is measured from the integrated HAADF intensity compared with the HAADF intensity of mass balance, the size-selected Au_{923} prepared in the magnetron sputtering source. Related parameters, matrix condensation support, 1000 mesh copper grid; condensation time, 200s; metal concentration, 2.8%; Ar gas dosing pressure, 6E-8mbar; matrix thickness, ~85nm; incident ion beam current on matrix, 50μA; beam energy, 1keV; deposition time, 120s.

As shown in the STEM images and the histograms of the size distributions, the distribution shifts to smaller sizes with the increased matrix temperature. The explanation to this phenomenon is not quite clear yet. We propose that the matrix temperature affects the following conditions: sputtering yield of the matrix, mobility of atoms in the matrix and the sticking co-efficient of the condensed atoms. The effect on the sputtering yield is mainly attributed to the thermal spike that atoms in a warmer matrix require less energy to eject [25-26]. The mobility of atoms affected by matrix temperature can be described by kinetic energy and Brownian motion [27]. For simplicity, the sticking co-efficient is treated as 1. Although metal atoms are more mobile in a warmer matrix intended to form larger clusters, they are more easily ejected from the matrix during ion bombardment as requiring less energy, meaning the clusters have less "germination time" (the time allowing cluster growth before leaving the matrix).

6.3.3 Effect of incident beam energy

Here, we varied the incident beam energy from 1keV to 4keV to study the effect of beam energy on Au cluster size and flux in transmission mode. HAADF STEM images of Au clusters prepared with different incident beam energy are shown in Figure 6.15(a) and the histograms of size distribution are shown in Figure 6.15(b).

As shown in the both STEM images and the histogram of size distributions, the size of clusters, both average and maximum size, is increased with the incident beam energy. However on the other hand, the size distribution becomes broader

when using high energy incident ion beam. For example, the mass resolution of the 1keV sample is about m/Δm=1, while it is about m/Δm~0.6 of the 4keV sample. The total cluster flux is also increased with incident ion beam energy as seen from the cluster density on the images. The changes in cluster size and flux can be explained based on the sputtering yeild, ion induced diffusion and energy transfer. The sputtering yield is increased with the beam energy, which results in the higher cluster flux [9]. Also high energy incident ions deliver more momentum to the matrix promoting the diffusion of metal atoms inside the matrix to aggregate into large clusters [6-10]. On the other hand, competing with the metal atoms aggregation in the matrix is the "germination time" decreases with the increased incident beam energy [25-26]. The ion-induced diffusion and vast aggragation lead to a non-uniform distribution of metal atoms inside the matrix, which contributes to the broader size distribution. All of these have effects on the clusters size.

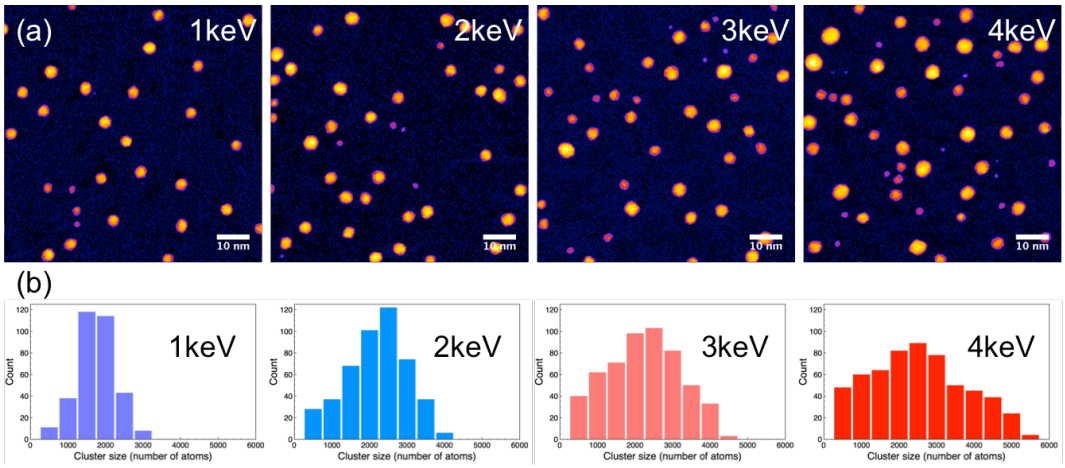

Figure 6.15 (a) HAADF STEM images of Au clusters prepared with different incident beam energy from 1keV to 4keV. (b) Histograms of size distribution of the produced Au clusters. The number of atoms in cluster is measured from the

integrated HAADF intensity compared with the HAADF intensity of mass balance, the size-selected Au_{923} prepared in the magnetron sputtering source. Related parameters, matrix condensation support, 1000 mesh copper grid; matrix temperature, 9K; condensation time, 200s; metal concentration, 2.8%; Ar gas dosing pressure, 6E-8mbar; matrix thickness, ~85nm; incident ion beam current on matrix, 50μA; deposition time, 120s.

6.4 Measurement of charge fractions

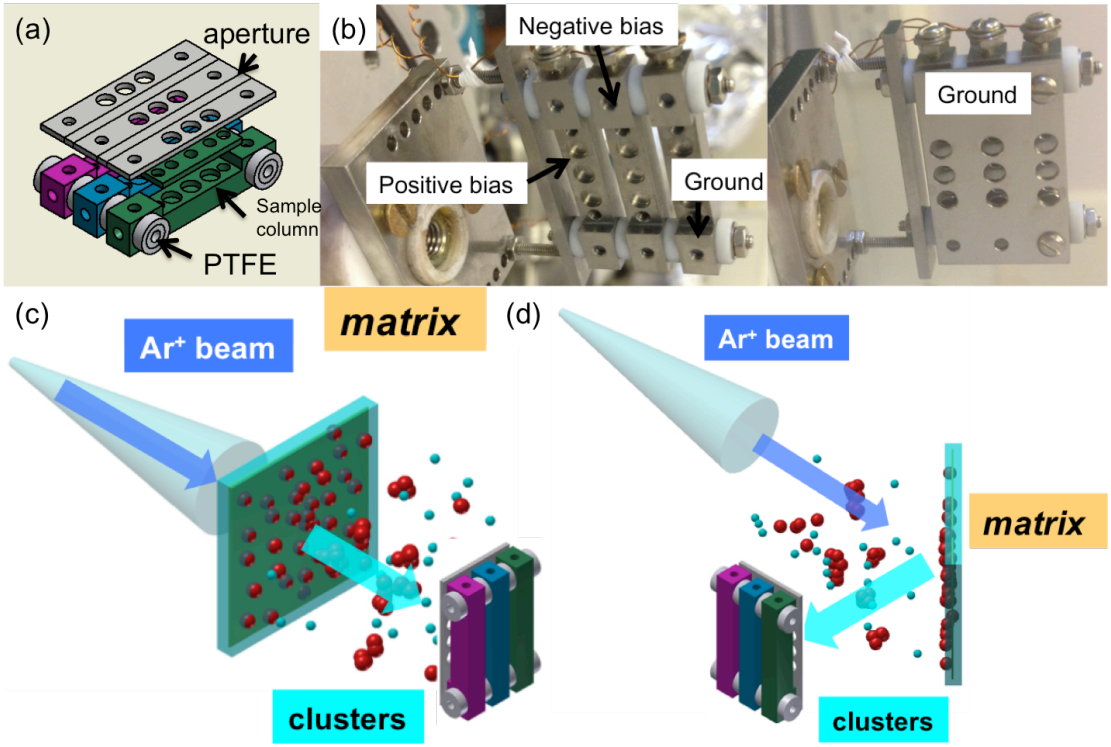

Figure 6.16 (a) Schematic diagram of the dedicated sample holder for charge fraction measurement. It consists of three columns which are electrical isolated from each other by PTFE rings enabling the application of different bias voltages: positive, negative and ground. An aperture is mounted in front of these three columns and the aperture is grounded to screen the electrical field generated on

the column. (b) Photograph of the sample holder installed in the MACS 1 apparatus. (c-d) Schematic diagram showing the charge fraction measurement in both transmission and reflection mode.

The charge fraction of clusters is measured with the help of a dedicated sample holder. As shown in Figure 6.16(a-d), the sample holder consists of three columns which are electrical isolated from each other by PTFE rings enabling the application of different bias voltages: positive, negative and ground. An aperture is mounted in front of these three columns and the aperture is grounded to screen the electrical field generated on the column. Therefore, it is electrical field free between the aperture and the matrix, while there is retarding field between the columns and the aperture. TEM grids are mounted on every column to collect clusters produced from the matrix. The charge fraction of clusters is determined by measuring the difference on cluster densities on each biased column, grounded, positive and negative. To verify the retarding field between the aperture and columns, the sample holder is placed in front of the Ar ion gun and Ar beam current using the same beam energy (1keV) measured on the column is plotted as a function of retarding voltages in Figure 6.17. The Ar beam current was measured at three different conditions: first with aperture and a copper mesh over the aperture (blue), then with aperture but no mesh (green) and finally without an aperture (red). As shown in the plot, the electrical field is well screened when the aperture is on as the current remains relatively stable when the column is negatively biased, such that it does not attract more Ar ions. There is very slight difference with or without the mesh. The retarding field between the column and aperture also works well, as the high energy Ar ion beam can be

stopped at some point around 400V. The voltage to stop Ar ion beam is actually much less than 1000V because the column starts attracting secondary electrons when it is positive biased.

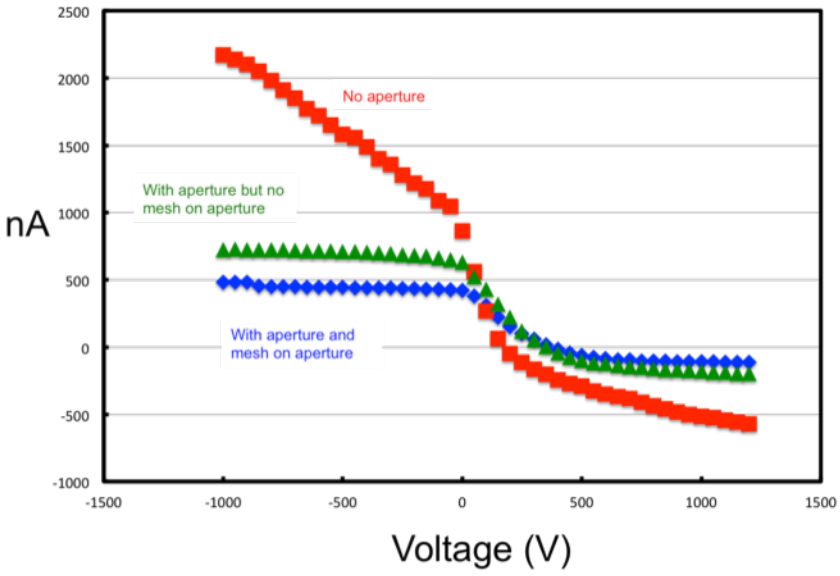

Figure 6.17 Current detected on the dedicated sample holder as a function of retarding voltage for the following configurations: with aperture and mesh over aperture (blue), with aperture only (green) and without aperture (red). The incident ion beam is Ar ions with energy of 1keV.

The charge fraction measurement obtained from both transmission and reflection modes using different experimental parameters are summarized in the Table 6.1, 6.2 and 6.3. Table 6.1 shows the charge fractions of clusters produced in transmission mode as a function of matrix thickness. Table 6.2 is the charge fraction results of clusters produced in reflection mode as a function of matrix thickness. Table 6.3 is the charge fraction of clusters production in reflection mode as a function of incident beam angle. The average cluster density on each sample was obtained by measuring over 25 images to reduce the statistical error.

The charge fraction (R_{pos} and R_{neg}) of clusters is determined by comparing the average number of clusters on the grounded column and biased columns using the equations:

$$R_{pos} = \frac{N_0 - N_{neg}}{N_0}$$

$$R_{neg} = \frac{N_0 - N_{pos}}{N_0}$$

where the N_0, N_{pos} and N_{neg} are the average numbers of clusters on grounded, positive biased and negative biased columns.

Matrix thickness (nm)	Cluster density (x10⁴/μm²)			Charge fractions (%)	
	0 bias	+50V bias	-50V bias	Positive	Negative
85	1.5±0.3	1.6±0.32	1.6±0.31	n/a	n/a
170	1.4±0.3	1.4±0.3	1.4±0.3	n/a	n/a
255	0.86±0.2	0.78±0.15	0.8±0.16	9.3	6.9
425	0.62±0.1	0.56±0.1	0.58±0.11	9.6	6.4

Table 6.1 The charge fractions of clusters produced in transmission mode as a function of matrix thickness. Related parameters, matrix condensation support, 1000 mesh copper grid; matrix temperature, 9K; metal concentration 1.1%; Ar gas dosing pressure, 6E-8mbar; incident ion beam current on matrix, 50μA; beam energy, 1keV; deposition time, 120s.

Matrix thickness (nm)	Cluster density (x10⁴/μm²)			Charge fractions (%)	
	0 bias	+50V bias	-50V bias	Positive	Negative
85	2.1±0.4	1.9±0.4	1.8±0.4	12	15
128	2±0.4	1.7±0.3	1.7±0.3	13	15
170	2±0.4	1.8±0.4	1.8±0.4	14	11
255	1.5±0.3	1.3±0.3	1.3±0.3	13	11
425	1.2±0.2	1±0.2	1±0.2	15	13

Table 6.2 The charge fraction results of clusters produced in reflection mode as a function of matrix thickness. elated parameters, matrix condensation support,

copper plate; matrix temperature, 9K; metal concentration 1.1%; Ar gas dosing pressure, 6E-8mbar; incident ion beam current on matrix, 50μA; beam energy, 1keV; deposition time, 120s; sputtering angle 40°.

Sputtering angle (°)	Cluster density (x10^4/μm^2)			Charge fractions (%)	
	0 bias	+50V bias	-50V bias	Positive	Negative
10	1.3±0.3	1.2±0.2	1.2±0.2	14	12
20	1.8±0.4	1.5±0.3	1.6±0.3	14	11
30	1.9±0.4	1.7±0.3	1.7±0.3	12	14
40	2.7±0.5	12.3±0.4	2.4±0.5	16	13

Table 6.3 The charge fraction of clusters production in reflection mode as a function of incident beam angle. Related parameters, matrix condensation support, copper plate; matrix temperature, 9K; metal concentration 1.1%; Ar gas dosing pressure, 6E-8mbar; matrix condensation time, 200s; matrix thickness, 85nm; incident ion beam current on matrix, 50μA; beam energy, 1keV; deposition time, 120.

As shown in the tables, the charge fractions of both positive and negative clusters produced in transmission mode is limited to less than 10% across the parameter space. However, in the reflection mode, charge fraction is sustained to around 15% for both positive and negative across all different thickness and incident angles. There are possibly two explanations. Firstly the transmission mode here is actually reflection involves at the micrometer scale, that the windows of the holey membrane are not closed and clusters are produced by Ar ions grazing the matrix or sputtering at very low angle. Therefore the energy transfer from incident ions to the clusters in transmission mode is much less than that in the reflection mode where ions are actually hitting the matrix at relatively large

angle [28-30], resulting in less ionization. Another possibility is the Ar matrix is not a good electrical conductor and it might be charged during the Ar ion beam sputtering. Clusters produced in the transmission mode are formed inside the micro-channels and are travelling through the channel before landing onto the substrate. If the matrix is charged but not uniformly charged, an electrical field will be created inside those channels which may deflect and stop the charged clusters flying out. While in the reflection mode there is no such obstruction after clusters are released out of the matrix [31-32].

6.5 Mass spectroscopy of clusters produced in the MACS

6.5.1 Experiment setup

The lateral time-of-flight mass filter is attached to the MACS 1 in order to acquire mass spectra as shown in Figure 6.18. The clusters are produced in the reflection mode as the charge fraction is higher than that of the transmission mode. A set of ion optic lenses with an XY deflector are built in between the cluster generation chamber and the mass filter to extract and focus clusters through. The orientation of the matrix is 45 degree from the incident beam direction. In order to prevent the ion optic lenses shorting from the vaporized metal, a metal case has been designed to protect the lenses as well as screen the electrical field around the outside of the ion optic lenses.

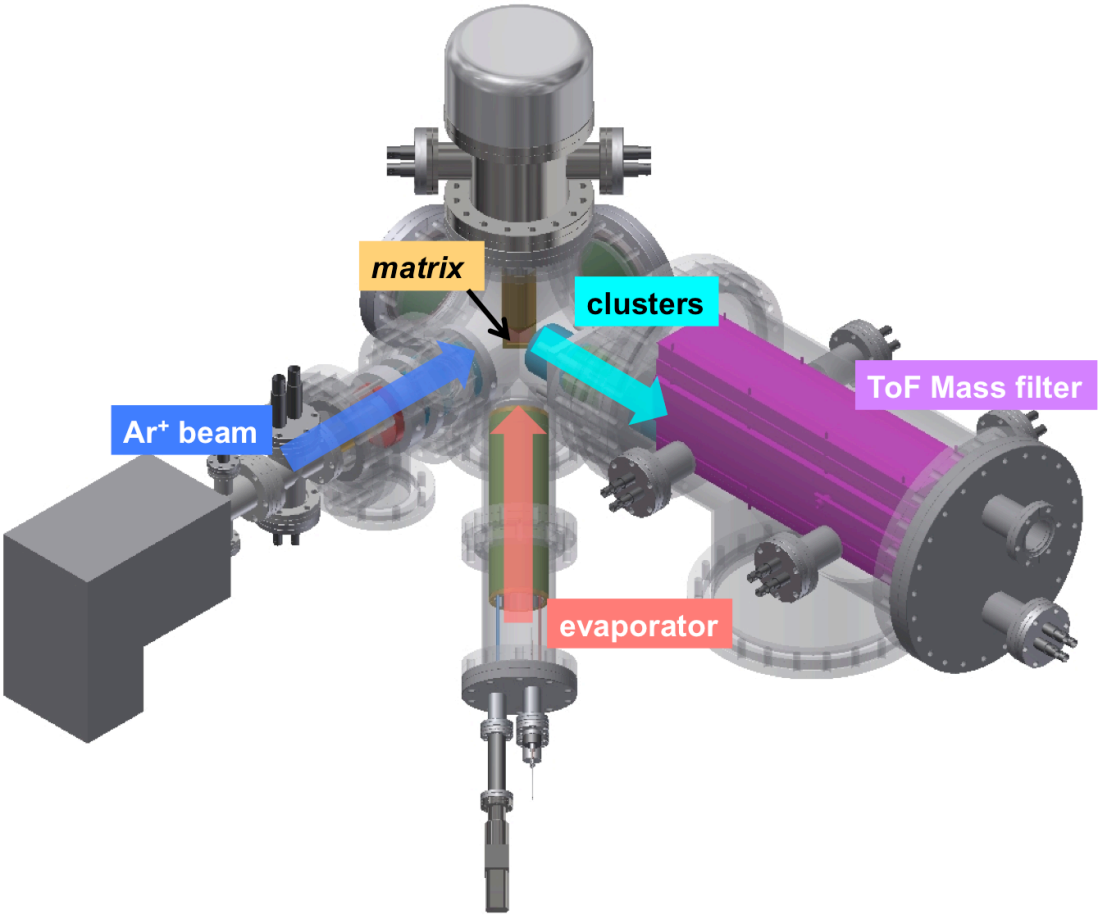

Figure 6.18 Schematic diagram of MACS 1 experimental apparatus equipped with lateral time-of-flight mass filter for mass spectra measurement. Ion optic lenses are built in between to extract and focus cluster ions into mass filter.

6.5.2 SIMION simulation

As the matrix facing an angle to the axis of the ion optic lenses, the trajectory of cluster beam is simulated in the SIMION 8.1 to make sure it can be focused into mass filter through the ion optics, as well as to obtain the optimal voltage settings on each lens element for different cluster sizes. In the simulations, clusters produced out of the matrix are given random directions with initial energy spread between 1-50eV and the cluster size distributions between 1-100,

500-1500 and 3000-5000 Ag atoms are tested. The simulated trajectories of clusters with different size distributions are shown in Figure 6.19. The optimal voltage settings for each lens element with different cluster sizes are listed in Table 6.4.

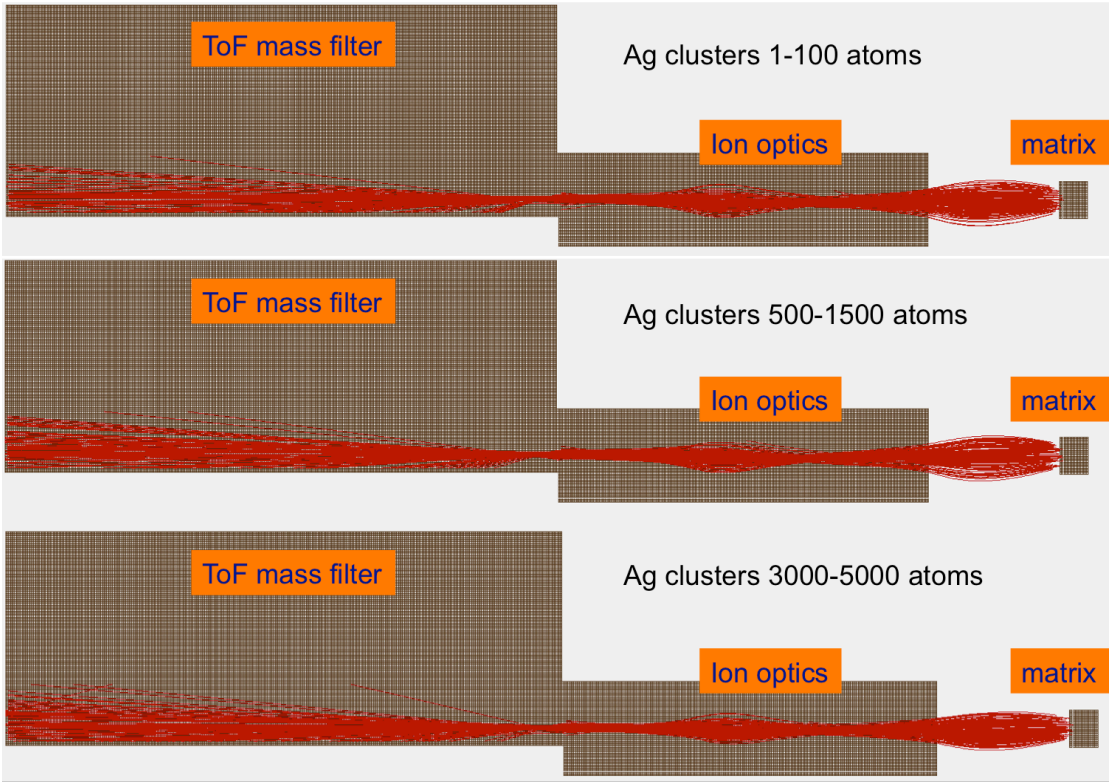

Figure 6.19 Simulated trajectories of the cluster ion beam for clusters with different size distributions.

Cluster size	Lens1	Lens2	Lens3 (XY lens)	Lens4
1-100 atoms	800V	600V	200V	800V
500-1500 atoms	1500V	850V	440V	800V
3000-5000 atoms	2200V	1500V	500V	800V

Table 6.4 The optimal voltage settings for each lens at different cluster size distributions obtained from simulations.

6.5.3 Mass spectra

Figure 6.20 shows the mass spectra when sputtering the bare matrix condensation support at room temperature. Two peaks are detected at 65amu and 108amu respectively, which belongs to residual Cu and Ag atoms as the matrix condensation grid is made of copper and some silver is left on the surface from the evaporation. The copper and silver ions are generated by the high energy ion beam bombardment. No peaks of clusters are detected as there is no matrix formed on the grid.

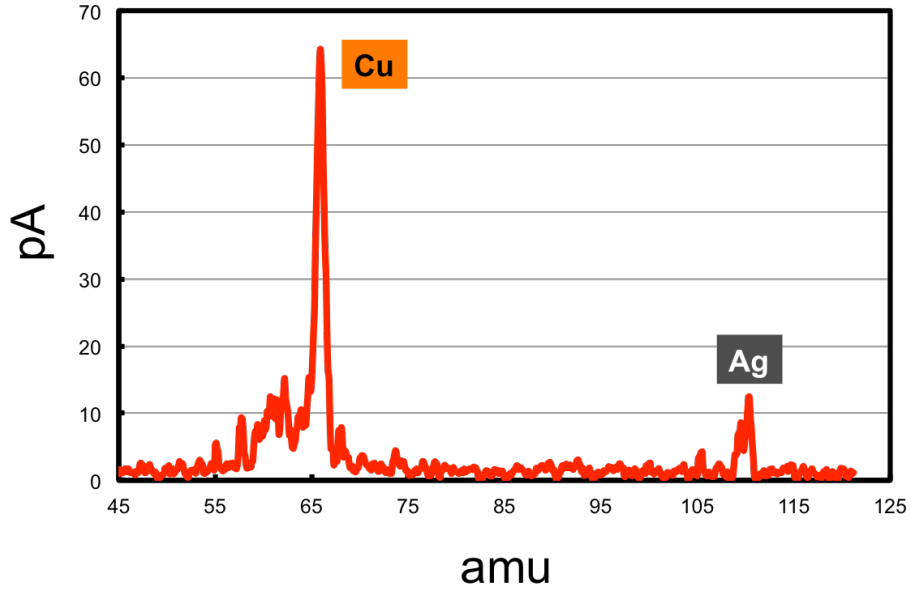

Figure 6.20 Mass spectra of sputtering the matrix condensation grid at room temperature. Two peaks detected at 65 amu and 108 amu respectively belong to copper and silver atoms as the matrix condensation grid is made of copper and some silver is left on the surface from the evaporation. The incident Ar ion beam current on the matrix support is about 30μA with beam energy of 1keV. The matrix support is grounded.

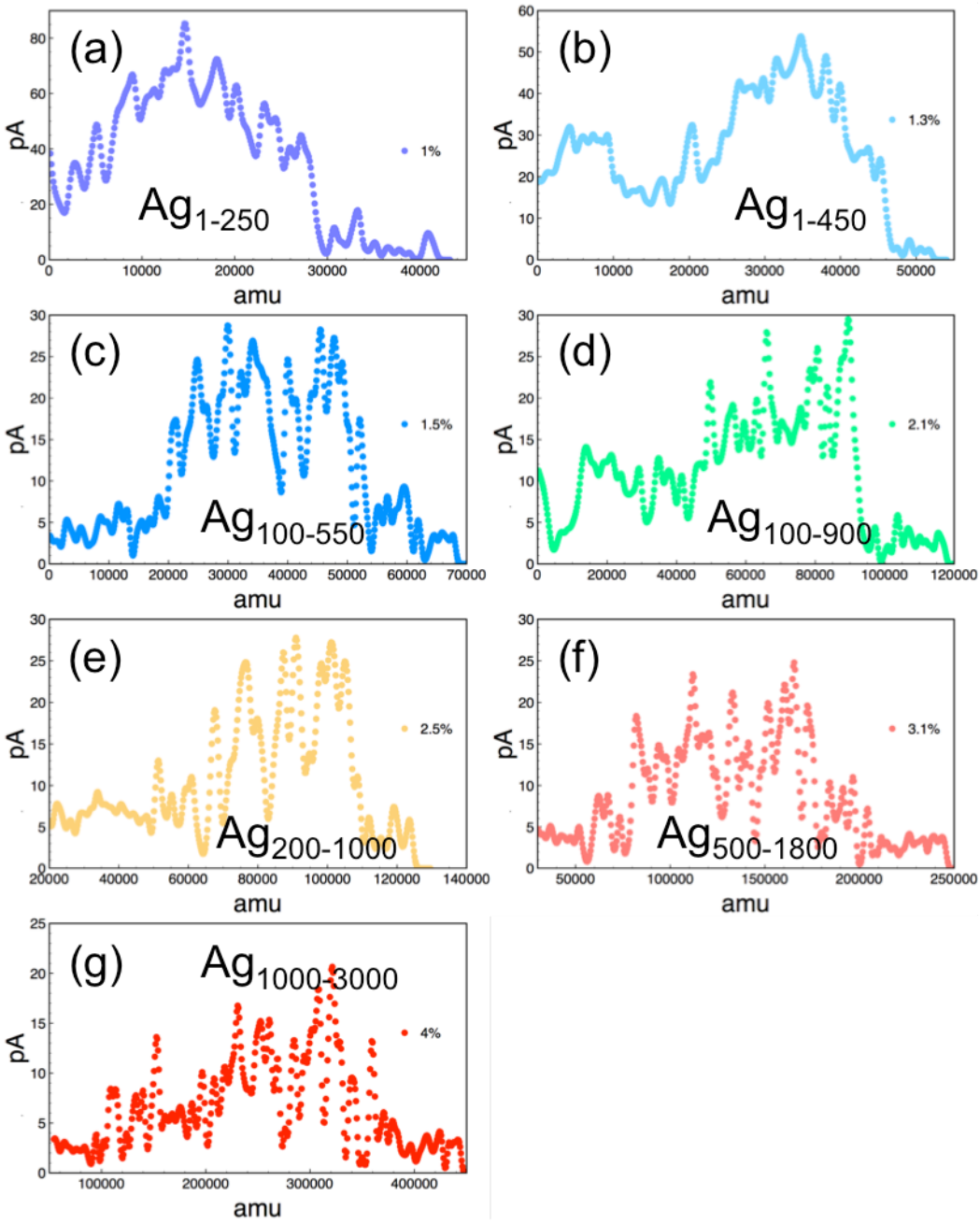

Figure 6.21 The mass spectra of Ag clusters produced with different metal concentration (from 1% to 4%) in the matrix. Clusters are produced in reflection mode. The matrix is pre-condensed for 5mins at Ar gas dosing pressure of 8E-6mbar before ion beam sputtering. The incident Ar ion beam current on the matrix is kept at 30μA for metal concentration between 1% and 1.5% (a-c) then is switched to a higher current 50~60μA for the heavier metal loadings from

2.1% to 4% (d-g) to get a better signal. The beam energy is kept at 1keV and matrix support is grounded.

The mass spectra of Ag clusters produced with different metal concentration (from 1% to 4%) in the matrix are shown in Figure 6.21. The size ranges of clusters detected at different metal concentrations are also marked in the mass spectra. The mass spectra measurement of the clusters directly demonstrates the proof-of-principle of the MACS technology. The variations in the mass spectra such as cluster size, size distribution and flux at different metal concentration are also consistent with the STEM results discussed previously. Please be aware the peaks observed in all the mass spectra shown above are not referring to the magic numbers. Instead they are more likely the fluctuations due to the unstable incident ion beam current or charging and discharging of the matrix.

6.6 Summary

In this chapter, the design and operation of a new experimental setup of the MACS system, the MACS 1, to scale up the cluster production rate has been discussed. The MACS allows further exploration of the effects of different experimental parameters on cluster size and flux. The cluster flux we have achieved in the MACS 1 is equivalent to nearly 100nA of Ag clusters produced from the 1-inch by 1-inch matrix in transmission mode. The effects of metal concentration in the matrix, incident beam energy and deposition time on both Ag and Au cluster size and flux have been investigated. The charge fractions of the clusters are also studied, with charged fractions of <10% and <15% for

transmission and reflection mode, respectively. Mass spectra are obtained from the charged clusters using lateral time-of-flight mass selector, further confirming the cluster production and size control in the MACS.

List of references

[1] Anton, R., et al. "Design and performance of a versatile, cost-effective microwave electron cyclotron resonance plasma source for surface and thin film processing." *Review of Scientific Instruments* 71.2 (2000): 1177-1180.

[2] Baxter, William J., and Stanley R. Rouze. "A photoemission electron microscope using an electron multiplier array." *Review of Scientific Instruments*44.11 (1973): 1628-1629.

[3] Stefanaki, Eleni-Chrysanthi. "Electron Microscope: The Basics."

[4] Dahl, David A. "SIMION for the personal computer in reflection." *International Journal of Mass Spectrometry* 200.1 (2000): 3-25.

[5] Balaji, V., et al. "Sputtering yields of condensed rare gases." *Nuclear Instruments and Methods in Physics Research Section B: Beam Interactions with Materials and Atoms* 46.1 (1990): 435-440.

[6] Makeev, Maxim A., and Albert-László Barabási. "Ion-induced effective surface diffusion in ion sputtering." *Applied physics letters* 71.19 (1997): 2800-2802.

[7] Babaev, V. O., Ju V. Bykov, and M. B. Guseva. "Effect of ion irradiation on the formation, structure and properties of thin metal films." *Thin Solid Films* 38.1 (1976): 1-8.

[8] Marinov, Miko. "Effect of ion bombardment on the initial stages of thin film growth." *Thin Solid Films* 46.3 (1977): 267-274.

[9] MacLaren, S. W., et al. "Surface roughness development during sputtering of GaAs and InP: Evidence for the role of surface diffusion in ripple formation and sputter cone development." *Journal of Vacuum Science & Technology A* 10.3 (1992): 468-476.

[10] Cavaille, J. Y., and M. Drechsler. "Surface self-diffusion by ion impact." *Surface Science* 75.2 (1978): 342-354.

[11] Silvera, Isaac F., and Victor V. Goldman. "The isotropic intermolecular potential for H2 and D2 in the solid and gas phases." The Journal of Chemical Physics 69.9 (1978): 4209-4213.

[12] Mirsky, Kira. "Carbon monoxide molecules in an argon matrix: empirical evaluation of the Ar· Ar, C· Ar and O· Ar potential parameters." Chemical Physics 46.3 (1980): 445-455.

[13] Tang, K. T., and J. Peter Toennies. "New combining rules for well parameters and shapes of the van der Waals potential of mixed rare gas systems." Zeitschrift für Physik D Atoms, Molecules and Clusters 1.1 (1986): 91-101.

[14] Mann, D. E., N. Acquista, and David White. "Infrared Spectra of HCl, DCl, HBr, and DBr in Solid Rare‐Gas Matrices." The Journal of Chemical Physics 44.9 (1966): 3453-3467.

[15] Makeev, Maxim A., and Albert-László Barabási. "Ion-induced effective surface diffusion in ion sputtering." Applied physics letters 71.19 (1997): 2800-2802.

[16] Winters, Harold F., et al. "Energy transfer from rare gases to surfaces: Collisions with gold and platinum in the range 1–4000 eV." *Physical Review B*41.10 (1990): 6240.

[17] Coufal, H., et al. "Energy transfer from noble-gas ions to surfaces: Collisions with carbon, silicon, copper, silver, and gold in the range 100–4000 eV."*Physical Review B* 44.10 (1991): 4747.

[18] Averback, R. S., and T. Diaz de la Rubia. "Displacement damage in irradiated metals and semiconductors." Solid State Physics 51 (1997): 281-402.

[19] Smith, Roger. Atomic and ion collisions in solids and at surfaces: theory, simulation and applications. Cambridge University Press, 2005.

[20] De La Rubia, T. Diaz, et al. "Role of thermal spikes in energetic displacement cascades." Physical review letters 59.17 (1987): 1930.

[21] Aderjan, Ralf, and Herbert M. Urbassek. "Molecular-dynamics study of craters formed by energetic Cu cluster impact on Cu." Nuclear Instruments and Methods in Physics Research Section B: Beam Interactions with Materials and Atoms 164 (2000): 697-704.

[22] Nordlund, K., et al. "Defect production in collision cascades in elemental semiconductors and fcc metals." Physical Review B 57.13 (1998): 7556.

[23] https://en.wikipedia.org/wiki/Collision_cascade

[24] Daniel, Marie-Christine, and Didier Astruc. "Gold nanoparticles: assembly, supramolecular chemistry, quantum-size-related properties, and applications toward biology, catalysis, and nanotechnology." *Chemical reviews* 104.1 (2004): 293-346.

[25] Winters, Harold F., et al. "Energy transfer from rare gases to surfaces: Collisions with gold and platinum in the range 1–4000 eV." *Physical Review B*41.10 (1990): 6240.

[26] Coufal, H., et al. "Energy transfer from noble-gas ions to surfaces: Collisions with carbon, silicon, copper, silver, and gold in the range 100–4000 eV."*Physical Review B* 44.10 (1991): 4747.

[27] Mori, Hazime. "Transport, collective motion, and Brownian motion." *Progress of theoretical physics* 33.3 (1965): 423-455.

[28] Kaminsky, Manfred. *Sputtering of Metal Surfaces by Ion Bombardment*. Springer Berlin Heidelberg, 1965.

[29] Ullevig, Dale M., and John F. Evans. "Measurement of sputtering yields and ion beam damage to organic thin films with the quartz crystal microbalance."*Analytical Chemistry* 52.9 (1980): 1467-1473.

[30] Laegreid, Nils, and G. K. Wehner. "Sputtering yields of metals for Ar+ and Ne+ ions with energies from 50 to 600 eV." *Journal of Applied Physics* 32.3 (1961): 365-369.

[31] Baba, Y., et al. "Formation and dynamics of exciton pairs in solid argon probed by electron-stimulated ion desorption." *Physical review letters* 66.25 (1991): 3269.

[32] Merrison, J. P., et al. "Field assisted positron moderation by surface charging of rare gas solids." *Journal of Physics: Condensed Matter* 4.12 (1992): L207.

Chapter 7 Conclusions and Outlook

In this thesis, we have presented work exploring size dependent propagation of size selected Au nanoclusters through few layer graphene; atomic structure control of size selected Au nanoclusters during formation and the principle demonstration and development of the new technology, the matrix assemble cluster source (MACS). In this chapter, we summarize the conclusions from the work and raise revealed opportunities and challenges for the future.

Size dependent propagation

The work presented in Chapter 4.1 exploring the size dependent propagation of size selected Au nanoclusters through few layer graphene. Results show the Au_{55} nanoclusters penetrate through the FLG while the Au_{923} nanoclusters, with same deposition energy, remain on the surface. This work has demonstrated the utilization of nanoclusters to control the properties of grahene-based materials or novel membranes through mechanisms of defects generation or dopants of nanoclusters. It would be interesting to investigate the applications of the

nanostructured membrane decorated by clusters, for example as filters for selective permeations.

Atomic structure control

In this work, we have combined the HAADF STEM imaging technique with multi-slice simulation to determine the structures of size-selected Au_{923} clusters as a function of magnetron power and condensation length. Results have demonstrated that the structure of clusters is a function of the formation parameters. Significantly, one can eliminate icosahedral isomers in Au_{923} with a specific set of parameters. This approach offers opportunities to explore the properties of nanoclusters not only as a function of size but also atomic configurations. However, in order to produce ensembles of isomerically pure clusters, take Au_{923} as the example, the elimination of the decahedral or fcc isomers is a necessity. Possible routines are to investigate the formation parameters with broader range, or to add further process after the cluster formation, such as using laser to heat up clusters in flight.

The MACS

The MACS is designed aiming to scale up the cluster production rate by ~7 orders of magnitude. The concept of the MACS technology has been introduced in chapter 5 and the MACS demonstration system has been built to demonstrate the proof-of-principle. Preliminary studies of effects of metal concentration and incident beam energy on cluster production have been presented. We have also reported the progress on scaling-up the production rate by using powerful ion source and high-density matrix support.

The technical development and more systematical investigation of the MACS were presented in Chapter 6. The cluster flux with the upgraded MACS 1 has been improved to equivalent to nearly 100nA. Effects of different parameters such as metal concentration, incident beam energy, matrix temperature on cluster production were studied intensively. The charge fractions of the clusters were also studied and mass spectra measurement was achieved from the positively charged clusters using the lateral time-of-flight mass selector, further confirming the cluster production and size control in the MACS.

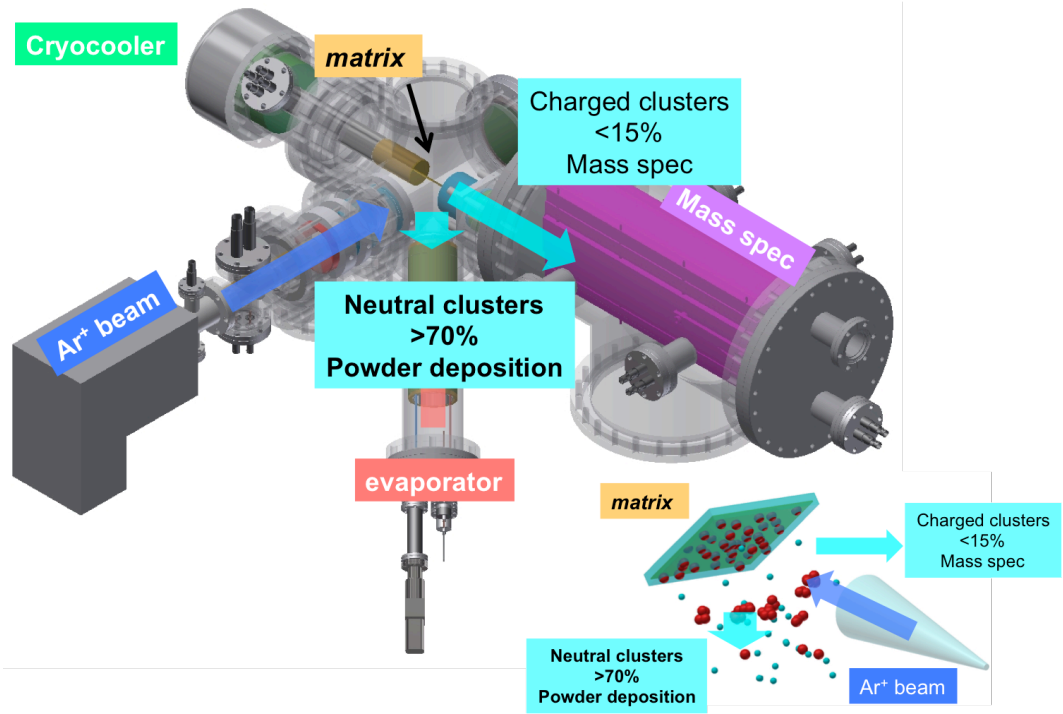

Figure 7.1 Schematic diagram of MACS 1.2. In MACS 1.2 clusters are produced in reflection mode. The neutral clusters are deposited onto powders for catalyst studies and the positively charged portion are used for mass spectra measurement to monitor the size.

One of the biggest future challenges for the MACS is to understand the cluster formation mechanism. Although we are able to produce clusters using the MACS method, the mechanisms behind their formation still incompletely understood. Simulation work is in progress (by Dr. L. Xu) to reveal what is happening in the matrix during the Ar ions sputtering. The simulation results show that clusters can be preformed in the matrix and the size of clusters remaining in the matrix increases with the number of ions, which have bombarded the matrix. Other challenges are technical issues in scaling up the production rate such as efficient cooling, pre-cooling of the matrix gas, matrix replenishment, high flux ion beam management and how to recycle metals which all require future investigations.

In short time, the next step of the MACS project is to upgrade the MACS 1 to MACS 1.2. The schematic diagram of the MACS 1.2 is shown in Figure 7.1. Clusters are produced in reflection mode in MACS 1.2. An ion source with 4mA output current will be adopted. Based on the efficiency of 1%, by efficiency we mean the number of clusters produced per argon ion incident on matrix from which a cluster beam can be formed, we are aiming for 40μA cluster production rate equivalent to ~10 milligram materials produced per hour. We have already achieved over 10μA cluster production rate over 1 hour in recent experiments, measured by QCM. According to the charge ratio results, the neutral clusters (more than 70%) will be used to deposit onto a powder deposition system for catalyst applications, where the positively charged clusters (less than 15%) will be used to monitor the size of produced clusters in real time using the lateral time-of-flight mass filter. The delivery time for MACS 1.2 will be this year. The plan to build super abundant cluster source, the MACS 3, is also around the

corner. In MACS 3, an ion source (from microsystem) with beam current of 800mA will be applied. In principle, we are able to produce at least 1mA cluster beam equivalent to grams of materials per hour using MACS 3, based on the obtained efficiency. Other plans on the MACS are testing another matrix gas e.g. using CO_2 to replace Ar to save the cooling power and using laser instead Ar ions to ablate the matrix.